Master Thesis

The Character of the Core-Mantle Boundary: A Systematic Study using PcP

Alexandra Carina Gassner

University of Potsdam

Institute of Earth and Environmental Science

Supervisors

Prof. Dr. Weber

GFZ German Research Centre for Geosciences Potsdam
Physics of the Earth
Geophysical Deep Sounding

apl. Prof. Dr. Krüger

University of Potsdam

Date of Submission
21-09-2012

Published online at the
Institutional Repository of the University of Potsdam:
URL http://opus.kobv.de/ubp/volltexte/2013/6359/
URN urn:nbn:de:kobv:517-opus-63590
http://nbn-resolving.de/urn:nbn:de:kobv:517-opus-63590

Contents

List of Figures

Erklärung

Hiermit erkläre ich, dass ich die vorliegende Arbeit selbständig und nur mit den angegebenen Hilfsmitteln erstellt habe.

Alexandra Carina Gassner

Assuming that liquid iron alloy from the outer core interacts with the solid silicate-rich lower mantle the influence on the core-mantle reflected phase PcP is studied. If the core-mantle-boundary is not a sharp discontinuity, this becomes apparent in the waveform and amplitude of PcP. Iron-silicate mixing would lead to regions of partial melting with higher density which in turn reduces the velocity of seismic waves.

On the basis of the calculation and interpretation of short-period synthetic seismograms, using the reflectivity and Gauss Beam method, a model space is evaluated for these ultra-low velocity zones (ULVZs). The aim of this thesis is to analyse the behaviour of PcP between 10° and 40° source distance for such models using different velocity and density configurations. Furthermore, the resolution limits of seismic data are discussed. The influence of the assumed layer thickness, dominant source frequency and ULVZ topography are analysed. The Gräfenberg and NORSAR arrays are then used to investigate PcP from deep earthquakes and nuclear explosions.

The seismic resolution of an ULVZ is limited both for velocity and density contrasts and layer thicknesses. Even a very thin global core-mantle transition zone (CMTZ), rather than a discrete boundary and also with strong impedance contrasts, seems possible: If no precursor is observable but the $\mathrm{PcP}^{model}/\mathrm{PcP}^{smooth}$ amplitude reduction amounts to more than 10%, a very thin ULVZ of 5 km with a first-order discontinuity may exist. Otherwise, if amplitude reductions of less than 10% are obtained, this could indicate either a moderate, thin ULVZ or a gradient mantle-side CMTZ.

Synthetic computations reveal notable amplitude variations as function of the distance and the impedance contrasts. Thereby a primary density effect in the very steep-angle range and a pronounced velocity dependency in the wide-angle region can be predicted. In view of the modelled findings, there is evidence for a 10 to 13.5 km thick ULVZ 600 km south-eastern of Moscow with a NW-SE extension of about 450 km. Here a single specific assumption about the velocity and density anomaly is not possible. This is in agreement with the synthetic results in which several models create similar amplitude-waveform characteristics. For example, a ULVZ model with contrasts of -5% V_P, -15% V_S and +5% density explain the measured PcP amplitudes. Moreover, below SW Finland and NNW of the Caspian Sea a CMB topography can be assumed. The amplitude measurements indicate a wavelength of 200 km and a height of 1 km topography, previously also shown in the study by Kampfmann and Müller (1989).

Better constraints might be provided by a joined analysis of seismological data, mineralogical experiments and geodynamic modelling.

Unter der Annahme, dass flüssiges Eisen aus dem äußeren Erdkern mit dem festen, silikat-reichen Unteren Mantel reagiert, wird eine Einflussnahme auf die Kern-Mantel Reflexionsphase PcP erwartet. Ist die Kern-Mantel Grenze aufgeweicht, und nicht wie bislang angenommen ein diskreter Übergang, so zeichnet sich dies in der Wellenform und Amplitude von PcP ab. Die Interaktion mit Eisen führt zu teilweise aufgeschmolzenen Bereichen höherer Dichte, welche die seismischen Wellengeschwindigkeiten herabsetzen.

Basierend auf den Berechnungen von kurzperiodischen synthetischen Seismogrammen, mittels der Reflektivitäts- und Gauss Beam Methode, soll ein möglicher Modellraum dieser Niedriggeschwindigkeitszonen ermittelt werden. Das Ziel dieser Arbeit ist es das Verhalten von PcP im Distanzbereich von 10° bis 40° unter dem Einfluss dieser Modelle mit diversen Geschwindigkeits- und Dichtekontrasten zu untersuchen. Ferner wird das Auflösungsvermögen hinsichtlich seismischer Daten diskutiert. Entscheidende Parameter wie Anomaliedicke, Quellfrequenz und Topographie werden hierbei analysiert. Tiefe Erdbeben und Kernexplosionen, die sich im entsprechenden Entfernungsbereich zum Gräfenberg und NORSAR Array befinden, werden anschließend im Hinblick auf PcP ausgewertet.

Das seismische Auflösungsvermögen von Niedriggeschwindigkeitszonen ist stark begrenzt sowohl in Bezug auf Geschwindigkeits- und Dichtekontraste als auch hinsichtlich der Mächtigkeit. Es besteht sogar die Möglichkeit einer dünnen, globalen Kern-Mantel Übergangszone, selbst mit großen Impedanzkontrasten, ohne dass dies mit seismologischen Methoden detektiert werden könnte: Wird kein precursor zu PcP beobachtet aber das $\mathrm{PcP}^{model}/\mathrm{PcP}^{smooth}$ Amplitudenverhältnis zeigt gleichzeitig eine Reduktion von mehr als 10%, dann könnte eine sehr dünne Niedriggeschwindigkeitszone von ca. 5 km Mächtigkeit und einer Diskontinuität erster Ordnung vorliegen. Andererseits, ist PcP um weniger als 10% reduziert, könnte dies entweder auf eine dünne, moderate Niedriggeschwindigkeitszone oder einen graduellen Kern-Mantel Übergang hindeuten.

Die synthetischen Berechnungen ergeben starke Amplitudenvariationen als Funktion der Distanz, welche auf den Impedanzkontrast zurückzuführen sind. Dabei ergibt sich ein primärer Dichteeffekt im extremen Steilwinkelbereich und ein maßgeblicher Geschwindigkeitseinfluss im Weitwinkelbereich. Im Hinblick auf die modellierten Resultate lässt sich eine 10 - 13.5 km mächtige Niedriggeschwindigkeitszone 600 km südöstlich von Moskau mit einer NW-SE Ausdehnung von mindestens 450 km folgern, wobei eine exakte Aussage über Geschwindigkeiten und Dichte nicht möglich ist. Dies ist im Konsens mit den synthetischen Berechnungen, wonach viele unterschiedliche Modelle ähnliche Amplituden- und Wellenformcharakteristiken erzeugen. Zum Beispiel erklärt ein Modell mit Kontrasten von -5% V_P, -15% V_S and +5% Dichte die gemessenen PcP Amplituden.

Darüber hinaus können unterhalb des südwestlichen Finnlands und nord-nordwestlich des Kaspischen Meeres Undulationen an der Kern-Mantel Grenze selbst vermutet werden. Unter Berücksichtigung früherer Studien, z. B. von Kampfmann and Müller (1989), deuten die Messergebnisse auf eine laterale Topographie von 200 km und eine Höhe von 1 km hin.

Eine Eingrenzung der potentiellen Anomaliemodelle kann nur durch eine gemeinsame Auswertung mit mineralogischen Experimenten und geodynamischen Modellierungen erfolgen.

Chapter 1

Introduction

The lowermost zone of the Earth's mantle forms one of the most fascinating scopes in global seismology because of the manifold and possibly interdependent attributes. Therefore, in the first part of this introduction the most important features of that region are presented because it is still unclear how these processes are related. Afterwards an overview of the key characteristics of the study related ultra-low velocity zones is given.
The average core-mantle boundary (CMB), i.e. the interface between the solid, silicate-rich lower mantle and the fluid outer core, is located at a depth of 2891.5 km [Kennett et al., 1995]. The CMB shows the largest contrast within the earth, not only in terms of the solid-liquid boundary but also respect to the chemical compositions. Below the CMB, iron (Fe^{2+}, Fe^{3+}) is the dominating element instead of silicium. The P-wave velocity is significantly reduced at the CMB (from 13.6 km/s to 8.1 km/s) but increases again within the outer core. In contrast, the density increases from 5.5 g/cm^3 to 9.9 g/cm^3 at the CMB. Therefore a very low impedance contrast of about 5% occurs. The S-wave velocity drops down from 7.2 km/s to almost zero. Because of these significant depth-dependent contrasts, the boundary between the lower mantle and the outer core is a first-order discontinuity. The pressure at the CMB amounts to 136 GPa. At the very beginning of research the base of the mantle (formerly denoted by D) were separated by geophysicist due to its different, much steeper, thermal gradient compared with the mid-mantle constitutions. Thus, the lowermost 300 km have been marked as D″. This region shows a thermal gradient of about 13°C/km which is similar to that of the lithosphere. The temperature in D″ increases by about 1000 K to almost 3700 K at the core-mantle boundary. With increasing depth the geotherm converges to the solidus and potentially even intersects it close to the CMB which would generally lead to partial meltings (see figure 1.1). Conversely, the D″ region is marked by a smaller velocity gradient in global Earth models compared to remaining lower mantle [Stein and Wysession, 2003].

In addition to the function as a thermal boundary layer there are further indications for the complex behaviour in D″. Some years ago two japanese research groups have been postulated, independent of each other, an isochemical, solid-solid phase transformation of γ-olivine, i.e. magnesium-silicate-perovskite $(Mg,Fe)(Si,Al)O_3$, at the top of the D″ region. This post-perovskite (pPv) called phase (also $(Mg,Fe)(Si,Al)O_3$) results in an increase of density of 1-1.2% (1.4% at the phase transition) as well as an increase of SH-wave velocity of 1.4% (1.9% at the phase transition) and +0.3% for P-waves for pure $MgSiO_3$ at 120 GPa and T=300 K, respectively [Murakami et al., 2004] and [Oganov and Ono, 2004]. This additional phase transformation in the lowermost mantle is widely accepted now. In general, the generation of pPv is supposed to be the cause of the observed seismic velocity anomalies, i.e. the D″ discontinuity, as well as the anisotropy effects (since experimentally found SH velocity is larger than SV velocity due to horizontal shear flow) [Oganov and Ono, 2004]. They have also proposed that pPv is a secondary

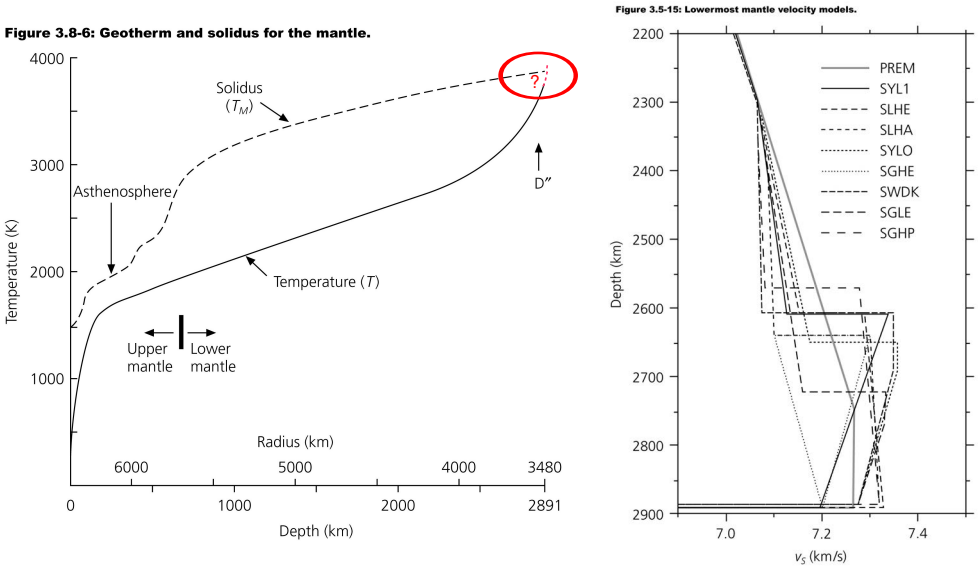

Fig. 1.1: Left: Behaviour of the temperature gradient and solidus between Earth's crust and CMB. Within the D″ region the thermal gradient may intersects the solidus which would result in partial melting (figure modified). **Right:** Shear wave velocity models of several studies for D″. PREM is the Preliminary Reference Earth Model. A discontinuity is assumed for the D″ region. Figures adopted from [Stein and Wysession, 2003].

crystallization product of the cooling mantle when it is interrupted by cold slabs. The longer this cooling process continue, the thicker becomes the D″ region. On the contrary, Murakami et al. [2004] have assumed a variable D″ thickness due to temperature effects on phase transition pressures. Potentially, both conclusions may add to the complete scenario.

Furthermore, the D″ region is regarded as ultimate destination for ancient subduction slabs. Reactions of cold lithospheric slabs with the mantle would result in an increase of seismic velocities, and probably density as well as anisotropy and may cause perturbations of the convective mantle flow. These assumptions are in contrast to partial melting related velocity reductions. The assumed D″ discontinuity can also behave as a chemical boundary between two distinct heterochemical regions or as a separation of chemical and phase anomalies which can be distributed by convective flows. Nevertheless, both possibilities include descended slabs [Gurnis et al., 1998].

However, the transition at the top of the D″ region reveal ambiguous signatures. The focus on that topic began in the 1970's. Early observations of radial velocity anomalies and laterally varying P waves were made by Wright and Lyons [1980/81]. Already in 1983, Lay and Helmberger [1983] postulate a first-order discontinuity for longperiod shear waves at a depth of 2610 ± 25 km with an velocity increase of 2.75 ± 0.25% (compare models SLHA and SLHE in figure 1.1). They observed triplications of rotated SH-waves for the region beneath the Aleutians archipelago. An alternative opportunity is the existence of a transition zone with a thickness less than 50 km when shortperiod data are used. These observations and assumptions were confirmed by Weber and Davis [1990] and Weber [1993] for further areas above all beneath the northern Atlantic region and northern Siberia. They detected the additional reflection phase PdP at the D″ discontinuity which arrives after P and before the core reflected PcP. The exact arrival time depends on the source distance. The velocity contrast for P-waves amounts up to 4% and not less than 1% at a discontinuity depth of 2610 ±15 km. The related S-velocity contrast

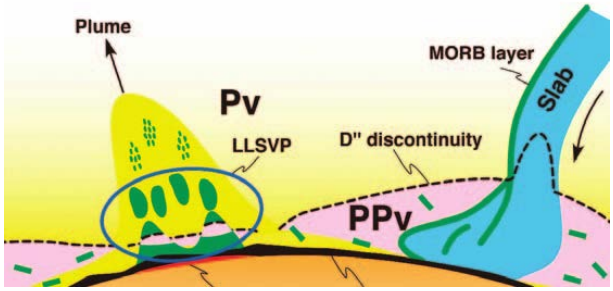

Fig. 1.2: Sketch of potentially related processes in the D″ region. It is widely accepted that a high-pressure phase transition from perovskite (Pv) to post-perovskite (PPv) atop the D″ region causes a further discontinuity or narrow transition zone within the lower mantle. This isochemical phase transformation is a temperature related process where the thickness of D″ increases with decreasing temperatures. Descending ancient subduction slabs can result in such temperature reductions. Conversely, within large low-shear-velocity provinces (LLSVP) - and associated rising hot plumes - a D″ discontinuity should be rather deeper or even completely diminish. Mid-oceanic ridge basalts (MORB) can accumulate within LLSVP and re-ascend in plumes. Moreover, a back-transformation to perovskite is conceivable for that provinces. Figure adopted from Hirose and Lay [2008].

is about 2.6% at a depth of 2575 ±15 km (see model SWDK in figure 1.1). Analogous to the previous study, a transition zone at the top of D″ is also possible as long as its thickness is smaller than 1λ where λ means the wavelength of the incident signal. For transition zones larger than 1λ strong distant-dependent amplitude reductions for PdP can occur. During the following years many other regions with this non-standard phase were observed using deep earthquakes and nuclear explosions (e.g. [Krüger et al., 1993]; [Krüger et al., 1995]; [Revenaugh and Meyer, 1997]; [Kito and Krüger, 2004]). Though not all studies reveal a positive velocity jump at D″, but also negative contrasts could be detected [Kito and Krüger, 2001]. It was shown that also the reflector depths are ambiguous beneath some regions, e.g. [Kito et al., 2007]. In other cases no clear discontinuity in P-wave velocity were found. However, even so no large P velocity jump was observed an increase of the S-wave velocity is possible [Ding and Helmberger, 1997]. Gurnis et al. [1998] gives an overview for regions where D″ structures have (not) been observed.
As a result of all these studies, it is obvious that these (non)-observations are not only due to the limited spatial arrangements of source and receiver combinations. The D″ discontinuity seems to be not a global signature or is at least superimposed by further core-mantle related processes. The reasons for these visual inconsistencies remain vague as well as manifold. Some possibilities are variations of the local velocity gradient and a resulting smaller velocity increase [Oganov and Ono, 2004], a pinching or dispersion of the anomalous sharp discontinuity, unequal distributed heterogeneities within and at D″ as well as a strong topography atop D″ which would result in focussing and defocussing effects and accompanying significant depth variations [Gurnis et al., 1998; Thomas, 1994]. Hernlund et al. [2005] have shown a double-crossing of the geotherm and the pPv phase transition boundary in D″ which would result in different depths of seismic velocity anomalies. For very high temperatures no perovskite-pPv transition occur and therewith no creation of a D″ discontinuity. A summary of the D″ related features is drafted in figure 1.2. A comparison of waveform studies with seismic tomography reveal two important findings: Around the whole pacific, including the Caribbean area, the tomography results correlate fairly

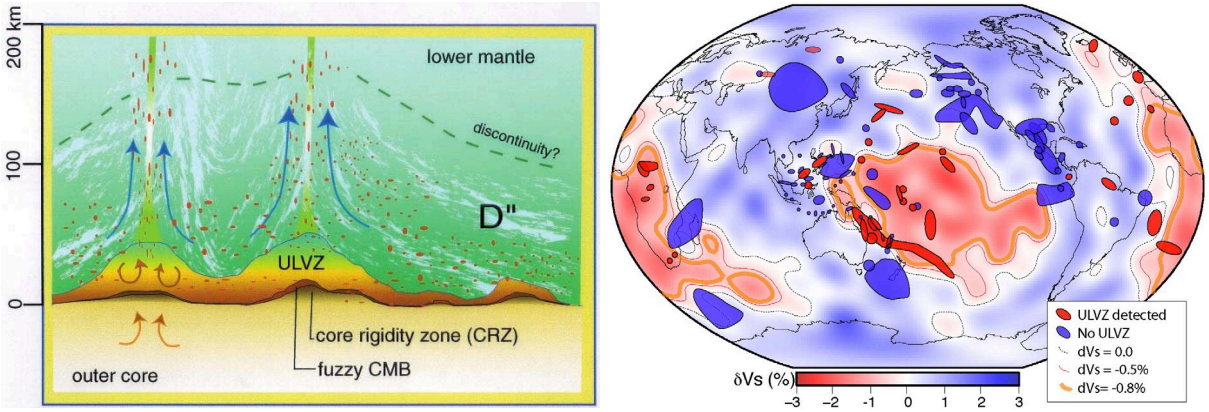

Fig. 1.3: Left: Sketch of the generation of an ultra-low velocity zone (ULVZ). Hot, liquid iron alloy from the outer core infiltrates the solid, silicate-rich lower mantle and induces regions of partial melting. Here the density is probably higher and the seismic velocities are in turn reduced. Other core-mantle related interactions such as a fuzzy CMB (zones of intense chemical and physical interactions between core and mantle) and a CRZ (core rigidity zone with a finite shear velocity at the top of the outer core) are also shown. Moreover, the possibility of ULVZs being the root of upwelling plumes is also denoted. Figure from Garnero [2000]. **Right:** Results of global S-wave tomography and the large low shear velocity provinces (LLSVPs) beneath the Central Pacific and the African continent. The global distribution of detected (red patches) and undetected (blue patches) ULVZs is overlain. Figure from McNamara et al. [2010].

well with the observed strong velocity discontinuities, at least using S-waves. Also the predicted large thickness of D″ corresponds to faster than average velocities [Sidorin et al., 1999]. It is assumed that the old, cold descended slabs cooling the lowermost mantle and lead to a shallow perovskite-pPv transition. In contrast, the large low-shear velocity province (LLSVP) beneath the central pacific shows much thinner D″ regions, partly only 60 km above the CMB. Though, also here in the vicinity of the prominent Hawaiian hot upwelling plume and related velocity reductions, S velocity discontinuities are well documented which is in disagreement to the mentioned hypothesis [Gurnis et al., 1998; Lay et al., 1998].

Another feature of the highly complex and manifold structure above the core-mantle boundary is the possible interaction of liquid iron, rising from the outer core, with the solid silicate-rich lower mantle. The hotter and denser iron alloy leads to an increase of density at the mantle-side boundary and is therefore probably able to remelt the stiff silicate material. As a consequence, significant reductions of P- and S-wave velocities are expected. These iron contaminated regions can create small-scale ultra-low velocity zones (ULVZs) within D" right atop the CMB. Early mineralogical experiments by Knittle and Jeanloz [1989] and Knittle and Jeanloz [1991] have shown that such a merging of silicates and iron is possible under high-pressure and temperature conditions. Numerous further studies, e.g. by Williams and Garnero [1996]; Jacobsen et al. [2002]; Mao et al. [2006], have investigated a possible range of velocity reductions by the influence of additional iron and partial melt ratios. The usual contrasts are given to P- and S-wave velocity reductions of 10% and 30%, respectively. However, a recent study by Mao et al. [2011] supposes only a 6 - 7% increase for the bulk sound velocity (where an anticorrelation of shear wave velocity and bulk velocity exists) and +4 - 6% for the density. It is assumed that the ULVZs are only thin layers in the order of 10s of km or below [Williams and Garnero, 1996]. The lateral extension is ambiguous and not well resolved because of the limited data coverage. A sketch of

an ULVZ is shown in figure 1.3.
In this regard, the possibility of a non-discontinuous CMB, rather a core-mantle transition zone (CMTZ), was early assumed by Kanamori [1967]. Further studies, e.g. by Vidale and Benz [1992], Garnero and Jeanloz [2000] and Thorne and Garnero [2004], have discussed this potential behaviour of the CMB with assumed transitions less than 4 km. Other studies developed the idea of a small-scale core-mantle material interaction which affects the core-side of the boundary. The so-called core rigidity zone (CRZ) is assumed to be rather stiff than mushy [Buffett et al., 2000; Garnero and Jeanloz, 2000; Rost and Revenaugh, 2001]. Thereby, a finite shear velocity in the outermost core is predicted and the thickness of a CRZ could be less than 3 km. It was shown in those studies that such very thin and highly heterogeneous features are able to produce significantly waveform effects without any partial melting. Both additional CMB features are shown in figure 1.3.
A different interpretation of ULVZs is the hypothesis that low-velocity anomalies could be the source of mantle plumes [Revenaugh and Meyer, 1997; Rost et al., 2005]. Moreover, Brandon and Walker [2005] have measured enriched Os isotopic ratios from Hawaiian plumed-derived materials, which could correlate with the predicted Os isotopic compositions of the outer core. The theory of a correlation between Hot Spots and ULVZs is also supported by Williams et al. [1998]. A completely different theory about the origin of low-velocity anomalies by Labrosse et al. [2007] is discussed in detail in chapter 5.
It is important to note that all of the proposed core-mantle attributes neither exclude nor include each other and it could be possible that different kinds of low-velocity anomalies exist at different regions.

The observation of any CMB characteristics is only provided by the seismology. During the last four decades numerous analyses of waveforms and amplitudes were made to investigate the region of the CMB and the attendant features. Laterally variations are preferably detectable by core diffracted waves as $SP_{diff}KS$ and $SKP_{diff}S$ [Thorne and Garnero, 2004]. The core transmitted waves PKP can indicate scattering in D″ as well as low-velocity structures [Wen and Helmberger, 1998]. A study of PKKP phases by Earle and Shearer [1997] allows for assumptions about a small scale topography on the CMB. Further useful phases are the inner core transmitted and outer core reflected SKP and PKiKP, respectively.
The most sensitive phases for vertical resolution are provided by the core reflected waves PcP and ScP (e.g. Rost et al. [2006]). Numerous studies have been shown evidences for ULVZs where the attributes of those regions are manifold as ambiguous. An overview of the assumed and non-detected ULVZs using PcP and the applied methods is listed in table 1.1. The map given in figure 1.3 shows the previously detected and undetected ULVZs [McNamara et al., 2010]. The effective Fresnel zones respecting to the potential ULVZs cover about 44% of the CMB whereas only 12% of the CMB reveal in fact an ULVZ with a thickness larger than 5 km Gurnis et al. [1998]. Many of the predicted ULVZs occur at the edges of the LLSVPs beneath central Pacific and the African continent. Recent geodynamical convection modelling by McNamara et al. [2010] reinforce this connection where dense low-velocity anomalies can accumulate along the reservoir boundaries. However, it can be seen from the overview map that some ULVZs do not correlate with the edges of the LLSVPs. Some of them seems to be randomly distributed (e. g. north of Indonesia) - maybe only because of the lack of data coverage or as a consequence of diverse source processes.

The motivation of this thesis is based on the hypothesis of ULVZs being the result of iron infiltration from the outer core. The goal is to analyse the behaviour of the core reflected PcP between 10° and 40° source distance. In contrast to common proceedings, here at first the impact on PcP using several low-velocity configurations should be analysed. Furthermore, the resolution limits of seismic data are discussed. On the basis of the calculation and interpretation of short-period synthetic seismograms a model space is evaluated for the ULVZ. Afterwards the Gräfenberg and NORSAR arrays are used to investigate PcP from deep earthquakes and nuclear explosions.
Chapter 2 describes the theoretical background of the applied methods: Based on the fundamental wave equations, the half-space reflection coefficients are obtained which in turn establish the reflectivity method. The Gauss beam method defines the second approach for modelling synthetic seismograms. An overview of array seismology give rise to an understanding of the data analysis. Chapter 3 contains the results of the synthetic seismograms where the first seven sections refer to the application of the reflectivity method and the last section shows the findings by the Gauss beam method including the 2D modellings. The analysed deep earthquakes and nuclear explosions recorded at the Gräfenberg and NORSAR array are treated in Chapter 4. A discussion of mineralogical aspects and an alternative hypothesis for the origin of ULVZs can be found in chapter 5. The concluding chapter 6 points out some opportunities to improve the resolution of the detected anomalies and to enlarge the sampling region at the CMB.

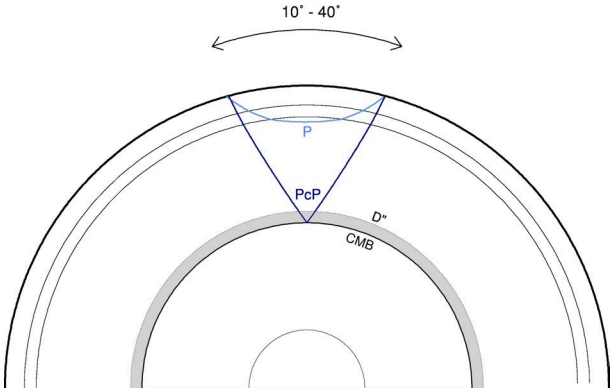

Fig. 1.4: The ray paths of P and PcP are shown for an epicentral distance of 30°. The distances and depths are true to scale. The upper mantle discontinuities at 410 km and 660 km are marked as well as the D" region as shaded area. The P-wave never reaches the bottom of the mantle and cannot be influenced by any CMB effects. The larger the source distance, and therewith the incidence angle, the longer is the PcP travel path through D".

Table 1.1: Some previous studies using PcP

Author	Bounce Region	Distance	Methods	ULVZ configuration	Notes / other features
				V_P / V_S / ρ / thickness	
Buchbinder [1968]	many regions	20-50°	single stations, reflection coefficient	-	PcP, PKKP amplitudes and travel times, PcP reversal at 32°
Chowdhury and Frasier [1973]	NNE Pacific / Caribbean / U.S.	26-40°	beamforming	-	PcP/P
Frasier and Chowdhury [1974]	north Pacific / north Atlantic	40-84°	beamforming	-	PcP/P
Menke [1986]	theoretical	40 - 85°	experimental modellings	-	PcP/P, CMB topography
Neuberg and Wahr [1991]	NNE Australia	35°, 70°	stacking, modelling matched filter	-	PcP/P, CMB topography
Mori and Helmberger [1995]	central Pacific	81 - 85°	stacking, modelling	-5-10% / - / - / 10 km	precursor / postcursor ?
Revenaugh and Meyer [1997]	central Pacific	>60°	Monte Carlo, stacking	-10% / -30-50% / -3 - +10% / <15 km	
Persh et al. [2001]	NE Pacific / central America	30-60°	stacking	<-10% / <-10% / - / <5 km	or gradients with >5 km
Thybo et al. [2003] / Ross et al. [2004]	Siberia	23-36°	stacking, modelling	-25% / -45% / - / 8 km	
Persh and Vidale [2004]	global	30-76°	global stacking	-	PcP/P, ScP/P
Rost and Revenaugh [2004]	Alaska	20-40°	stacking	-	PcP/P
Hutko et al. [2009]	central Pacific	>60°	double-array stacking	-3-4% / -4-8% / - / 15 km	
	north Pacific	20-40°		-4% / -4-8% / - / 15 km	
	Cocos plate/Mexico	30-60°		-	no ULVZ detectable
Rost et al. [2010]	north Pacific	30-50°	stacking, modelling	-	no ULVZ detectable / some configurations modelled
Rost and Thomas [2010]	Alaska	20-40°	migration	-	no ULVZ detectable >7 km

Methods

2.1 Waveforms and Reflections

The study of the core reflected phase PcP requires a knowledge of the reflections and transmissions at an interface. In order to reveal the mathematical description of reflection coefficients the basic equation of motion have to be considered first. The following equations are for a point source and a homogeneous layered earth [Müller, 2003]. It holds for plane waves at far-field considerations. Continuously inhomogeneous media can be expressed with a large number of homogeneous layers where the true quantity depends on the magnitude of the velocity gradient. The most general form of the equation of motion is valid for homogeneous, isotropic media and independent of the coordinate system:

$$\rho\frac{\partial^2\vec{u}}{\partial t^2} = (\lambda+2\mu)\overbrace{\nabla\underbrace{(\nabla\cdot\vec{u})}_{\text{volume change}}}^{\text{acting pressure}} - \mu\overbrace{\nabla\times(\nabla\times\vec{u})}^{\text{shear stress}} + \vec{f} \tag{2.1}$$

The vector $\vec{u}$ describes the displacement field of the elastic waves or just the state of deformation with respect to time. λ and μ are the Lamé elasticity parameters and ρ is the density. Vector $\vec{f}$ contains all other body forces that cause additional deformation. The right side of that equation is based on the spatial derivatives of the stress tensor which results from the stress-strain relation of Hook's law. The spatial derivatives of the stress tensor p_{ij} leads to forces which change the displacement vector. The left side gives the time derivatives of the displacements. The displacement field vector $\vec{u}$ can be expressed as displacement potentials

$$\vec{u} = \nabla\Phi + \nabla\times\vec{\Psi} \quad with \quad \nabla\cdot\vec{\Psi} = 0 \tag{2.2}$$

where Φ is a scalar potential that presents the compressional part (no rotations) and $\vec{\Psi}$ is a vector potential and is called shear potential (source free). Also the body forces $\vec{f}$ can be factored into

$$\vec{f} = \nabla\varphi + \nabla\times\vec{\Psi} \tag{2.3}$$

Inserting 2.2 and 2.3 in equation 2.1 using the mathematical relations

$$\nabla\cdot(\nabla\times\vec{\Psi}) = 0 \quad and \quad \nabla\times(\nabla\Phi) = 0 \tag{2.4}$$

and the equalization of all gradient (compression potential) and rotation (shear potential) terms, separately, leads to the potential form of the equation of motion:

$$\nabla^2\Phi - \frac{1}{\alpha^2}\frac{\partial^2\Phi}{\partial t^2} = -\frac{\varphi}{\lambda+2\mu} \qquad with \quad \alpha^2 = \frac{\lambda+2\mu}{\rho} \tag{2.5a}$$

$$-\nabla\times\nabla\times\overrightarrow{\Psi} - \frac{1}{\beta^2}\frac{\partial^2\overrightarrow{\Psi}}{\partial t^2} = -\frac{\overrightarrow{\Psi}}{\mu} \qquad with \quad \beta^2 = \frac{\mu}{\rho} \tag{2.5b}$$

The first terms on the left side of 2.5a (which is an inhomogeneous wave equation) and 2.5b show spatial derivatives whereas the second parts reveal derivatives with respect to time, respectively. The term on the right side presents the source. From this notation the two basic seismic wave types and their velocities can be defined which depend on the elastic Lamé parameters, λ and μ, and the density of the medium. α corresponds to the compressional P-wave and it is shown that the S-wave results from the shear potential of 2.5b. In the simplest case, i. e. a homogeneous, solid medium, the Lamé parameters are identical which gives the well-known velocity relation of $\sqrt{3}$ for α/β. The rigidity μ, the resistance to shearing, is zero for fluids and therefore only P-waves are observed in liquid regions such as the outer core.
Note that the solutions of 2.5a and 2.5b yield the seismic waves. Regarding to arbitrary directions the solved differential wave equations can again expressed with compression (2.6) and shear (2.7) potentials.

$$\Phi = A\ exp\Big[j\omega\Big(t - \frac{\overrightarrow{x}\,\overrightarrow{k}}{\alpha}\Big)\Big] \tag{2.6}$$

$$\overrightarrow{\Psi} = B\ exp\Big[j\omega\Big(t - \frac{\overrightarrow{x}\,\overrightarrow{k}}{\beta}\Big)\Big]\ \overrightarrow{n} \tag{2.7}$$

The shear potential is described by a vector and is therewith normalised by the unit vector $\overrightarrow{n}$. $\overrightarrow{x}$ is the location vector and A and B are the potential amplitudes. The wavefronts are perpendicular to the unit vector $\overrightarrow{k}$, which also presents the direction of propagation and can be decomposed into the angle of incidence. A multiplication with ω/α yields the wavenumber vector. From 2.6 and 2.7 as well as 2.5a and 2.5b, without the source term, follow the wave equations

$$\nabla^2\Phi = \frac{1}{\alpha^2}\frac{\partial^2\Phi}{\partial t^2} \quad and \quad \nabla^2\Psi_j = \frac{1}{\beta}\frac{\partial^2\Psi_j}{\partial t^2} \tag{2.8}$$

The polarization direction can be obtained when the gradient of equations 2.6 and 2.7 is taken. According to the normalisation vectors the resulting P-wave is longitudinal whereas the S-wave has a polarization perpendicular to $\overrightarrow{k}$, hence perpendicular to the propagation direction. Moreover the so-called displacement amplitudes can be defined as

$$\nabla\Phi = \underbrace{-\frac{j\omega}{\alpha}A}\ \underbrace{exp\Big[j\omega\Big(t - \frac{\overrightarrow{x}\,\overrightarrow{k}}{\alpha}\Big)\Big]}\ \overrightarrow{k} \tag{2.9}$$

$$\nabla\times\overrightarrow{\Psi} = \underbrace{-\frac{j\omega}{\beta}B}\ \underbrace{exp\Big[j\omega\Big(t - \frac{\overrightarrow{x}\,\overrightarrow{k}}{\beta}\Big)\Big]}\ \overrightarrow{k}\times\overrightarrow{n} \tag{2.10}$$

displacement amplitude *phase*

Elastic waves can be studied when the components u, v and w of the displacement vector $\overrightarrow{u}$ are derived from the potentials using the relation of equation 2.2. $\overrightarrow{u}$ is independent of the y-direction and therefore only derivations with respect to x and z are considered.

$$\begin{aligned} P-SV: \; u &= \frac{\partial \Phi}{\partial x} - \frac{\partial \Psi_2}{\partial z} \\ SH: \; v &= \frac{\partial \Psi_1}{\partial z} - \frac{\partial \Psi_3}{\partial x} \\ P-SV: \; w &= \frac{\partial \Phi}{\partial z} + \frac{\partial \Psi_2}{\partial x} \end{aligned} \tag{2.11}$$

As can be seen the P- and SV-waves are coupled within the media for u and w, whereas v gives the decoupled SH wave since there is no connection to the compression potential Φ. P-SV waves propagating in the x-z plane. A decoupling of P and SV occurs at first-order discontinuities (between two homogeneous half-spaces) or in case of an inhomogeneous medium where the elastic parameters only depends on x and the depth z. That means for an incident P-wave reflected and refracted P- and SV-wave are created at an interface and vice versa but a SH incidence causes no conversions. The continuity of the stress components as well as of the displacement components holds for the surface between the two half-spaces. However, the continuity for displacements depends on the properties of the half-spaces (solid-solid, solid-liquid, etc.).

A reflection or refraction (transmission) coefficient is described by the relation of the displacement or potential amplitudes of the incident to the reflected or refracted wave, respectively. The potential ansatz for an incident P-wave which is reflected and converted to SV as well as transmitted at an first-order discontinuity between two solid half-spaces is

$$\begin{aligned} P^{inc}: \Phi_0^{inc} &= A_0 \; exp\Big[j\omega\Big(t - \frac{\sin\varphi_0}{\alpha_1}x - \frac{\cos\varphi_0}{\alpha_1}z\Big)\Big] \\ P^{ref}: \Phi_1^{ref} &= A_1 \; exp\Big[j\omega\Big(t - \frac{\sin\varphi_1}{\alpha_1}x + \frac{\cos\varphi_1}{\alpha_1}z\Big)\Big] \\ SV^{ref}: \Psi_1^{ref} &= B_1 \; exp\Big[j\omega\Big(t - \frac{\sin\varphi_1'}{\beta_1}x + \frac{\cos\varphi_1'}{\beta_1}z\Big)\Big] \\ P^{trans}: \Phi_2^{trans} &= A_2 \; exp\Big[j\omega\Big(t - \frac{\sin\varphi_2}{\alpha_2}x - \frac{\cos\varphi_2}{\alpha_2}z\Big)\Big] \\ SV^{trans}: \Psi_2^{trans} &= B_2 \; exp\Big[j\omega\Big(t - \underbrace{\frac{\sin\varphi_2'}{\beta_2}}_{horizontal}x - \underbrace{\frac{\cos\varphi_2'}{\beta_2}}_{vertical\ slowness}z\Big)\Big] \end{aligned} \tag{2.12}$$

The second term within the phase expression reveals the horizontal slowness $\sin\varphi/\alpha$ for P-waves or $\sin\varphi/\beta$ for SV-waves, which gives multiplied by the frequency ω the wavenumber k. The third part including the cosine of φ corresponds to the vertical slowness l with

$$l_{1,2} = \Big(\frac{\omega^2}{\alpha_{1,2}^2} - k^2\Big)^{1/2} = \frac{\omega}{\alpha_{1,2}}\cos\varphi \quad and \quad l'_{1,2} = \Big(\frac{\omega^2}{\beta_{1,2}^2} - k^2\Big)^{1/2} = \frac{\omega}{\beta_{1,2}}\cos\varphi \tag{2.13}$$

A and B are again the potential amplitudes. The negative (positive) signs in front of the vertical slowness denote a propagation in positive (negative) z-direction, i. e. downward or upward, respectively. To find the correct amplitude ratios for reflection and transmission appropriate boundary conditions are needed. It requires continuity of the vertical and horizontal displacement $\partial\Phi/\partial$z and $\partial\Phi/\partial$x as well as of the normal and tangential stress components p_{zz} and p_{zx} for solid-solid media. Those conditions also hold for solid-viscous fluids interfaces as at the transition from solid lowermost mantle to ULVZ. The potentials for the downgoing and upgoing P-wave can be summarised to $\Phi = \Phi_0^{inc} + \Phi_1^{ref}$. The continuity for horizontal displacement u leads to the constraint regarding to 2.11:

$$\frac{\partial\Phi}{\partial x} - \frac{\partial\Psi_1^{ref}}{\partial z} = \frac{\partial\Phi_2^{trans}}{\partial x} - \frac{\partial\Psi_2^{trans}}{\partial z} \tag{2.14}$$

The other three condition equations are not shown. In case of a solid-liquid interface, as at the core-mantle boundary, only the normal displacement is continuous since a slip can occur parallel to the CMB. The incidence and reflected angles are equal and Snell's law is defined as

$$\varphi_0 = \varphi_1 \qquad and \qquad \frac{\sin\varphi_0}{\alpha_1} = \frac{\sin\varphi_2}{\beta_2} = \frac{\sin\varphi_1'}{\beta_1} = \frac{\sin\varphi_2'}{\beta_2} \tag{2.15}$$

Inserting the potential ansatz of 2.12 into the boundary constraints, tedious equations result which can be summarised to a matrix formalism. Finally, the reflexion and transmission coefficient (potential amplitudes) for an incident downgoing P-wave has the following form. The displacement amplitudes can be obtained by multiplying R_{PP} with the ratio of ω/α to ω/β (see 2.9 and 2.10).

$$R_{PP} = \frac{D_2 - D_1}{D_1 + D_2} \tag{2.16}$$

$$T_{PP} = \frac{2\rho_1 a_1}{D_1 + D_2}[(cu^2 + \rho_2)b_1 - (cu^2 - \rho_1)b_2] \tag{2.17}$$

$$D_1 = (cu^2 - \rho_1 + \rho_2)^2 u^2 + (cu^2 - \rho_1)^2 a_2 b_2 + \rho_1\rho_2 a_2 b_1$$

$$D_2 = c^2 u^2 a_1 a_2 b_1 b_2 + (cu^2 + \rho_2)^2 a_1 b_1 + \rho_1\rho_2 a_1 b_2$$

$$a_{1,2} = (\alpha_{1,2}^{-2} - u^2)^{1/2} \quad with \quad u = \frac{k}{\omega} = \frac{\sin\varphi}{\alpha_1} \tag{2.18}$$

$$b_{1,2} = (\beta_{1,2}^{-2} - u^2)^{1/2} \tag{2.19}$$

$$c = 2(\rho_1\beta_1^2 - \rho_2\beta_2^2)$$

As a consequence of these relations a reflection and refraction of P is dependent on the seismic velocities, density and angle of incidence (or slowness). The product of velocity and density is known as impedance. R_{PP} depends also on the shear wave properties. Equations 2.18 and 2.19 reveal meaningful features of R_{PP} since the parameters a and b correspond to the vertical slownesses for P and SV, respectively, which can become complex. This behaviour is correlated with a critical incidence. As long as the incidence angle φ is smaller than the critical angle φ^* the vertical slowness is real and positive and therewith the reflection coefficient. For incidents larger than the critical angle the vertical slowness becomes positive imaginary for negative frequencies ω and vice versa. For that and in case of grazing propagation ($\varphi = \varphi^*$) the transmitted waves are now inhomogeneous and decay exponentially with depth. In case of a frequency dependency

(beyond the critical angle), the impulse deforms with increasing incidence angle respect to the incident plane wave. This occurs due to the Hilbert transform which is an all-pass filter. Every frequency retains its amplitude but the phase is changing. For an incidence of 90° the impulse shape is again equal to the incident wave but the phase has been changed about 90° (sign reversal). Note that for solid-solid media several critical angles exist because of the P-SV conversions [Aki and Richards, 2009], [Müller, 1985], [Müller, 2003], [Stein and Wysession, 2003].

2.2 Reflectivity Method

The computations of synthetic seismograms in this study are based on the so-called reflectivity method by Müller [1985]. The fundamental idea of calculating synthetic waveforms is the assumption of spherical waves that incident on a layered half-space. These spherical waves are emitted by an explosive point source located within an arbitrary homogeneous layer and generate many incidence angles and wavenumbers instead of single values in case of a plane wave. In order to solve the equation of motion the Bessel function for cylindrical coordinates is applied. The resultant displacements at the free surface follow from a double integration over the slownesses in the frequency domain and an integration over the frequencies in time domain. The calculation is based on a recursive system of equations where for every layer a layer matrix is determined. Those matrix depends on the layer thickness, seismic velocity and vertical wavenumber or mainly on the reflection coefficient of the layer. The recursion takes place in frequency domain. Each layer matrix is separately solved and finally summed. The slowest allowed velocity is the shear wave velocity at the slowest layer and therewith the lower boundary for the slowness integration. The lower limit for the frequencies is zero and the upper boundary result from the source spectrum. The source function can be multiplied with the recursion solution in the wavenumber domain.
A more detailed view of the applied method for the P-SV case follows from the tutorials of Müller [1985] and Müller [2003] using the example of an explosion point source. The reflection (2.16) and transmission (2.17) coefficients from section 2.1 hold for plane waves in a homogeneous half-space with one interface. The starting point for the recursion is the potential ansatz (equation 2.20) for i layers from zero to n. Note that the time factor $e^{j\omega t}$ cancels out. The boundary conditions for solid-solid interfaces are given by the continuity of the vertical and horizontal displacement $\partial\Phi/\partial$z and $\partial\Phi/\partial$x as well as the normal and tangential stress components p_{zz} and p_{zx}.

$$
\begin{aligned}
P-wave : \Phi_i &= e^{-jkx}\left[A_i\ e^{-jl_i^{\alpha}(z-z_i)} + B_i\ e^{+jl_i^{\alpha}(z-z_i)}\right] \\
S-wave : \Psi_i &= e^{-jkx}\left[C_i\ e^{-jl_i^{\beta}(z-z_i)} + D_i\ e^{+jl_i^{\beta}(z-z_i)}\right]
\end{aligned}
\tag{2.20}
$$

The terms with A_i and C_i refer to downgoing waves and B_i and D_i to the upgoing waves in layer i. The horizontal wavenumber k remains constant in analogue to Snell's law. However, the vertical wavenumber l_i change and can become complex (negative imaginary) for $\sin\varphi = \alpha_1/\alpha_i$.

The extension to a layered homogeneous half-space leads to a sophisticated matrix formalism which contains the potential amplitudes of the upgoing (B_i and D_i) and downgoing (A_i and C_i) P and SV waves. The weighting of these potential amplitudes are caused by the reflection and transmission coefficients of the single layers as they are given in equations 2.16 and 2.17.

More precisely, the reflections and refractions of layer i have to be related with that of the underlying layer i+1. Those resultant reflectivities and transmissivities matrices connect the local reflectivity and transmissivity matrices atop of layers i and i+1 and depend on the layer thickness and vertical wavenumber and therewith on the frequency and seismic velocity. A frequency dependency cause constructive and destructive interference of the appropriate wave train. The recursion starts at the bottom of the layered half-space with increasing layer i toward the free surface. As a result the reflectivities and transmissivities matrices become more and more complex.

Using explosive point sources, cylindrical coordinates are more advisable than Cartesian coordinates due to the radially symmetric radiation. The potential ansatz is now expressed as function of the first kind and zeroth order Bessel function $J_0(kr)$.

$$\Phi_i = J_0(kr)\Big\{\underbrace{A_i\ e^{-jl_i^{\alpha}(z-z_i)}}_{} + \underbrace{B_i\ e^{+jl_i^{\alpha}(z-z_i)}}_{}\Big\} \tag{2.21}$$

$$\Psi_i = J_0(kr)\frac{1}{jk}\Big\{\underbrace{C_i\ e^{-jl_i^{\beta}(z-z_i)}}_{} + \underbrace{D_i\ e^{+jl_i^{\beta}(z-z_i)}}_{}\Big\} \tag{2.22}$$

$$\textit{incident wave} \qquad \textit{reflected wave}$$

Using the Sommerfeld integral spherical waves of the source displacement potential are converted to cylindrical coordinates. From equations 2.21 and 2.22 the potentials can be separated into a first part which presents the incident wave and a second part as the reflected wave. In contrast to the plane waves, the vertical wavenumber is now expressed as function of k (compare eq. 2.13) and many incidence angles occur. The integration over real ray parameters, or slownesses, occur in frequency domain since the reflectivities and transmissivities contain the frequency. The derivative with respect to depth of the potential yield the displacement in frequency domain. To come up with the displacements in time domain, the integration over the frequencies is combined with an inverse Fourier transform.
A final important step for obtaining synthetic seismograms is the conversion from spherical to flat velocities, densities and accompanying depths ζ. The global standard models always contain spherical values. Thus the earth-flattening approximation (EFA) by Müller [1977] has to be applied in order to satisfy the horizontal layer assumption of the reflectivity method. This transformation is mandatory beyond epicentral distances of about 300 km. R means the earth's radius and z is the depth of the interface.

$$V_{flat}(\zeta) = \frac{R}{R-z}V_{sphere}(z), \quad \rho_{flat}(\zeta) = \left(\frac{R}{R-z}\right)^n \rho_{sphere}(z) \quad with \quad \zeta = R\ln\frac{R}{R-z} \tag{2.23}$$

An advantage of the reflectivity method is the stable recursive system of equations for all frequencies and slownesses in contrast to a high-frequency approximation, e.g. by the Gauss-Beam method. Complete seismograms can be synthesized with all body and surface phases as well as head waves. The method is stable also in cases where the classical ray theory breakdown such as for caustic and shadow zones or diffraction and tunneling effects. In addition, the anelasticity of the earth can be included.
However, there are some adverse features of this numerical method. The generation of inhomogeneous waves is avoided in the region above the reflection [Aki and Richards, 2009]. The

seismograms are computed for an one-dimensional earth, i. e. only depth-dependent medium attributes can be considered. Any 2D and 3D effects like anisotropy and layer undulations cannot be regarded. But exactly these features of the medium cause strong focussing and defocussing effects or for example polarity reversals [Thomas et al., 2011]. Phases which propagate through the earth's center are not calculated since that depth becomes infinity using the EFA. The computing time can become very long since that effort is proportional to the number of layers and sampling rate. Moreover, numerical noise effects like aliasing and cut-off phases can be created as can be seen in the next chapter.

2.3 Ray Tracing with Gauss-Beam Method

Beside the well established reflectivity method, which is based on the full wave theory, there is another opportunity of studying synthetic seismic phases. The Gauss-Beam Method (GBM) combines the classical ray theory with aspects of the wave theory whereby a breakdown at caustics is prevented and an evaluation of dynamic effects, i.e. amplitudes, is possible. Moreover with that advanced ray tracing approach two-dimensional effects as topography atop discontinuities can be included.
A wavefield, that is radiated by a (point) source, can be decomposed into many single rays, the so-called Gaussian beams (GB). Such a GB consists of a central ray Ω with the maximum energy that travels through the medium at which a surrounding Gaussian bell curve enables the inclusion of adjacent energies. Therefore, even if no ray endpoint Q exactly incidents at a receiver S energy will arrive at that site because of station S lies inside of the Gaussian beam (figure 2.1). Hence displacements close to the central ray also contributes to the amplitude at receiver S (marked by shaded area). The amplitude of the beam decreases by an exponential function and is perpendicular to the tangent vector $\vec{t}$ to the central ray. Finally, at the receiver all beams are integrated over their take-off angles to get the total displacement at station S .

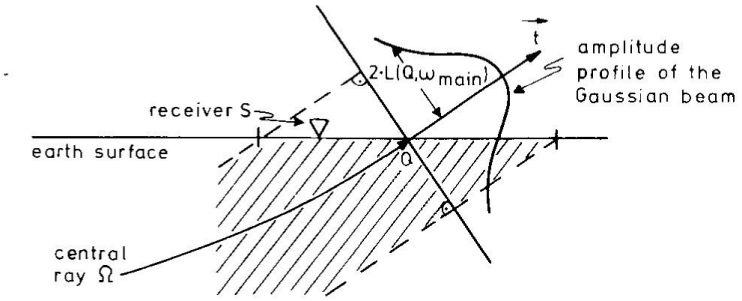

Fig. 2.1: Sketch of a Gaussian beam that arrives in the vicinity of a receiver S. Although the central ray Ω does not exactly hit the receiver energy arrive at station S since the receiver is inside the Gaussian bell curve look-alike. Hence displacements close to the central ray also contributes to the amplitude at receiver S (marked by shaded area). The amplitude of the beam decreases by an exponential function and is perpendicular to the tangent vector $\vec{t}$ to the central ray. The beam width L(Q, ω) controls the precision of the synthetic seismograms. Figure from Weber [1988].

As well as the classical ray theory, the GBM is based on the high-frequency approximation. Within very fast varying media of velocity v the wavelength λ should be very small where $v/|\nabla v| \gg \lambda$. A Gaussian beam in frequency domain is in principle controlled by the velocity and density

of the medium, the travel time and distance s along the central ray and its width L, that depends again on the distance s and the main frequency of the source signal. The beamwidth L(s, ω) is defined as the offset from the central ray where the amplitude of the Gaussian beam decreases. Beams for high frequencies are narrower than beams for low frequencies. Outside the GB the amplitude contribution at receiver S is less than 2 percent. Thus an appropriate beamwidth is crucial for the correct calculation of synthetic waves.
The beamwidth L(s, ω) can be expressed via the Gaussian beams parameter ϵ which also controls the phase-front curvature of the beam. Nine different options exist to quantify that complex parameter where ϵ can be determined for example at the beam endpoint Q, along the beam or by mixed criteria. In this study the latest option by Weber [1988] were used. Here the whole medium, through the ray is propagating, is used to establish the beam width L instead of using only the points at the source and the receiver. The medium is separated into triangles of different sizes which evaluates the velocity, density and also a constant absorption. Large triangles describe only slowly varying media with resultant broad beam width. However, fast varying structures result in narrow beams which are close to the central ray. Inside such a triangle the parameters vary linearly. In case of an inhomogeneous medium the gradients of velocity and density are used. The beam width L at the endpoint Q has now following relation:

$$L(Q,\omega) = l \cdot \left(\frac{\omega_{main}}{\omega}\right) \quad with \quad l = \sqrt{\frac{1}{N}\sum_{i=1}^{N} D_i^2} \tag{2.24}$$

The factor l quantifies the number N of triangle sides the ray encounters in relation to all minimum distances D_i of the central ray to the corners of the triangles. ω_{main} is the main frequency and ω all other frequencies of the source signal. The computing time using the GBM is much less than for the reflectivity method since the dynamic and kinematic ray tracing systems can be solved analytically. In comparison with the full wave theory the exactness of the amplitudes amounts to 3-5%. A description of the used program by Weber [1988] can be found in section 3.8.

2.4 Array Seismology

The application of seismic arrays enables the use of weak phases and even noisy recordings since the noise is suppressed and the desired signal will be enhanced. In this context a propagating plane wave is represented by its slowness vector $\vec{s}$, with a horizontal component s_{hor} which is the reciprocal of the horizontal apparent velocity v_{app} (cf. section 2.1, eq. 2.18).

$$s_{hor} = \frac{1}{v_{app}} = \frac{\sin i}{v_c} \qquad p = r \cdot \frac{\sin i}{v} = R_c \cdot s_{hor} \tag{2.25}$$

That apparent velocity correlates to the vertical incident angle i of the wavefront divided by the medium propagation velocity v_c. Referring to these parameters, the ray parameter p [s/°] can be defined which describes a distinct phase since its value remains constant while propagating through the earth. R_c gives the radius for the turning point of a specific ray. Another important parameter to evaluate arrays is the angle of back-azimuth (BAZ). This is the angle Θ in figure 2.2 measured clockwise between the north and source-receiver direction.
An array response function (ARF), or array transfer function, describes the resolution of the

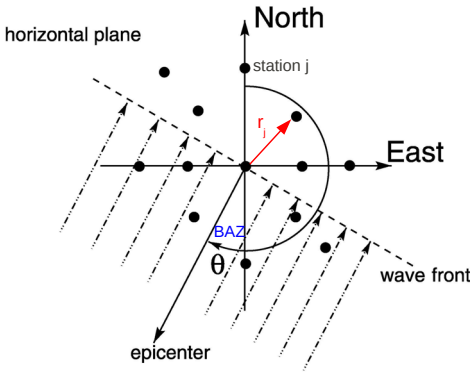

Fig. 2.2: View of the horizontal plane for an incident plane wave which arrives with an back-azimuth (BAZ) Θ. The reference site is located in the origin of the coordinate system. $\vec{r}_j$ gives the distance from that reference site to stations j. Figure modified from Rost and Thomas [2002].

seismic array for any signals according to different frequency and slowness ranges. The modelling of the ARF is based on the prerequisite that a signal S(t) is recorded by several stations M which are combined into an array. The array geometry is defined by a vector $\vec{r}_j$ and represents the distance between station j and the reference site of the array. Usually that reference site is located at the centre of the array. Because of the varying travel times of the wave toward the different stations, a time delay τ_j occur in terms of the arrival of signal S(t). Since $\tau_j = \vec{r}_j \cdot \vec{s}$, there is a relation between the array geometry, slowness vector $\vec{s}$ and BAZ. Those time delay τ_j of the individual traces is corrected for a specific slowness and BAZ, i.e. all signals are aligned, so that a discrete signal can be summarised to one trace B(t).

$$B(t) = M \cdot S(t) + \sum_{j=1}^{M} n_j(t + \vec{r}_j \cdot \vec{s}) \tag{2.26}$$

Therewith, ideally an amplifying of the signal and suppression of the noise n_j proportional to the root of the sites M can be achieved assuming that the signal is coherent and the noise is incoherent (uncorrelated). This principle is called beamforming or delay-and-sum method where the resulting beam amplitude B(t) is controlled by τ_j and the number of seismometer (equation 2.26). Furthermore, for the correct analysis of the ARF plane and monochromatic waves are considered. Note that for large arrays or in the near-field the incident wave behave rather as a spherical wave than as a plane wave and the Earth's curvature have to be included. An epicentral distance of more than 10 wavelength and much larger than the array geometry gives a good approximation for a plane wave.
The response function itself depends on the number of sites, the array geometry (aperture) $\vec{r}_j$ and the wavenumber $\vec{k}$ (or slowness since $k = \omega \cdot s$) difference, i.e. the difference of a discrete, desired slowness $\vec{s}_0$ to all other plane waves with slowness $\vec{s}$. At first the energy of the beam amplitude from 2.26 is calculated. With a Fourier transform into the frequency domain the travel time difference in time domain become a phase shift. Hence equation 2.27 describes the signal energy at the array where a parameter $\vec{k}$, or $\vec{s}$, is wanted which should maximise that energy.

$$|C(\vec{k}_0 - \vec{k})|^2 = \left| \frac{1}{M} \sum_{j=1}^{M} e^{i\omega \vec{r}_j (\vec{k}_0 - \vec{k})} \right|^2 \tag{2.27}$$

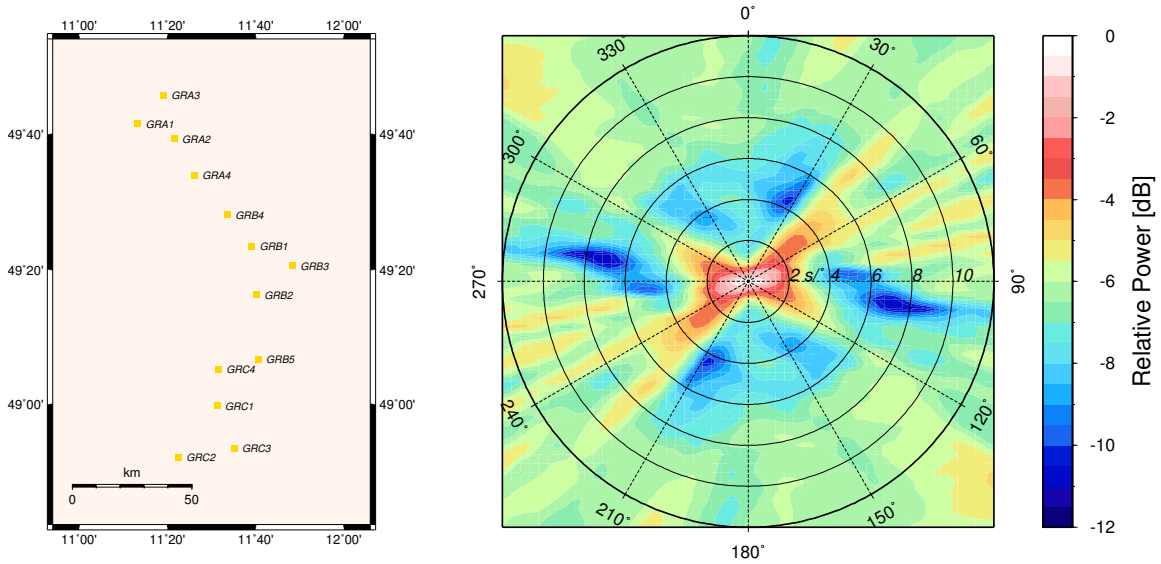

Fig. 2.3: Array geometry and response function for the Gräfenberg Array in Germany. The scaling shows relative power in dB, normalised by the maximum value of the absolute powers. Radial component displays slowness range from 0 s/° to 12 s/°. The azimuthal value of 0° corresponds to the north direction. The ARF was calculated for the frequency range of 0.5 Hz to 1.5 Hz. Reference site is station GRA1.

Basically, the wave incidents perpendicular from below. The true wavenumber $\vec{k}_0$ and therewith the slowness $\vec{s}_0$ is zero in that case. For this reason the apparent velocity is infinity. In case of the wave number difference $\vec{k}_0$ - $\vec{k}$ = 0 the resolution of the response function equates its optimum. The right side of 2.27 yields then the energy maximum of 1. An energy which is propagating with a different wavenumber than $\vec{k}_0$ is suppressed by the function, i.e. only a discrete slowness and BAZ will be enhanced and all other values are prevented [Rost and Thomas, 2002; Bormann, 2009].

Since a plane wave is defined by its slowness vector the ARF is usually considered in the slowness domain. Figure 2.3 shows the response function for the Gräfenberg array in Bavaria, Germany which consists of 13 broad-band stations (see section 4.1.1 for more details). The ARF was calculated only for the sx-sy plane, which are the components of the slowness vector. A vertical influence, i. e. the topography of the array site, was neglected. The perpendicular incident wave is located at the origin of the sx-sy coordinate system - here is the energy maximum. A resulting absolute slowness range from 0 s/° to 12 s/° is shown on the radial component. The azimuthal scale gives the BAZ where 0° corresponds to the north. The ARF was calculated for the frequency range of 0.5 Hz to 1.5 Hz using an equally spaced grid of 200 by 200 points. Every grid point gives a calculated power value which were normalised to their maximum value and converted to dB. This computation method indicates that the response function is a special case of a frequency-wavenumber analysis (f-k analysis).

The resolution of an array can be understood from the used arrays. The aperture of an array determines the shape and size of the energy maximum, which is also called main lobe. The smaller the array geometry the larger are these lobes. Thus small apertures are not able to resolve little slowness differences. Large arrays such as Gräfenberg or NORSAR were installed to observe regional and teleseismic wave groups. Concerning the Gräfenberg array in view of the main lobe shape, the quality of the slowness resolution depends on the direction of the incoming signal. The minimum width (smallest apparent aperture) of the main lobe correlates with the

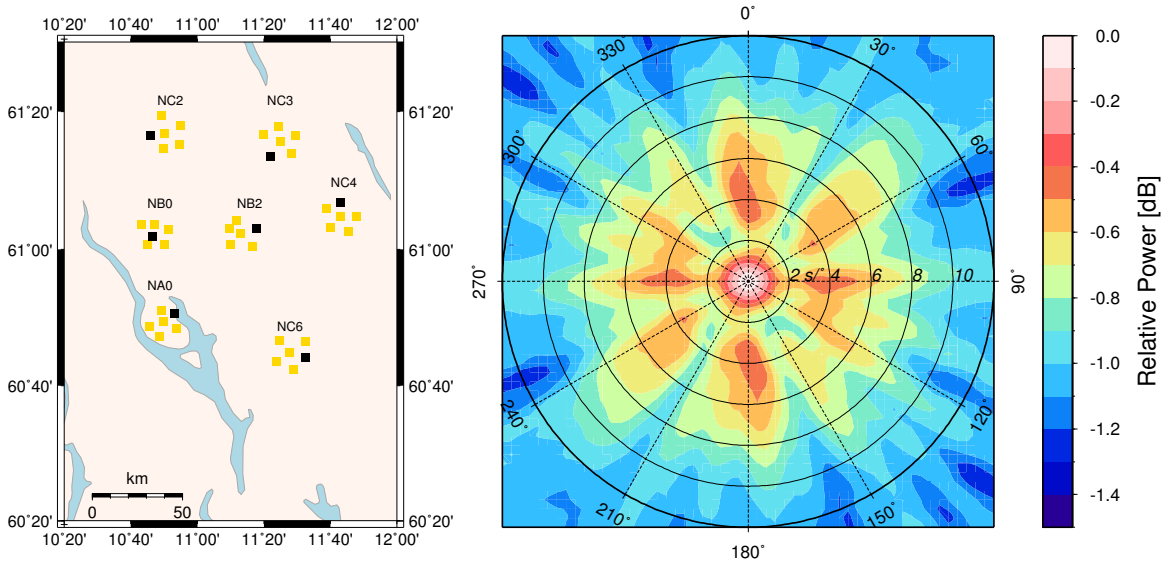

Fig. 2.4: Array geometry and response function for the NORSAR array with its 7 subarrays 6 seismometers in Norway. The golden squares mark the short-period instruments and the black ones show the broad-band seismometer. Notation as in figure 2.3. The ARF was calculated for the frequency range of 0.5 Hz to 1.5 Hz. Reference site is the centre station of subarray NB2.

direction of the maximum aperture and the largest lobe width is directed to the smallest array geometry. Regarding to the Gräfenberg Array the worst slowness resolution occur for signals from eastern and western directions. A good slowness resolution is expected for wave incident from the north and the south. The azimuthal resolution results from an converse manner, i.e. best determination of the BAZ occur for easterly or westerly incident wave groups.
Beside the main lobe at the origin several side lobes exist which are defined by the distances between the stations. The larger the mean distances, the smaller are the slownesses that can be observed. The side lobes for the Gräfenberg array a fairly strong and close to the main lobe which decrease the resolution. In addition the position of the side lobes and the size of the main lobe are dependent on the applied frequency range. The more higher frequencies are used the smaller become the energy maximum. Hence, also frequencies influence the resolution of an array.

Figure 2.4 shows the large NORSAR array in Norway which consists of 7 subarrays, each equipped with one broad-band (black squares) and 6 short-period (golden squares) stations (see section 4.2.1 for more details). Again a frequency range of 0.5 Hz to 1.5 Hz was used. The resolution of slowness and BAZ is independent from the direction since the response function is almost a circle and is related to the centre subarray NB2. The high-energy lobes around the centre lobe result from the surrounding subarrays. Side lobes are less prominent than for the Gräfenberg array since NORSAR consists of much more stations in relation to the aperture. Note that the scaled relative power values are much larger, by a factor of 10, as for the Gräfenberg array.

Chapter 3

Modelling of Synthetic Seismograms

Synthetic Seismograms were calculated using *psquik*, which is a simple and fast tool for modelling single impulses based on the reflectivity method after Müller [1985]. Therefore only an usual reflectivity method was used which generates solely PP reflexions, P-SV and SV-P as well as SV-SV conversions. On the surface of a layered half-space vertical and horizontal seismograms are modelled using a single explosion point source. Theoretical ground displacements were calculated and only vertical components are considered below. The derived ground velocities are stable and coincide with calculated velocity proportional seismograms.
16 equidistant, displacement proportional seismograms were calculated between 10° and 40°. In that distance range the reflection coefficient is increasing and therewith the amplitude of the core reflected PcP. The maximum is reached at an incidence angle of about 65° that corresponds to an epicentral distance of 60°. At this distance the travel time difference of P and PcP is less than 60 seconds and an interference with the direct wave train could occur which may influence the amplitude ratio. In general, PcP is a fairly weak phase since most of its energy is transmitted to the outer core as can be seen in figure 3.1. The absolute coefficient rise from 0.024 at 10° to about 0.26 at 40°. The specified distance was also chosen because PcP passes through the D″ region as shortest path length as possible. The greater the ray path the more significant become the influence of the D″ attributes on the core reflected wave. Moreover, the effective Fresnel zone is much smaller for steep incidence angles and therewith the lateral resolution of the CMB is increased. A more detailed discussion can be found in section 3.8.2.
The global earth model ak135 [Kennett et al., 1995] is used as input one-dimensional velocity-depth function and composed of P-wave and S-wave velocity, their quality factors (reciprocal damping parameters), density and the number of homogeneous layers which approximates the gradients. First and second order (gradient zones) discontinuities can be used. Between a gradient zone the earth parameters are linearly interpolated so that equally thick layers will be produced. In the beginning, first order discontinuities were only applied to the Moho and core-mantle boundary where the number of homogeneous layers is zero. Otherwise, the number of homogeneous layers was set to 10 except for the D″ region and CMB where 30 and 60 layers were applied, respectively. The flat earth transformation after Müller [1977] is activated since this is necessary beyond distances of 300 km.
In a first step, synthetics were calculated without any damping parameters for compressional and shear waves. This fully elastic media assumption were applied in order to extract the pure waveforms and amplitudes of PcP and its precursor and postcursor in the case of a discontinuity above the ULVZ. In a second step, where damping have been used, it was abstained from the application of frequency dependent quality factors.

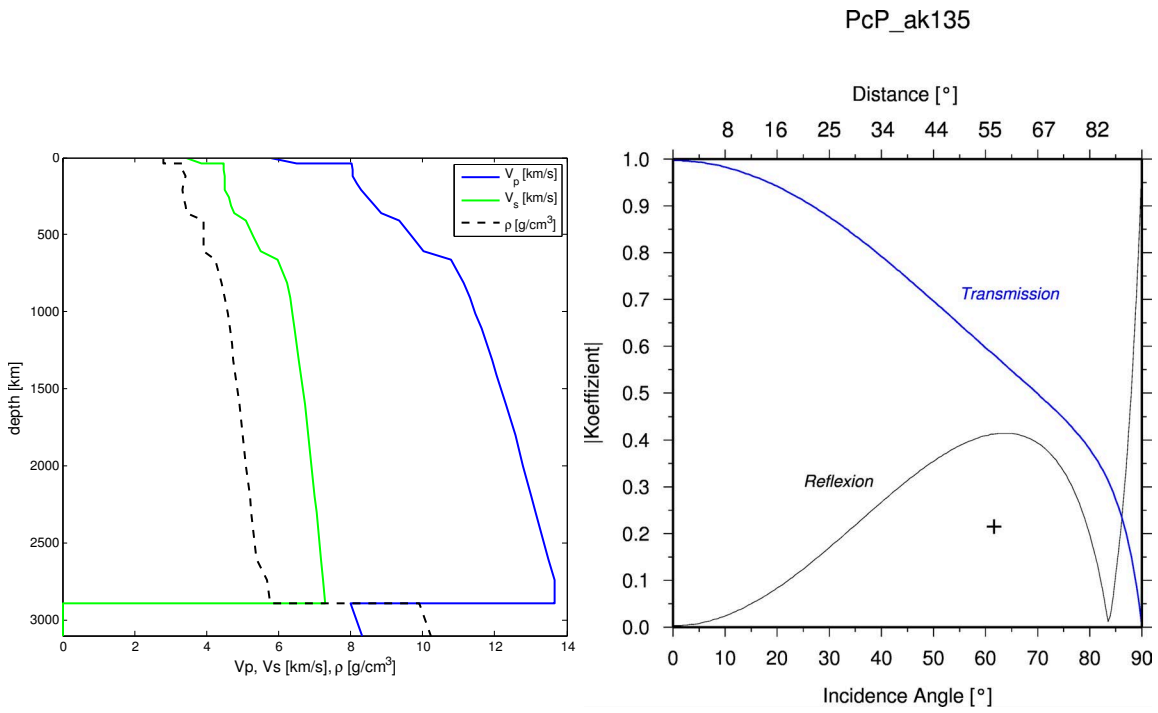

Fig. 3.1: Left: Used global earth model ak135. **Right:** Half-space reflection and transmission coefficients of the core reflected phase PcP using ak135. Most of the P-wave energy is transmitted to the outer core. The plus sign denotes a positive polarity of the PcP amplitude.

The source depth was located at 130 km. In such a depth no multiple reflexions due to the crust occur and P is directly transmitted through the mantle. Though this is not a realistic depth for explosion sources which mostly occur in the upper 1000 m, this assumption allows a detailed study of PcP waveform and its amplitude ratios. At first, a dominant period of 4 seconds was chosen as source duration. The sampling rate amounts to 5 Hz (0.2 s), thus a sampling of 20 per source impulse results. This wavelet approximates the source time function and it has to be sampled by at least 4 points to avoid acausal impulse effects. The number of samples used is 4096 which leads to a seismogram length of 819.2 s at a time increment of 0.2 s. The lower frequency of the bandpass was set to zero. The upper limit can at most reach the Nyquist frequency of 2.5 Hz. It was abstained from the usage of a cosine taper window. When an upper frequency of 2.0 Hz is used only artifacts are produced which do not interfere with the stable output signals. A cosine taper could not reduce the numerical noise. An important factor is the suppression of aliasing in time domain. Typically, this value is approximated by 20-50% of the trace length and set to 400 s here. For the integration over the slowness a definition of the upper and lower boundaries is required. Thereby, a cosine taper window (convolution of cosine impulse and heavy-side function) is applied. The lowest slowness for PcP is about 1 s/° at 10° according to ak135, so that the integration takes place from 0.75 s/° to 32 s/°. This corresponds to phase velocities of about 145 km/s and 3.5 km/s, respectively. A cosine taper is used to suppress numerical signals that arrive with these phase velocity limits and is defined with 140 km/s and 4.0 km/s, respectively. The total number of slownesses amounts to 1200. Seismograms were modelled with a velocity reduction of 12.2 km/s which corresponds to an average P-wave velocity at a distance of 24°. In addition, a reduction time of 20 s was used.

Figure 3.2 shows the vertical synthetic seismograms calculated with the parameters described

above. Notable waveform complexities and amplitude variations within the triplication range occur, whereby at 16° and 22° the amplitudes reach the maximum. The focussing effects are fairly strong although only second order discontinuities for 410 km and 660 km were used, but the velocity gradient is very high. Between P and PcP a strong impulse with negative polarity arrives which travels toward PcP and whose amplitude decreases with distance. Both arrival time and polarity qualitatively fit the surface reflection phase PP. However, a detailed study of the travel time shows time differences up to 13 s with decreasing distance. At 40° and 38° the synthetic arrivals fit well the values of the travel time tables but at 24° a misfit of 13 s occurs. Regarding to the source depth of 130 km, PP would be generated only beyond 24°, whereby here the signal can be already observed beyond 18°. Also the arrival time of the depth phase pP does not coincide with this impulse. Therefore, it is rather a cut-off phase than a real signal. Though, this effect is negligible for the study since it does not interfere with PcP and remains stable for all modelled ULVZ configurations. The calculated P and PcP pulses correspond to the specified waveform and duration of 4 s and no waveform broadening with distance can be observed.

As described in chapter 1, if iron alloy reacts with the lowermost mantle a reduction of velocities and an increase of density is expected. It is assumed that shear wave velocities are more effected since the rigidity reduces with increasing melts. Based on the assumption of Williams and Garnero [1996], 14 models for low-velocity regions above the CMB were constructed and calculated for gradient zones and first order discontinuities atop the ULVZ. Table 3.1 summarises the applied configurations in this study.

Table 3.1: Overview of the 14 ULVZ models with P- and S-wave velocity and density contrasts as well as the resultant impedances

Model (V_P / V_S / ρ)	V_P [km/s]	V_S [km/s]	ρ [g/cm^3]	impedance [km/s · g/cm^3]
smooth (CMB)	13.66	7.282	5.772	78.85
-10%-30%+30%	12.294	5.097	7.504	92.25
-10%-30%+20%	12.294	5.097	6.926	85.15
-10%-30%+15%	12.294	5.097	6.638	81.61
-10%-30%+10%	12.294	5.097	6.349	78.06
-5%-15%+30%	12.977	6.190	7.504	97.37
-5%-15%+15%	12.977	6.190	6.638	86.14
-5%-15%+5%	12.977	6.190	6.061	78.65
-10%-20%+30%	12.294	5.826	7.504	92.25
-10%-20%+20%	12.294	5.826	6.926	85.15
-10%-20%+15%	12.294	5.826	6.638	81.61
-10%-20%+10%	12.294	5.826	6.349	78.06
-5%-10%+30%	12.977	6.554	7.504	97.37
-5%-10%+15%	12.977	6.554	6.638	86.14
-5%-10%+5%	12.977	6.554	6.061	78.65

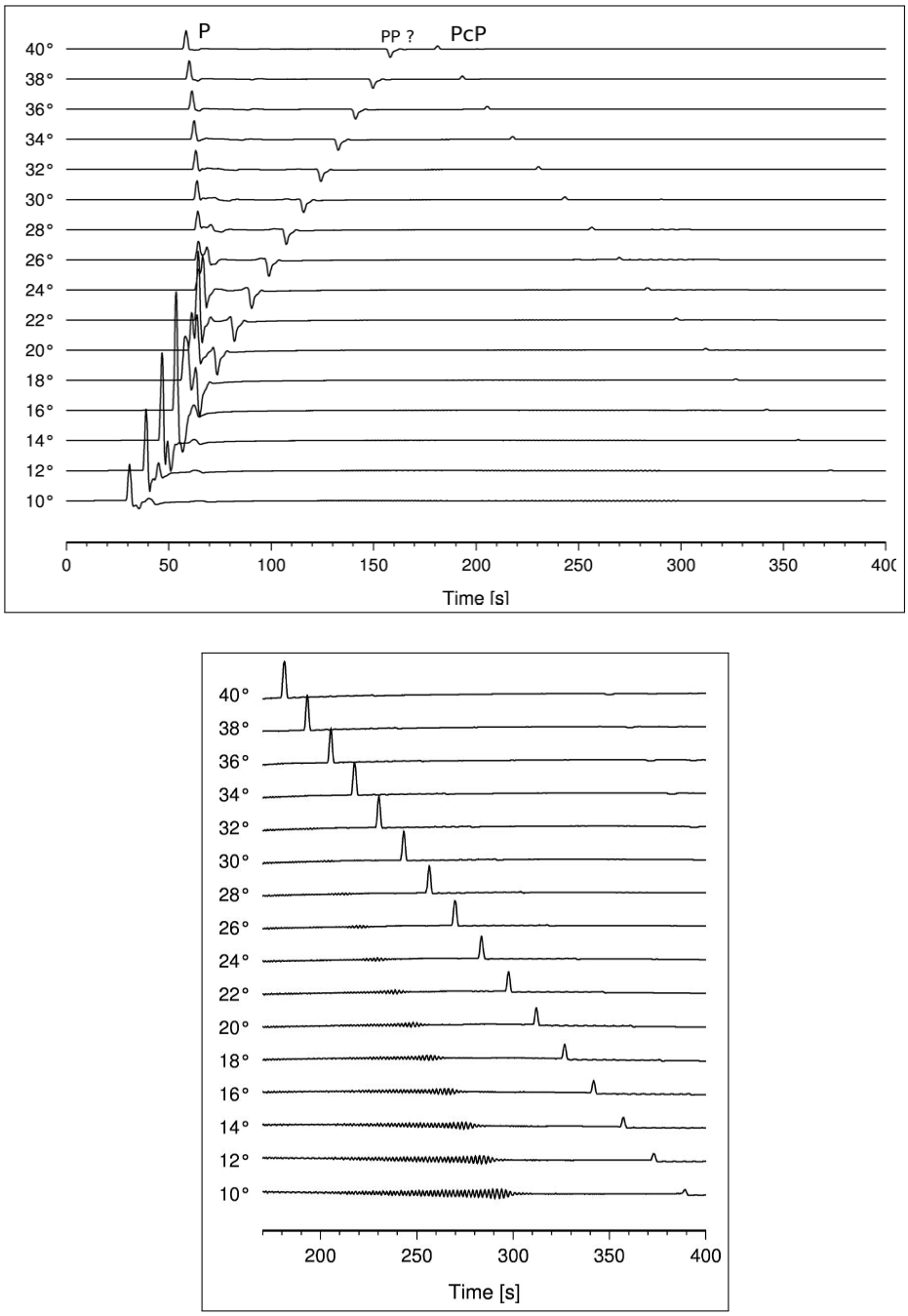

Fig. 3.2: Vertical synthetic seismograms of the smooth model are shown for the distance range of 10° to 40°. Parameters described in the text were used. The lower figure shows the PcP impulse in detail. Note that the scaling of the upper and lower figure is different. The numerical noise, above all for near distances, is steady and PcP remains unaffected.

3.1 Modelling with Gradient Layers

As a first step synthetic seismograms of ultra-low velocity zones with gradients were computed for seven different models (illustrated in figure 3.3) and five varying anomaly thicknesses. The parameters described above and table 3.1 were used.

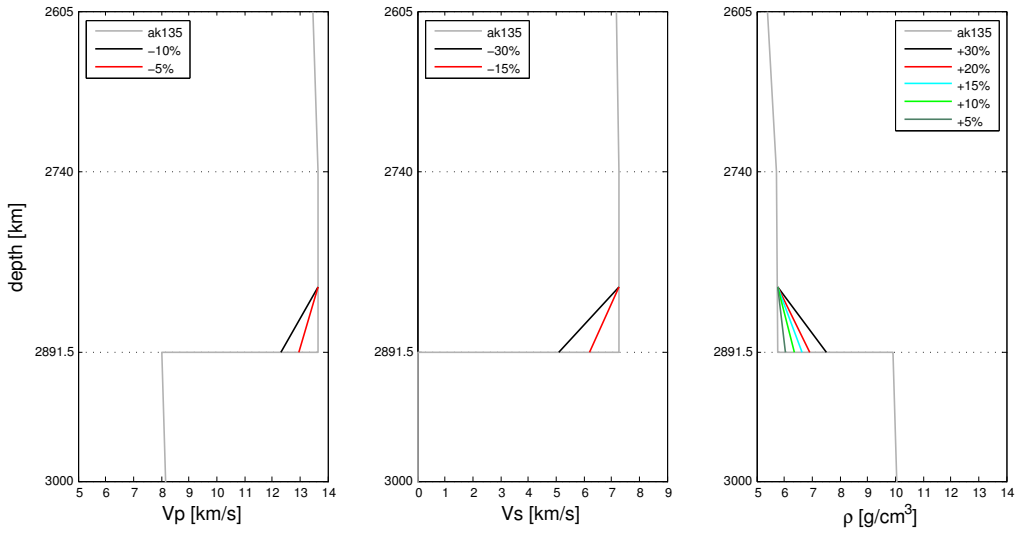

Fig. 3.3: Velocity-depth models for a gradient ULVZ with a thickness of 55 km. Only the velocity contrast ratios of 1:3 are shown here. The density-depth function is also illustrated.

In order to scale the calculated PcP waveforms, the amplitude ratios of PcP to P of the smooth global earth model and of the modified models were measured, respectively. The modified amplitude ratio is scaled by the smooth amplitude ratio. In fact, the amplitudes of the direct wave remain identical for all CMB anomalies since the maximum turning point of the ray at 40° is located at about 1000 km depth (see figure 1.4). Therefore a simple scaling of the modified PcP impulse by the smooth signal (PcP^{mod}/PcP^{smooth}) results as a function of epicentral distance, which is given in figure 3.4. A ratio of 1.0 means that the modified PcP impulse equals the smooth amplitude. It should be mentioned that the distances are not identical with the incidence angles of PcP of the smooth model. However the deviance is not large and the shown distances can be regarded as a rough approximation of the incidence angles (cf. figure 3.1). The legend annotation refers to a reduction of P- and S-wave velocity and an increase of density in percent, respectively. Five different ULVZ thicknesses are displayed in relation to a wavelength λ of about 55 km at the CMB for a wavelet period of 4 s. The amplitudes were measured between the baseline and the absolute peak offset, i. e. the absolute amplitude of the whole impulse were determined independent from the shape of the waveform. Therefore any polarity changes or waveform broadening were neglected. This means that most of the determined amplitudes have a positive sign. The only exceptions are the -10%-30%+30% and -5%-15%+30% models at a thickness of 55 km between 10° and 14°. Here the absolute amplitudes have negative polarities. The diagrams in figure 3.4 present several important attributes. Generally, the amplitudes show a highly complex behaviour above all within the steep-angle region between 10° and 20° and become smaller with increasing low-velocity layer. An important feature is that the amplitudes of the steep-angle area are solely dominated by the density contrasts and show strong dependencies on distance. For the highest density variances of the models -10%-30%+30% (black line) and

-5%-15%+30% (red line) even an amplitude increase occur for the very steep-angle range of 10° to 14°. This can be seen for every ULVZ thickness where the modified PcP impulses increase with layer thickness (except for 27 km). At 10° the PcP amplitude is almost doubled for the -5%-15%+30% configuration. This is in contrast to what would we expect for such extremely low velocity zones resultant from partial melting. Note that the velocity contrasts are halved and reveal absolutely no influence on this amplitude ratios. The smaller density contrasts of +20% and +15% form a second group (cf. black arrows in figure 3.4 at λ=55 km) between 10° and 16°, again independent of their velocity reduction. The light blue and pink coloured lines possess velocity variances of -10% and -30%, whereas the dark blue line refers to -5% and -15% of V_P and V_S, respectively. However, the amplitudes here are reduced as would be expected, except for the thinnest layer of 5.5 km. Here the modified amplitude at 10° for the models -10%-30%+20% and -5%-15%+15% is slightly higher than the smooth PcP. These two models have similar impedances (cf. table 3.1). The strong varying ratios from 0.6 at 10° to 0.2 at 14° (d = 55 km) coincide with the predicted reflection coefficients and result from polarity reversals (see section 3.4).

Beyond 20° the influence of the velocity variance begins to dominate. The impact of the velocity contrast is marked with filled and unfilled black arrows in figure 3.4 at λ=70 km. Two different slopes can be separated according to their model contrasts, where the lower contrasts of -5%-15% (filled arrows) result in highest amplitudes for the wide-angle area. In general the velocity reductions of -10%-30% cause smaller amplitudes with a little negative slope in the wide-angle region beyond 25°. In both cases the trend of the amplitude ratio is only little dependent on the distance. Beside the discrimination of velocity contrasts the amplitude ratios are sorted by its density increase, i. e. the greatest contrast of -10%-30%+30% yields lowest amplitudes with a ratio of about 0.2 (20% of the smooth amplitude) at 40° and 55 km. A density increase of +10% leads to largest amplitudes respect to the -10% and -30% velocity lowering. Similar effects can be seen for -5% V_P and -15% V_S.

Another interesting feature of synthetic calculations becomes visible if the absolute P-wave velocity and density contrasts equal. The models -10%-30%+10% (light green line) and -5%-15%+5% (dark green line) generate PcP amplitudes which show only few dependency on distance over the full considered range. Amplitude ratios for the -5%-15%+5% model are larger than for -10%-30%+10%. The impedances remain unaffected respect to the smooth values. Therefore the PcP amplitude is increasing with distance similarly to the smooth signal is rising. As well, this feature is visible for all considered ULVZ thicknesses. Though for the largest anomaly thicknesses of 55 km and 70 km the -10%-30%+10% pulse reduces at about 20% between 22° and 40°. Generally, amplitude differences of 55 km and 70 km are negligible and indistinguishable. It should be mentioned that indications for strong density effects independent from the velocity contrasts have been previously discussed by **?**.

The meaningful effect on the waveforms is discussed in section 3.4. Furthermore, the influences of the density and velocity contrasts at differing distance ranges can be seen on the spectral components of the synthetic seismograms which is noted in section 3.7.

Using synthetic seismograms significant effects on PcP amplitude ratios can be created. However, taking the resolution of observable waveforms into account one has to keep these diagrams in perspective. In general, a clear anomaly of PcP cannot be observed for a ULVZ thickness of

5.5 km or below. The variations are too close to the smooth ratio of 1.0. A maximum deviation of -10% is obtained for the greatest model contrast. Solely the curious amplitude increase in the very steep-angle range could be probably detectable. Even for larger thicknesses a clear separation between the single ULVZ models seems not possible. For instance, at about 16° and 18° there are 4 models with completely different contrasts which can explain the amplitude ratio of about 0.4 at 55 km. The models -10%-30%+30%, -5%-15%+30%, -10%-30%+15% and -5%-15%+15% generate such PcP amplitudes, i.e. many extreme velocity and density variations can cause such an amplitude depression. Moreover, the amplitude relations for varying layer thicknesses are fairly similar. This means that regarding to the same distance as above the amplitudes cannot only be generated by four diverse models but also by different ULVZ thicknesses, e.g. 27 km and 55 km. Therefore, considering only a PcP scaling it is not possible to make a decision about the character of the CMB.

The scaling of PcP by P is shown in figure 3.5 for all calculated models as well as the smooth model ak135. The kinks around 16° and 22° result from the upper mantle triplications at 410 km and 660 km, respectively, where P has higher amplitudes due to the caustics. Within that triplication range the P amplitude was measured from the whole wave train since it is difficult to separate the direct from the scattered waves in real data. In general, amplitude reductions become larger with increasing anomaly thickness. As well as for the PcP ratio diagrams a strong influence of the largest density contrasts is notable within the steep-angle region between 10° and 14° for all ULVZ thicknesses, although it is unlikely to observe this in the data. For distances between 25° and 40° the ratios for the seven velocity contrasts show unequal slopes, as in case for the PcP relation. Reductions of 10% for the P-velocity and 30% for the S-velocity are almost distance independent (unfilled arrows) in that range compared to the -5%-15% contrasts (filled arrows). A small amplitude increase with distance can be observed. This accounts for the predominantly influence of the velocity contrasts for larger distances. Again, the velocity variances are sorted by their density contrasts. A distance independent effect for configurations where $\delta|V_P|$ equals $\delta|\rho|$ can not be observed for the PcP/P scaling.
However, it should be noted that it is nearly impossible to distinct these various ULVZ models from the global standard model within the steep-angle region. This is another limit for the resolution of a low-velocity basal layer using the PcP/P relation. For distances beyond 25° any evidence for a specific anomaly are restricted. It might be possible to decide between the models -5%-15%+5% (dark green line) and -10%-30%+30% (black line) but within that model space a clear decision from the other models is improbable. Several ULVZ configurations can produce such amplitude ratios because the amplitude ratio differences between each model are less than 2%. For distances up to 25° the use of the $\mathrm{PcP}^{mod}/\mathrm{PcP}^{smooth}$ scaling augurs a better finding. Moreover, the significance of one model will be also influenced by the standard deviation of the measured data and its signal to noise ratio.

On the other side the obtained results for the gradient case also allow for an alternative or additional conclusion. It seems to be possible to have a thin (mushy) anomaly at the CMB, even with large velocity and density contrasts, without the ability for a clear seismic detection. The deviation from the global model is too small at a layer thickness of 5.5 km with a maximum PcP reduction of 10% respect to the smooth PcP. The PcP/P scaling reveals no amplitude decreases

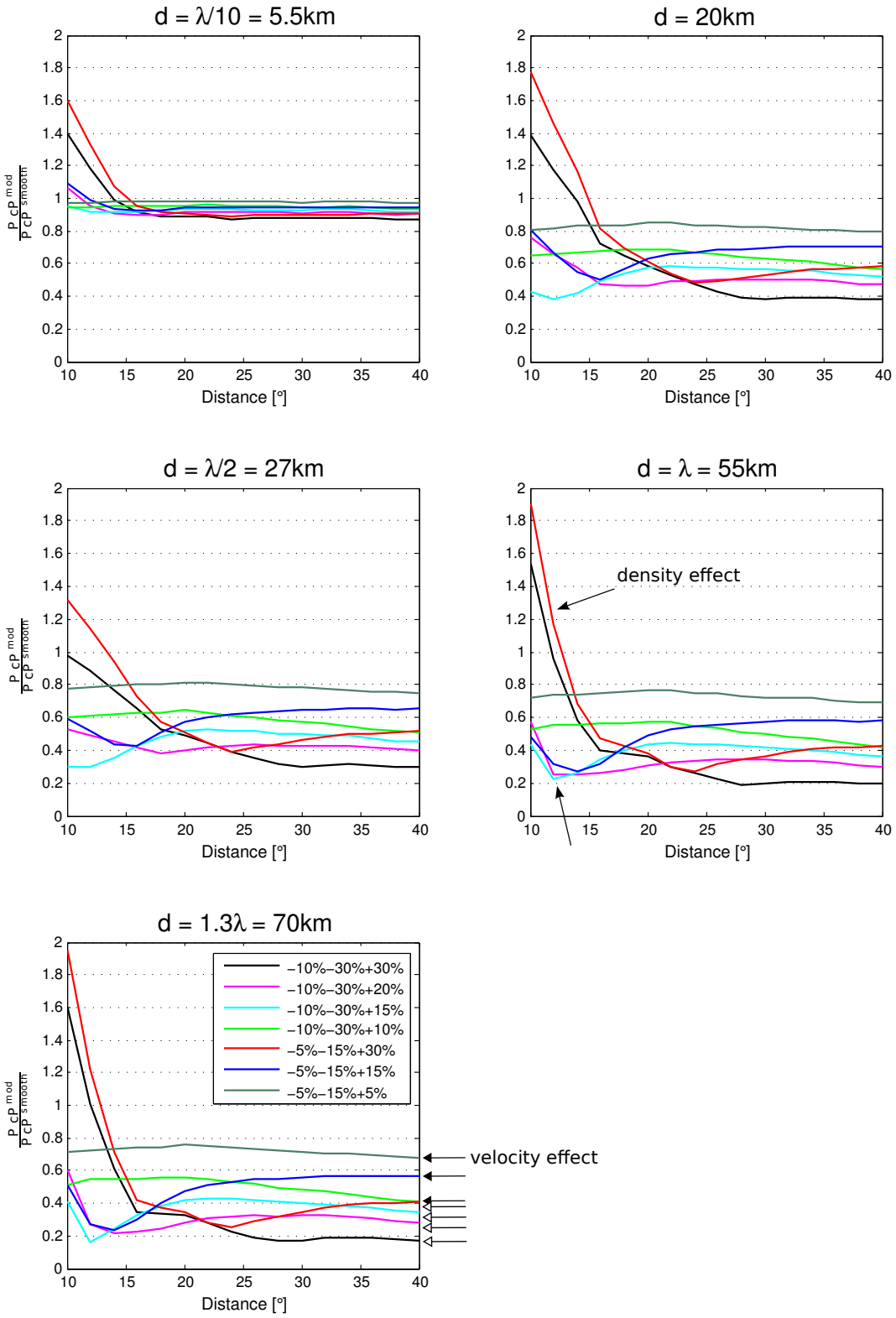

Fig. 3.4: PcP amplitude ratios of synthetic seismograms for **gradient** ULVZs. The core-mantle reflections of the modified global models are normalised by PcP of the smooth model. This figure shows the amplitude behaviour for seven models at five different ULVZ thicknesses within the distance range of 10° to 40°. The parameter λ reflects a wavelength of about 55 km at the CMB according to a dominant source period of 4 s. The annotation of the legend refers to a relative reduction of P- and S-wave velocity and an increase of the density, respectively. A primary density effect can be seen within the steep-angle region up to 20°. For the wide-angle region the velocity contrasts, which are sorted by the density, dominate the amplitude ratios. The filled (unfilled) arrows correspond to a velocity reduction of -5% (-10%) V_P and -15% (-30%) V_S. Strong distance dependencies occur except for -10%-30%+10% (light green line) and -5%-15%+5% (dark green line).

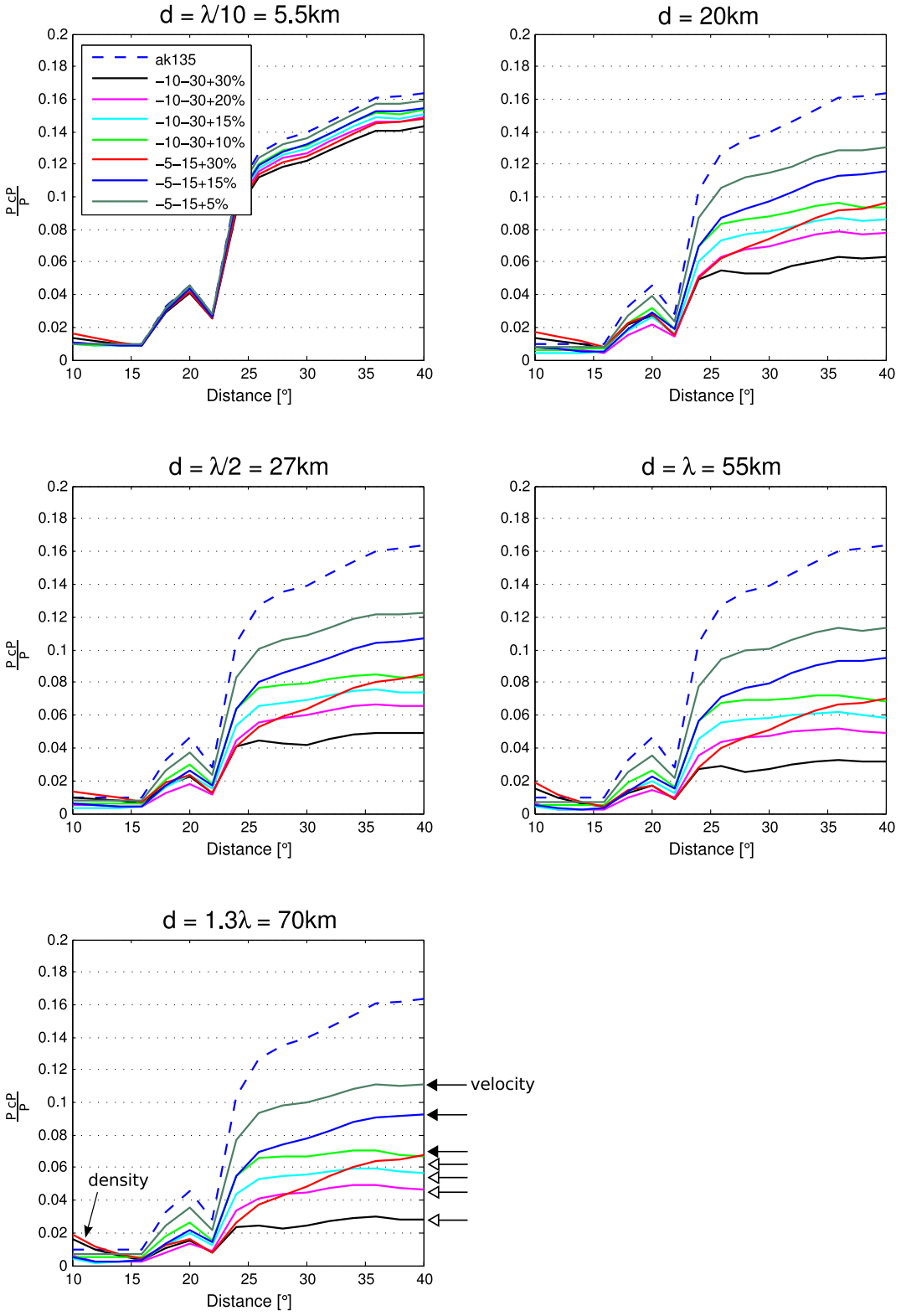

Fig. 3.5: The ratio of PcP to P is shown for the **gradient** layered case. The kinks at 16° and 22° result from the triplications at 410 km and 660 km, respectively, where P has higher amplitudes. Notation as in figure 3.4. Density and velocity effects for near and far distances can be seen, respectively.

up to 25° and only -0.02 (about 10%) beyond that distance. From this point of view, this would not be a true, common ULVZ but rather a core-mantle transition zone (CMTZ) in contrast to a discrete boundary. Previous studies, e. g. by Vidale and Benz [1992] and Garnero and Jeanloz [2000], have suggested such an additional CMB feature with a transition thickness up to 3 km. However, they assume that the CMTZ will also affect the uppermost layer of the outer core. The CMTZ in this study refers only to the mantle-side modellings. It is shown in the next section that such a thin gradient layer atop the CMB can be separated from a first-order discontinuity which may refers to a 'real' ULVZ.

Summary

- The amplitudes vary as function of the distance and the impedance contrasts.
- Primary density effect occurs in the steep-angle range (up to 20°) and a pronounced velocity dependency in the wide-angle region.
- The distance dependency in the wide-angle region becomes little independent from the model contrasts.
- The amplitude ratios decrease with increasing anomaly thickness.
- Better model constraints are possible using PcP/P and $\mathrm{PcP}^{mod}/\mathrm{PcP}^{smooth}$ scalings.
- Thin layers below 5.5 km may rather refer to a core-mantle transition zone (CMTZ) than to a usual, discontinuous ULVZ.

3.2 Modelling with Discontinuities

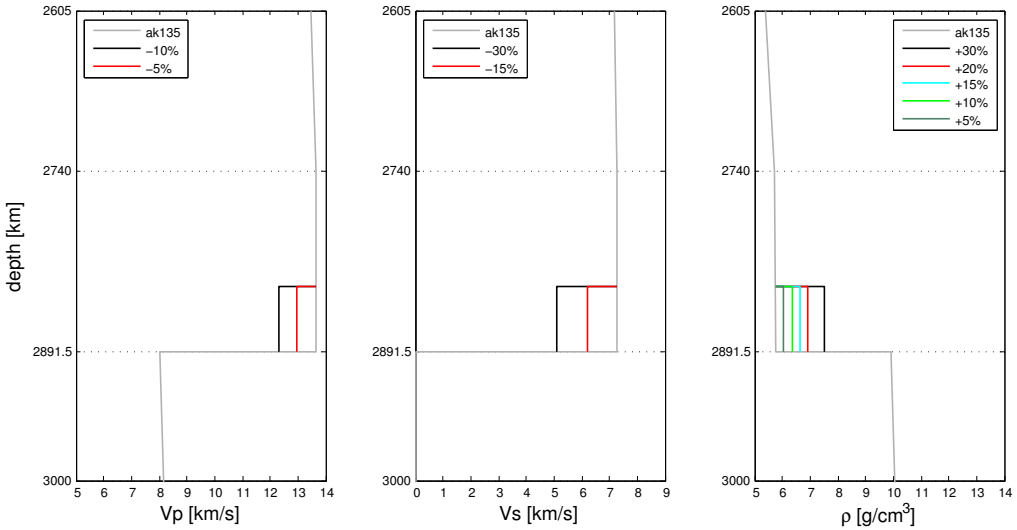

Fig. 3.6: Velocity-depth models for first-order discontinuity atop the ULVZ with a thickness of 55 km. Only the velocity contrast ratios of 1:3 are shown here. The density-depth function is also illustrated.

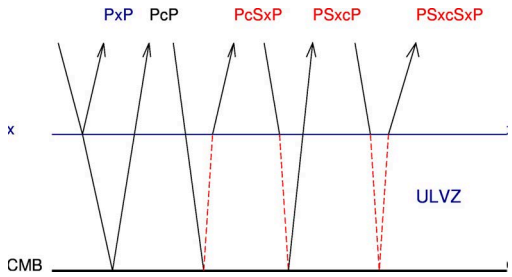

Fig. 3.7: Schematic illustration of rays created at the discontinuity x and their nomenclature. PxP is the precursor to the core-reflected PcP. Three postcursors exist, of which PcSxP and PSxcP superimpose on seismograms to one strong amplitude since they are kinematically equivalent and arrive at the same time. PSxcSxP is the second postcursor phase that arrives after the first one because of its two SV-wave legs. The amplitude of this phase is always smaller than that of the first postcursor.

In the next step first order discontinuities were included atop the low velocity layers illustrated in the figure above. The same thicknesses and model configurations have been used as for the gradient ULVZs. In addition, the calculations were repeated for P-wave to S-wave velocity reductions of the relation 1:2. When first order discontinuities are modelled, an additional waveform is generated due to the topside reflection at the basal layer boundary which is denoted as x. This is a precursor to the mother wave PcP and is called PxP below. The phase nomenclature is shown in figure 3.7 and also illustrated at d = 70 km in figure 3.16. Due to the coupling of compressional and shear waves a conversion from P to SV is produced during the transmission at discontinuity x and the reflection at the CMB. The first postcursors PcSxP and PSxcP are slower than PcP because of their SV-wave legs and they are kinematically equivalent. Hence, both phases arrive at the same time after PcP and superimpose on seismograms. Since their reflection coefficients are positive a strong postcursor appears. The second postcursor PSxcSxP is even later than the first one due to two SV-wave legs and it arrives after PcSxP and PSxcP. Its amplitude is also always positive but much weaker than the first postcursor. However, the exact amplitudes depend on the ULVZ configuration. The development of those pre- and postcursors depends on the thickness of the ULVZ. The thicker a basal layer is, the more are pre- and postcursor separated respectively to PcP.

3.2.1 Calculation with $\delta|V_P| : \delta|V_S| = 1 : 3$

As can be seen in figure 3.8 the results of discontinuity modelling are similar to gradient low-velocity basal layers. Note that the vertical axis of $\mathrm{PcP}^{mod}/\mathrm{PcP}^{smooth}$ is slightly larger than in figure 3.4 but all significant features described above occur as well. In the very steep-angle region the strong distance dependent amplitude ratios, dominated by the density contrasts, can be seen. For increasing distance the amplitudes are influenced by the velocity variances (cf. filled and unfilled arrows in figure 3.8). In case the absolute density variance equals the P-wave velocity contrast no distance dependency is obtained.
However, there are two characteristics which are in contrast to gradient ULVZs. At a layer thickness of 5.5 km the seven models can be more distinguished. The -5%-15%+5% model reveals amplitude reduction by about 10% over the full distance range where the largest model contrast produces a ratio of 0.6 beyond 30°. Moreover, the strange PcP amplifications for very steep incidence angles are much more pronounced. The core-reflected phase completely interfere here with its precursor which may influence this attribute. On the other side, for all larger thicknesses

the amplitude ratios remain almost constant, i. e. they do not decrease with increasing basal layers. This is consistent with the outcomes of the PcP/P scalings shown in figure 3.9. These relations yield similar amplitude trends as illustrated in figure 3.5 with constant PcP amplitudes for increasing anomalies. As distinguished from that only the thinnest modelled layer augurs a better separation of the single models with reductions up to 40% beyond 25°.
Hence, a conclusion about the ULVZ thickness, only by this relation, is not possible in case of discontinuities unless the layer is very thin: If no precursor is observable but the PcP amplitude reduction amounts to more than 10%, a very thin ULVZ with a first-order discontinuity may exist. Otherwise, if amplitude reductions of less than 10% are obtained this could indicate either a moderate, thin ULVZ or a mushy mantle-side CMTZ (with completely different velocity and density configurations) as mentioned in the previous section.
In summary, considering only the PcP/P and PcP^{mod}/PcP^{smooth} ratios, first and second order discontinuities are indistinguishable without additional information. Therefore the precursor can provide the chance of a better model space limitation.

Figure 3.10 illustrates the ratio of the precursor PxP to PcP. An ULVZ of 5.5 km is not shown here. In this case PxP is not visible in synthetics because of its strong interference with PcP. It is important to note that PxP has mostly much larger amplitudes than the core-reflected wave, however not always over the whole distance range. Within the steep-angle region PxP is always larger than PcP except for -10%-30%+10% and -5%-15%+5%. Those models with identical absolute P-velocity and density contrasts have always greater PcP phases.
Again, the steep-angle area indicates a primary density effect since models -10%-30%+30% and -5%-15%+30% as well as -10%-30%+20%, -10%-30%+15% and -5%-15%+15% have similar PxP/PcP values in that range. Beyond their peak amplitude ratios the density dependency diminish. That peaks correlate with the polarity reversals of PcP, respectively and are in agreement with the previous shown PcP^{mod}/PcP^{smooth} diagrams. See section 3.4 for more details. For the configurations of -5%-15%+15%, -5%-15%+30% and -10%-30%+15% the ratio changes to values less than one at wide-angle distances and PcP exceeds PxP (marked by shaded area). There is no correlation with their impedances. The models -10%-30%+30% and -10%-30%+20%, i.e. greatest density contrasts for highest velocity variances, reveal larger PxP amplitudes over all distances (cf. section 3.8). These relations remain constant for all ULVZ thicknesses. According to the resolution of real data, if PxP is smaller than PcP a discrimination beyond 30° will be not reliable.

3.2.2 Calculation with $\delta|V_P| : \delta|V_S| = 1 : 2$

Since the reflection coefficient of an incident P-wave is also dependent on the shear wave properties [Müller, 1985]; section 2.1, an influence on PcP is expected when reducing the velocity contrast ratio. Shear waves are more affected by mushy regions than compressional waves but the magnitude of that lowering is ambiguous [Williams and Garnero, 1996; Mao et al., 2006, 2011; Jacobsen et al., 2002]. Therefore the velocity contrast ratio has been reduced from 1:3 to 1:2. In figure 3.11 the results for a ULVZ layer of 55 km are shown to test that influence, where same effects occur as before. Considering all model contrasts, the common difference to the higher velocity ratio is an increase of the PcP amplitude (cf. figure 3.8). For instance, model -5%-10%+5% generates about 20% higher amplitudes and model -10%-20%+30% about 30% higher amplitudes beyond 30°. However, the amplitude increases within the very steep-angle

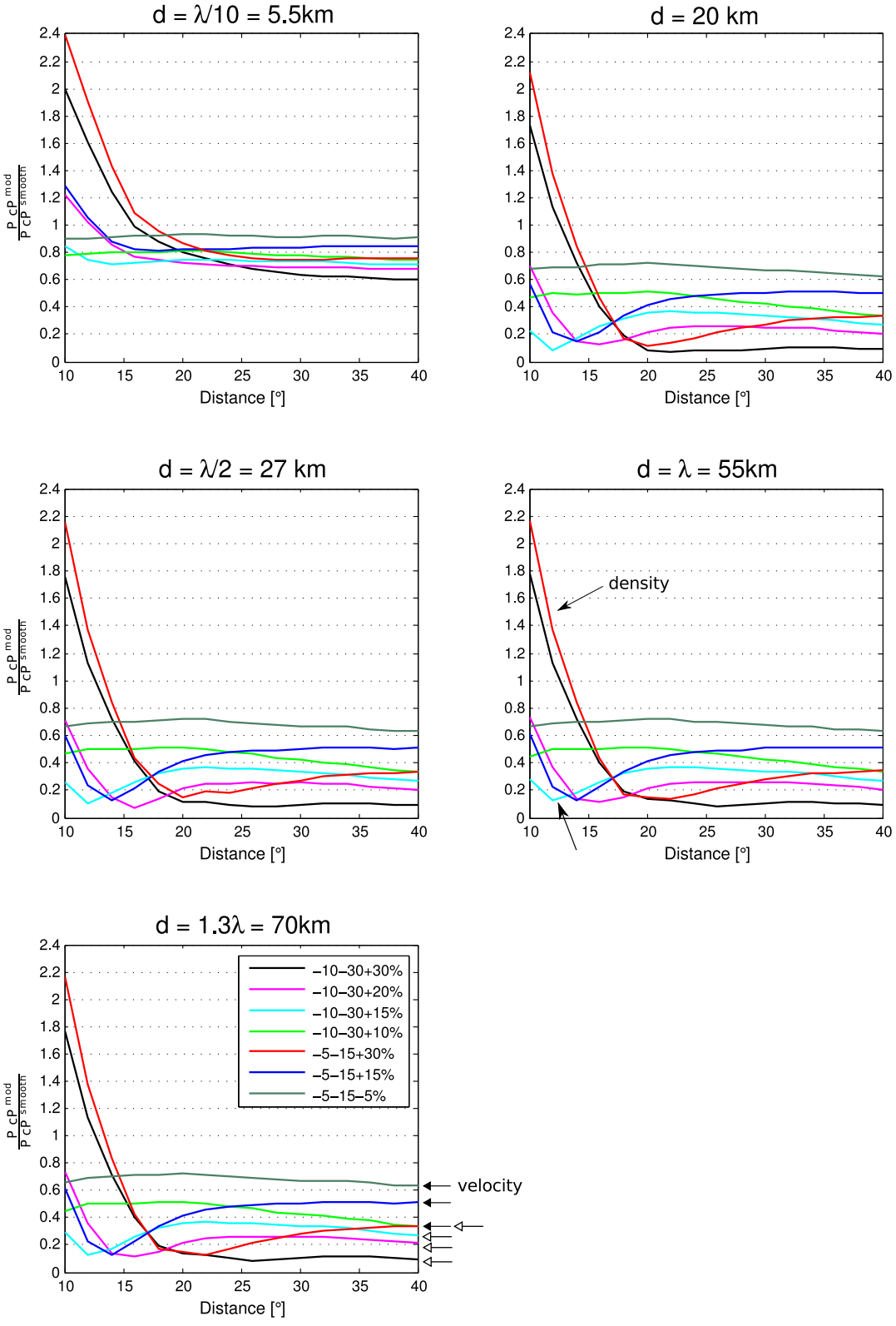

Fig. 3.8: PcP amplitude ratios of synthetic seismograms with a **discontinuity** above the ULVZ. Notation as in figure 3.4. Note that the vertical scale is larger than in figure 3.4. The models can be better separated for a thickness of 5.5 km respect to the gradient ULVZ. Otherwise, amplitudes do not decrease with increasing layer thickness. Same distance dependent effects occur as for the second order discontinuities. The filled (unfilled) arrows correspond to a velocity reduction of -5% (-10%) V_P and -15% (-30%) V_S.

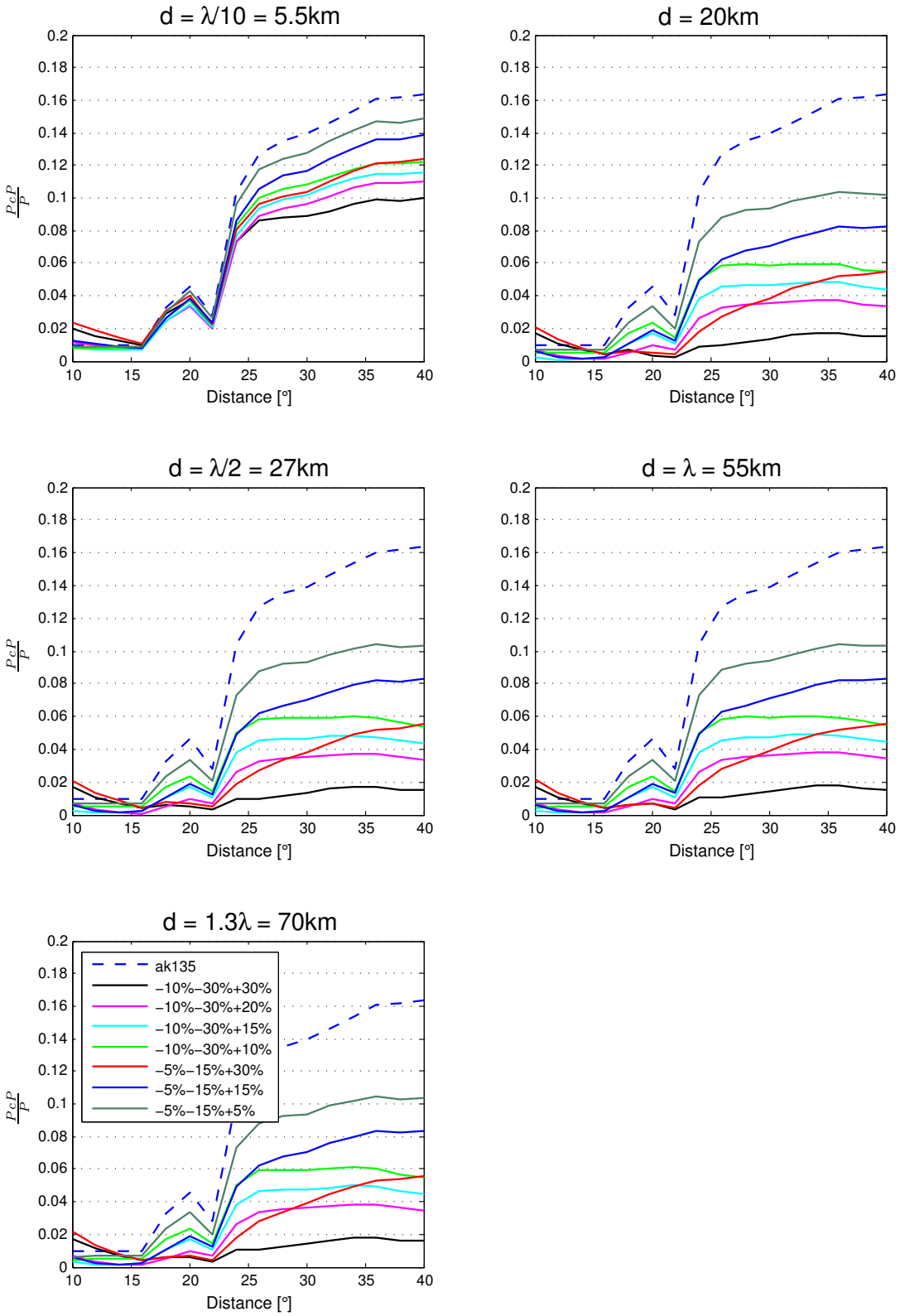

Fig. 3.9: PcP/P amplitude ratios of synthetic seismograms with a **discontinuity** above the ULVZ. Notation as in figure 3.4. The models can be better separated for a thickness of 5.5 km respect to the gradient ULVZ. Otherwise, amplitudes do not decrease with increasing layer thickness.

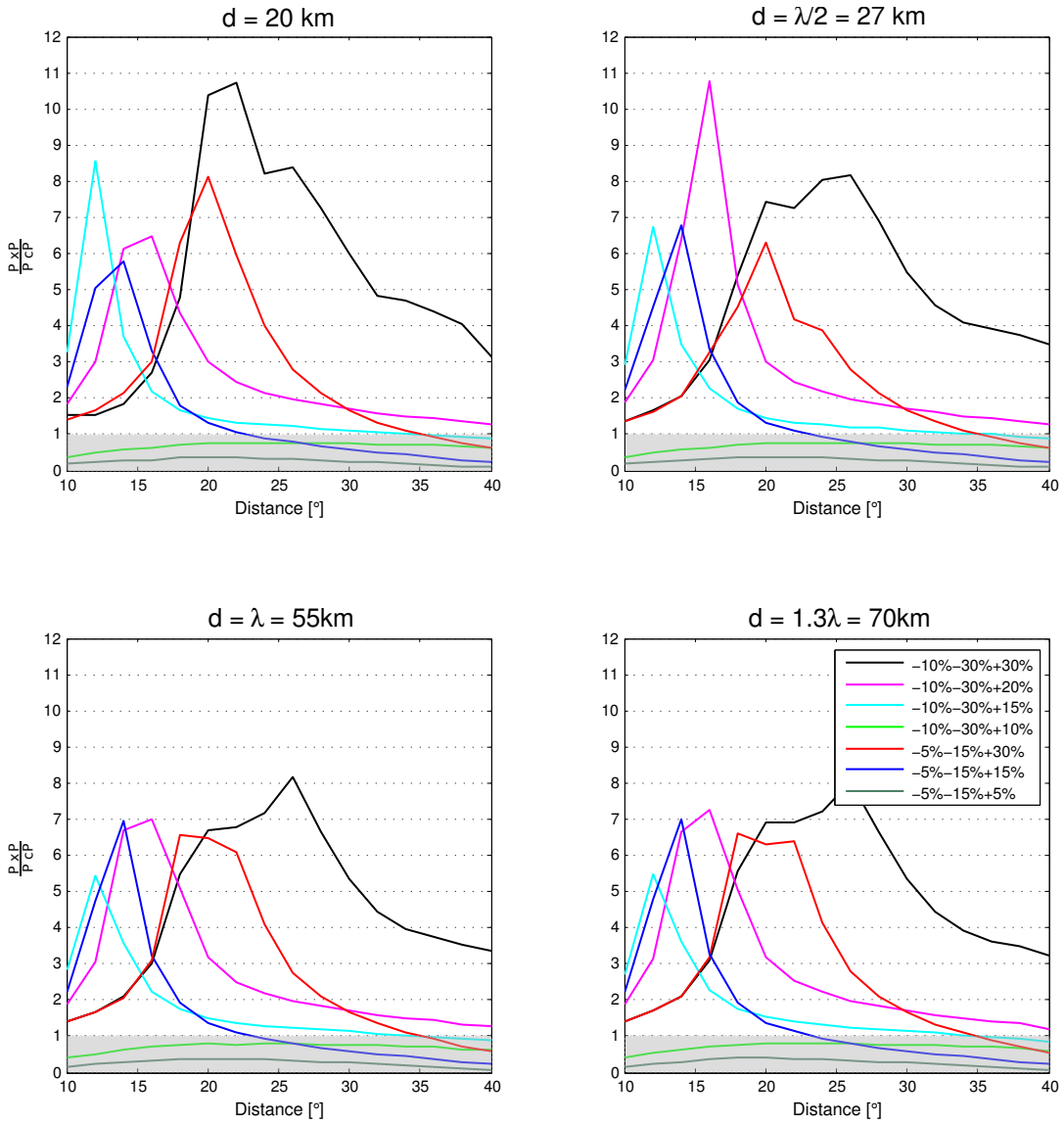

Fig. 3.10: The relation of precursor PxP to PcP is shown for four different anomaly thicknesses. In case of an ULVZ layer of 5.5 km the precursor can not be separated in synthetics because of its interference with PcP. Grey highlighted areas mark where the core reflected phase is larger than PxP. The peak amplitude ratios coincide with the predicted PcP polarity reversal.

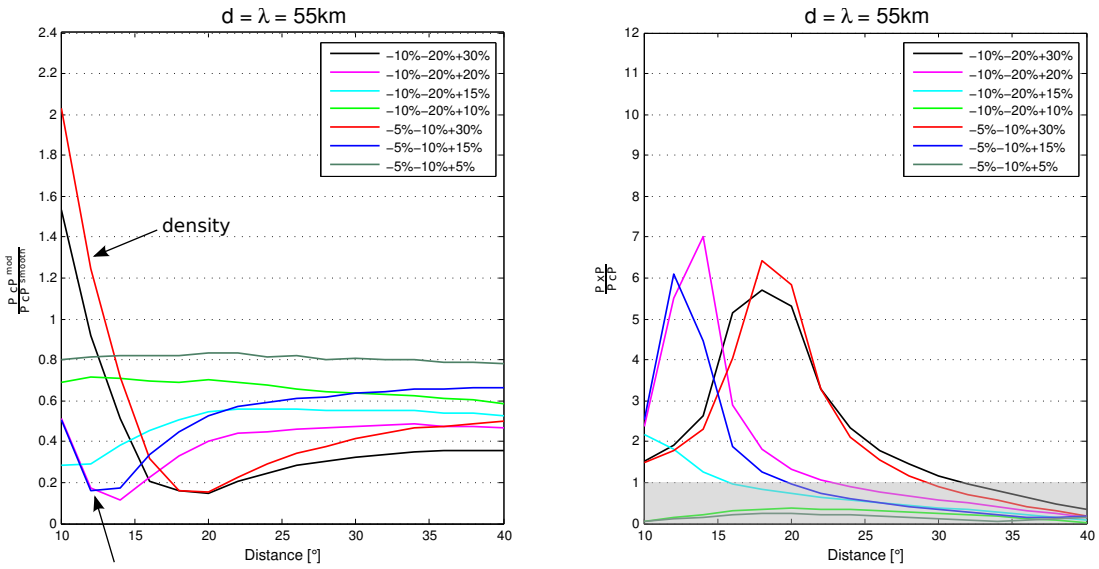

Fig. 3.11: The velocity contrast ratio of P- and S-waves has been reduced to 1:2. In general PcP amplitude ratio is increased for relatively higher shear wave velocities respect to the modelling with larger velocity contrast ratio. For further distances the precursor PxP is always smaller than PcP for all configurations.

region is slightly reduced respect to the 1:3 ratio.
The influence on the precursor related to PcP is more pronounced. PxP is little lowered compared to PcP in figure 3.10 for all configurations. The trend of PxP over PcP equals for -5%-10%+30% and -10%-20%+30% as well as for -10%-20%+20% and -5%-10%+15% over the full distance range, i.e. the amplitudes with identical or similar density coincide. This is in contrast to the 1:3 ratio where these amplitude ratios are not similar beyond the ratio peak. Hence, the S-wave velocity should cause this difference. See section 3.4 for more details. The core-reflected impulse becomes larger than PxP in wide-angle regions for all models, which is also in opposition to the higher velocity ratio.

Summary

- The amplitudes vary as function of the distance and the impedance contrasts.
- Primary density effect occurs in the steep-angle range (up to 20°) and a pronounced velocity dependency in the wide-angle region.
- The amplitude ratios do not decrease with increasing anomaly thickness (>20 km).
- If no precursor is observable but the $\mathrm{PcP}^{model}/\mathrm{PcP}^{smooth}$ amplitude reduction amounts to more than 10%, a very thin ULVZ of 5 km with a first-order discontinuity may exist.
- If amplitude reductions of less than 10% are obtained, this could indicate either a moderate, thin ULVZ or a gradient CMTZ (with completely different velocity and density configurations).
- PxP is mostly larger than PcP in the steep-angle range expect for $\delta|V_P| = \delta|\rho|$

3.3 Elastic and Attenuating Earth

So far synthetic seismograms were calculated without damping. In this section the influence of an attenuating global model on the amplitude ratios were appraised for the gradational behaviour atop the ULVZ as well as for a discontinuity. Using the global attenuation parameters of ak135 [Kennett et al., 1995] only little differences on the amplitude ratios can be observed. This is valid for all ULVZ thicknesses. At first, within the ultra-low velocity layers same quality factors as at the CMB were applied. Figure 3.12 shows the results only for an anomaly thickness of 55 km. An attenuated PcP/P scaling and PcP ratio (dashed lines) in comparison with the elastic calculations (solid lines) are given in the upper diagrams of figure 3.12 for gradients atop the ULVZ. As can be seen the disparity is marginal for all used models in both cases. This means that the direct P-wave and the core-reflected signal are absorbed in equal measure above all for distances up to 25°. Same results were obtained by measurements for a discontinuity, illustrated in the lower left picture.
On the lower right diagram the relation of the precursor PxP to PcP is shown for elastic (solid lines) and anelastic models (dashed lines). Again, most of these models show no significant discrepancy between the purely elastic and attenuated solution. Solely the -10%-30%+30% and -5%-15%+30% model contrasts, i. e. the models with the highest density variance, have larger deviations between 18° and 28° and 16° and 24°, respectively. Those distance ranges coincide with the polarity reversal of PcP for these models which is always subject to amplitude variabilities. Therefore, the variances here result rather from impreciseness of amplitude measurements than from true effects. Polarity reversals within the very steep-angle region generate less fluctuations. Thus, this comparison demonstrates that the use of a fully elastic earth as input model for synthetic seismograms is allowed and does not distort the results as long as PcP ratios and PcP/P scaling were considered. For the precursor ratios this assumptions is restricted. Section 3.8 will show that the rate of PxP to PcP is in general subject to larger fluctuations when using alternative calculations, i.e. the Gauss beam method. Finally, the available damping parameters are just rough approximations about the earth's media and it is shown here that varying attenuation should not have a primary effect on the amplitude ratios.

In order to reinforce this assumption for short-period signals the quality factor for the P-wave inside the ULVZ has been changed. The quality factor for P is about 720 at the CMB according to the global model. This value has been reduced by 500 to about 220 within a 55 km thick anomaly zone. The discontinuity model with -10%-30%+30% and a source period of 1 s were applied to test that influence for 'broad-band' synthetics (sampling rate of 10 Hz) as well as using a short-period band-pass filter of 0.5-1.5 Hz. Figure 3.13 illustrates the results in comparison to the conventional anelastic earth model (solid lines) as illustrated above. Only marginal variance beyond 35° is identifiable for the 'broad-band' and filtered synthetic PcP waves. In the steep-angle area no difference can be observed. This result is in contrast to the modelling by Schlittenhardt [1984]. He studied the damping effects for the D″ region of 190 km thickness at a distance range of 70° to about 85°. In this case the PcP signal passes much longer through a zone of extreme absorption. For example, at an incidence angle of 75° PcP is traveling about 1500 km through D″ instead of a propagation path of 135 km for an incidence angle of 35° and the ULVZ parameters shown here. As a result Schlittenhardt [1984] obtained a PcP/P reduction of about 40% using a similar P-quality factor of 250. Hence, within the distance range and layer thicknesses presented in this study damping effects are negligible.

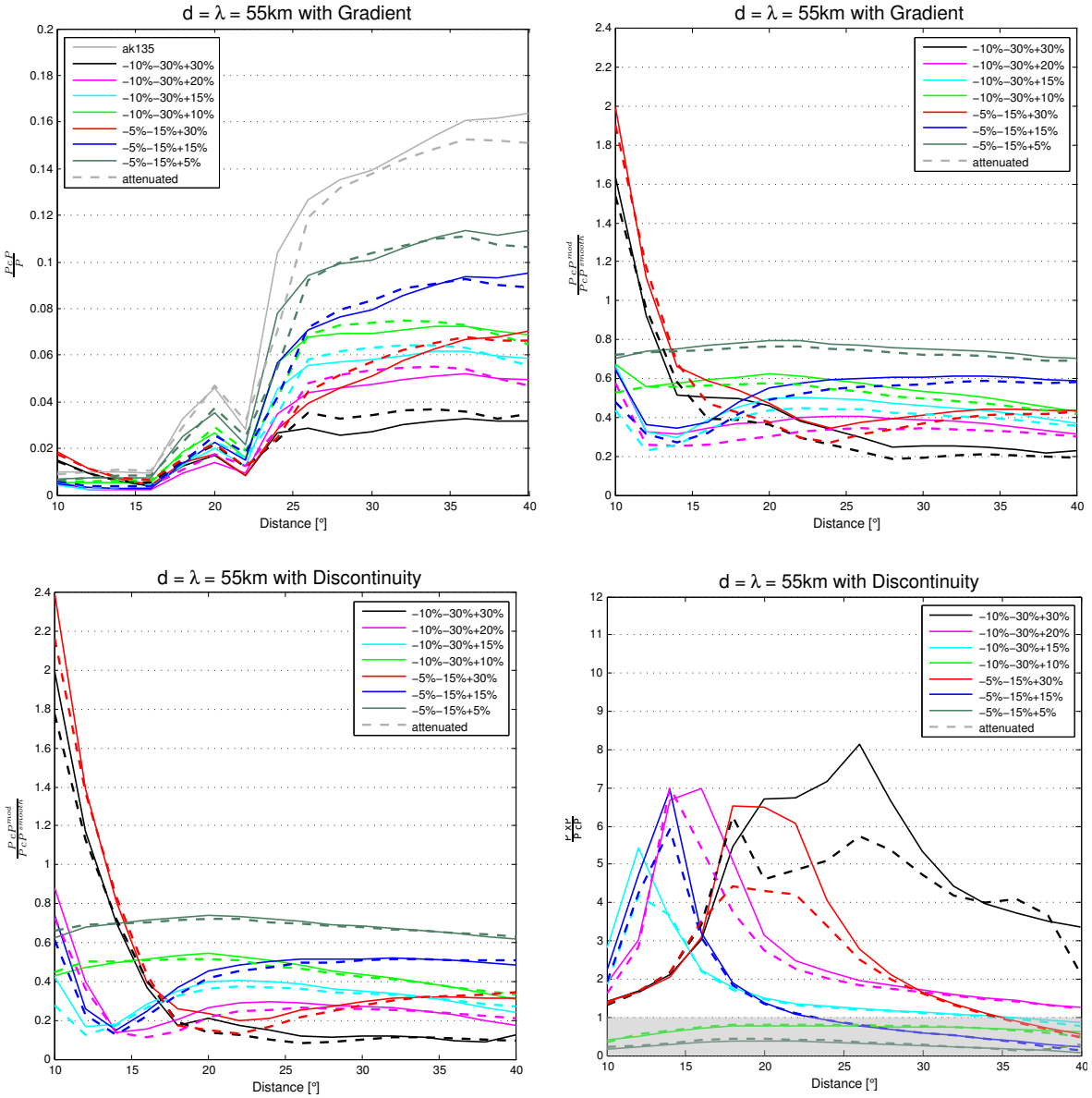

Fig. 3.12: Top: PcP/P scaling and PcP amplitude ratio for **gradient** ULVZ with a source period of 4 s in comparison with attenuating models (dashed lines). Compared to the fully elastic earth (solid lines) no decisive differences can be observed. **Bottom**: Same as above but for the **discontinuity** case. The ratio of the precursor PxP to PcP is also shown. Most of the models show no significant discrepancy between elastic and attenuated earth. Only the -10%-30%+30% and -5%-15%+30% models indicate larger deviations between 18° and 28° and 16° and 24°, respectively. This distance ranges corresponds to the appropriate polarity reversals of PcP.

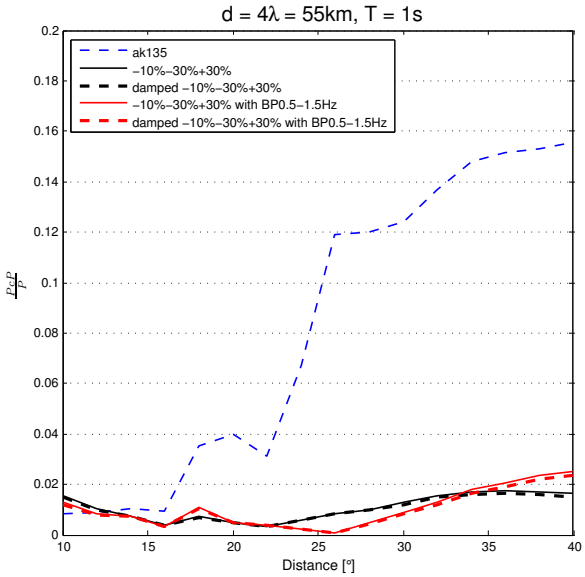

Fig. 3.13: PcP/P amplitude ratio for an exceedingly damped ULVZ of 55 km thickness. The discontinuity model with -10%-30%+30% and a source period of 1 s were used to test that influence for 'broad-band' synthetics as well as using a short-period band-pass filter of 0.5-1.5 Hz. The solid lines and the ak135 model refer to an attenuated earth. No significant deviations of PcP can be recognised and no frequency dependent effects are visible. Also for this high-frequency wavelet the deviation to the elastic case is negligible.

3.4 Analysis of Waveforms and Reflection Coefficients

In the first part of this thesis only the manifold amplitude features of PcP were considered. In this section the attributes of waveforms are presented and discussed in relation to the reflection coefficients. Figure 3.14 shows the displacement proportional, anelastic results for model -10%-30%+30% and all layer thicknesses. Note that a velocity reduction of 12.2 km/s was used as well as a time reduction of 20 s. The grey traces illustrate the smooth PcP impulses in which at 10° the dominant period is still about 4 seconds. With increasing distance the smooth pulse becomes broader and at 40° the base of PcP shows a width of about 7 seconds. At a thickness of 5.5 km, which is one-tenth of the wavelength, a waveform distortion for the closer distances up to 24° can be observed. The first peak is shifted about +2 seconds whereas a small negative peak coincide with the smooth PcP peak. This small negative polarity changes to positive values with increasing distance. The whole modified pulse is broader even for the closest distances and little larger at 10° to 14°. At wide-angle regions the pulse shape equals the smooth wave although it is slightly reduced. These effects are quite small for the thinnest layer and become more pronounced for larger thicknesses. An ULVZ layer of 20 km shows still the same waveform trend as a layer of 5.5 km thickness. However, when the thickness further increases to the half wavelength of 27 km the wave begins to deform also for larger distances beyond 30° (compare blue ellipses). The generation of a small notch initiates at this thickness and the impulse base becomes broader. These characteristics are more notable for ground velocities displayed in figure 3.15.

An anomaly thickness that match one wavelength of 55 km shows remarkable waveform distortions over the full distance range. The change of the polarity is now very clear where the reversal occurs at about 27°. Between 10° to 14° the maximum amplitudes are negative and definitely

greater than the smooth wave as has been discussed for the amplitude ratio diagrams. For distances beyond 30° the impulses are extremely broadened at the base up to 17 seconds at 40° with a strong notch that coincides with the smooth peak of dominant period of 4 s. At the greatest modelled thickness of 70 km the behaviour of PcP meets the 55 km results, except for the even broader impulse bases. Again, the produced cusp correlates to the simple smooth shape. Travel time deviations can not be observed.
As noted above, the beginning of waveform distortion at d = $\lambda/2$ is more pronounced for derived ground velocities in figure 3.15. As can be seen the PcP signal gets split into a precursor and postcursor with rising layer thickness although only second order discontinuities are considered. This is an analogue effect to the upper mantle triplications for P. There, also only gradients were used for the calculations but strong focussing and defocussing effects occur follow from complex P waves because of the large velocity gradient. The small second order pre- and postcursors become better separated from PcP with increasing thickness. Hence, these varying travel time differences enables a conclusion about the ULVZ thickness. Polarity reversals are well pronounced even for 5.5 km. Note that between 200 and 300 seconds larger numerical but steady noise appears since the derivation of signals leads to a higher frequency content of the seismograms.
Ground velocity proportional waveforms in case of first order discontinuities atop the ULVZ are presented in figure 3.16. Regarding the amplitude ratio diagrams, same waveform features as mentioned above should be cognisable. For the thinnest model layer of 5.5 km the effects are small but an amplitude increase between 10° and 14° is nevertheless obtained. The PcP pulse reveals a larger negative peak and the change of the polarity is denoted. Beyond 24° the amplitude lowering becomes prominent but the impulse shows a simple symmetric two-sided shape. Already for a layer thickness of 20 km the scattering of PcP is notable, where the wave train is rather dominated by the pre- and postcursor than by the true core-reflected phase. The negative PcP amplitudes for distances up to 26° cause an enlarged dominant PxP phase due to the interference. With increasing layer thickness the PcP waveform and their polarity reversal are even more clearly since the traveltime difference between pre- and postcursor increase. As has been shown in figure 3.10 PxP is always much larger than PcP.
From the amplitude ratio diagrams a strong density dependency on near distances has been shown. This feature is also reflected in the pulse shapes. Figure 3.17 compares the waveforms of model -10%-30%+30% (black), -10%-30%+15% (blue) and -5%-15%+30% (red). Within the steep-angle range up to 18° PcP is distorted in equal measure for the models with highest density contrasts independent from their velocity configuration. Beyond 20° the three different waveforms become increasingly different also in terms of their polarity change.

The absolute reflection coefficients of PcP are shown in figure 3.18 as function of the incidence angles for all ULVZ models used. The incidence angles correlate to different epicentral distances since the conversion is related to the P velocity at the CMB (cf. section 2.1). At first, velocities with flattening had to be calculated by equation 2.23. A conversion according to the earth-flattening approximation [Müller, 1977] is necessary because Snell's law refers to horizontal interfaces but the global model includes spherical velocities. Then the flat velocities can be used to calculate exact horizontal slownesses for the appropriate incidence angles (cf. equation 2.18). Using the seismological table for ak135 the accurate distances are obtained. However, the discrepancy between V_P for -10% and -5% is marginal for distances up to 45°. Thus, incidence angles approximate the epicentral distances for the considered range. The smooth coefficient

is also shown, illustrated with the grey line, but the displayed distances do not fit the smooth values.

Firstly, consider the upper two diagrams with a δV_P to δV_S ratio of 1:3. All reflection coefficients are clearly reduced beyond 18° above all for the larger velocity contrasts of -10% and -30% for P and S, respectively. Within the steep-angle region up to 15° the coefficients and therewith the amplitudes are raised and negative for the models -10%-30%+30% and -5%-15%+30%. This is in good agreement with the seismograms and also with the amplitude ratio diagrams. Thus, an amplitude increase for the closest distances can be reproduced using reflection coefficients that are based on the calculation with two homogeneous half-spaces. The models with density increases of +15% and +20% have also larger and negative amplitudes, nonetheless outside the study range. An important feature gives rise to the density contrast. The higher the densities are, the larger are the amplitudes within the very steep-angle region. Thereby, for -5% V_P and -15% V_S the amplitude would be even higher than for -10% V_P and -30% V_S. An occurrence of a polarity reversal is also controlled by the density of the medium. The larger the density variance, the larger is the distance for the polarity change. For instance, the seismograms in figure 3.15 indicate a polarity change around 27° which is consistent with the half-space reflection coefficient of model -10%-30%+30%. In addition the greatest densities lead to lowest values beyond 25°. In conclusion, the highly varying amplitude ratios coincide with the theoretical half-space reflection coefficients. In case of $|\delta V_P| = |\delta\rho|$ no polarity reversals are created. The growing of the modified coefficient corresponds to the smooth one. Hence, the measured PcP amplitude ratio reveals a distance independent behaviour as can be seen in figures 3.4, 3.8 and 3.11.

The lower two diagrams of figure 3.18 show the half-space reflection calculations for the reduced V_P to V_S contrast ratio of 1:2. It is obvious that the polarity reversals are shifted to closer distances respect to the higher velocity ratio. In such a way model -10%-20%+30% has its polarity change already at 22°. However, the absolute coefficient remains constant for extremely steep incidence angles up to 15°. Consequently, it is independent from the shear velocities. For perpendicular incident rays no P-SV conversion occurs since the whole energy is transmitted. Thus, in case of those very steep incidence angles the influence of the shear wave properties is negligible. All amplitudes are larger beyond that reversal points which fits the synthetic results illustrated in figure 3.11. Hence, also the shear wave velocities have a crucial influence on the core-reflected phase for larger distances >20° even densities remain constant.

Concluding, it should be noted that half-space reflection coefficients are able to reproduce the amplitude behaviour for the PcP^{mod}/PcP^{smooth} relations but cannot provide information about the absolute amplitude ratios since the calculations are independent from an ULVZ thickness. Thus in terms of the data, a carefully analysis is required since amplitude ratios decrease for increasing anomaly thickness in case of gradient ULVZ.

Again, in comparison with the lower velocity ratio the difficulties to pin down a PcP anomaly can be seen. For instance, at a distance of 40° models -5%-15%+5% and -10%-20%+10% yield equal reflection coefficients of about 0.2, i.e. 20% of the P amplitude (cf. figure 3.18). Even in case of a first-order discontinuity a conclusion about a specific model is not possible since PxP is almost unchanged at that distance.

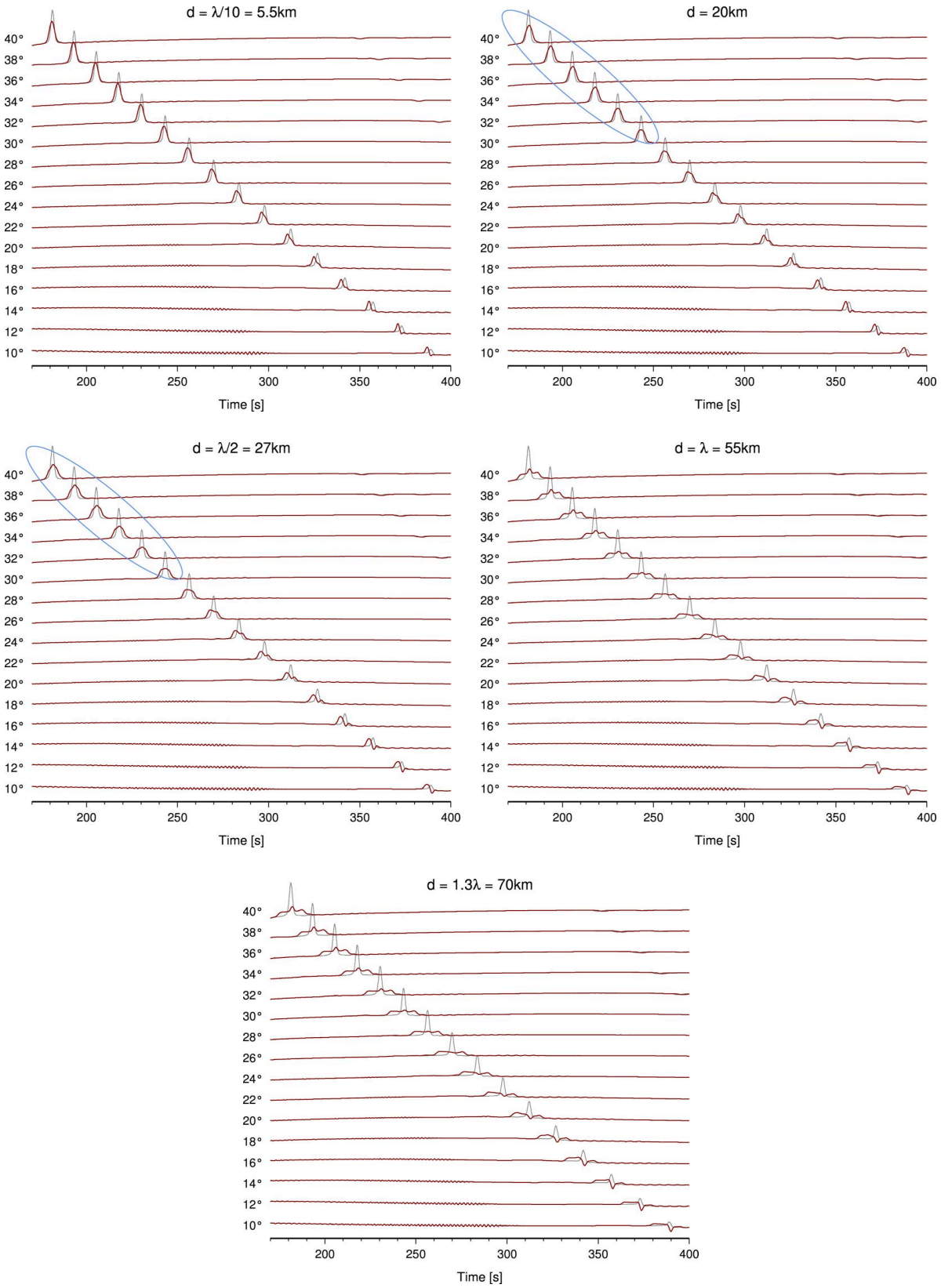

Fig. 3.14: Waveform analysis for model -10%-30%+30% and **gradient** ULVZ. **Ground displacements** are shown. Grey seismograms show the smooth results, whereas the red traces refer to the ULVZ model illustrated for the five different anomaly thicknesses. Note that the waveform begins to distort between 20 km and 27 km thickness for wide-angle distances imaged by the blue ellipses. A velocity reduction of 12.2 km/s was used as well as a time reduction of 20 s.

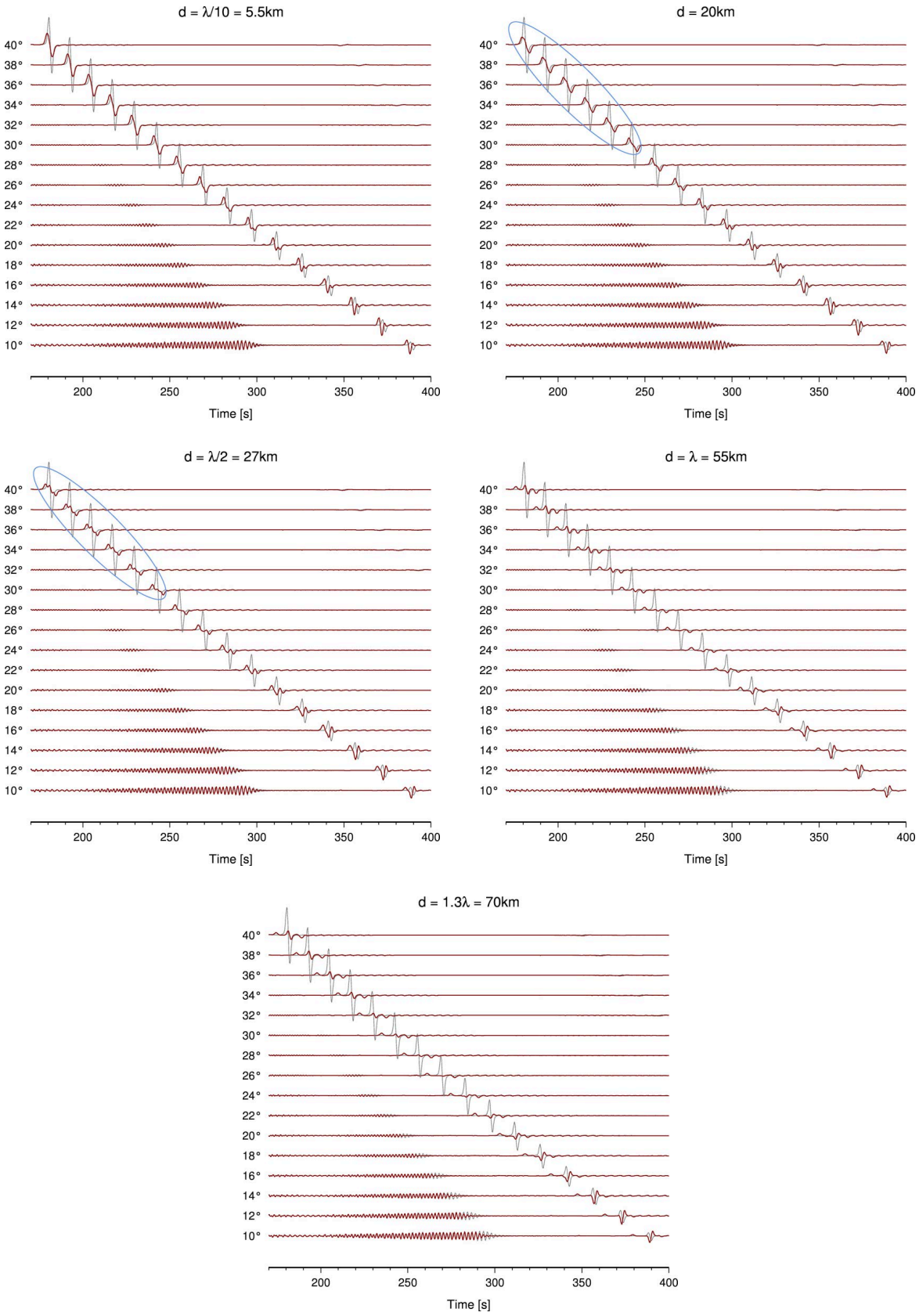

Fig. 3.15: Waveform analysis for model -10%-30%+30% and **gradient** ULVZ. **Ground velocities** are shown. Grey seismograms show the smooth results, whereas the red traces refer to the ULVZ model illustrated for the five different anomaly thicknesses. Note that the waveform begins to distort between 20 km and 27 km thickness for wide-angle distances beyond 30° (marked by the blue ellipses).

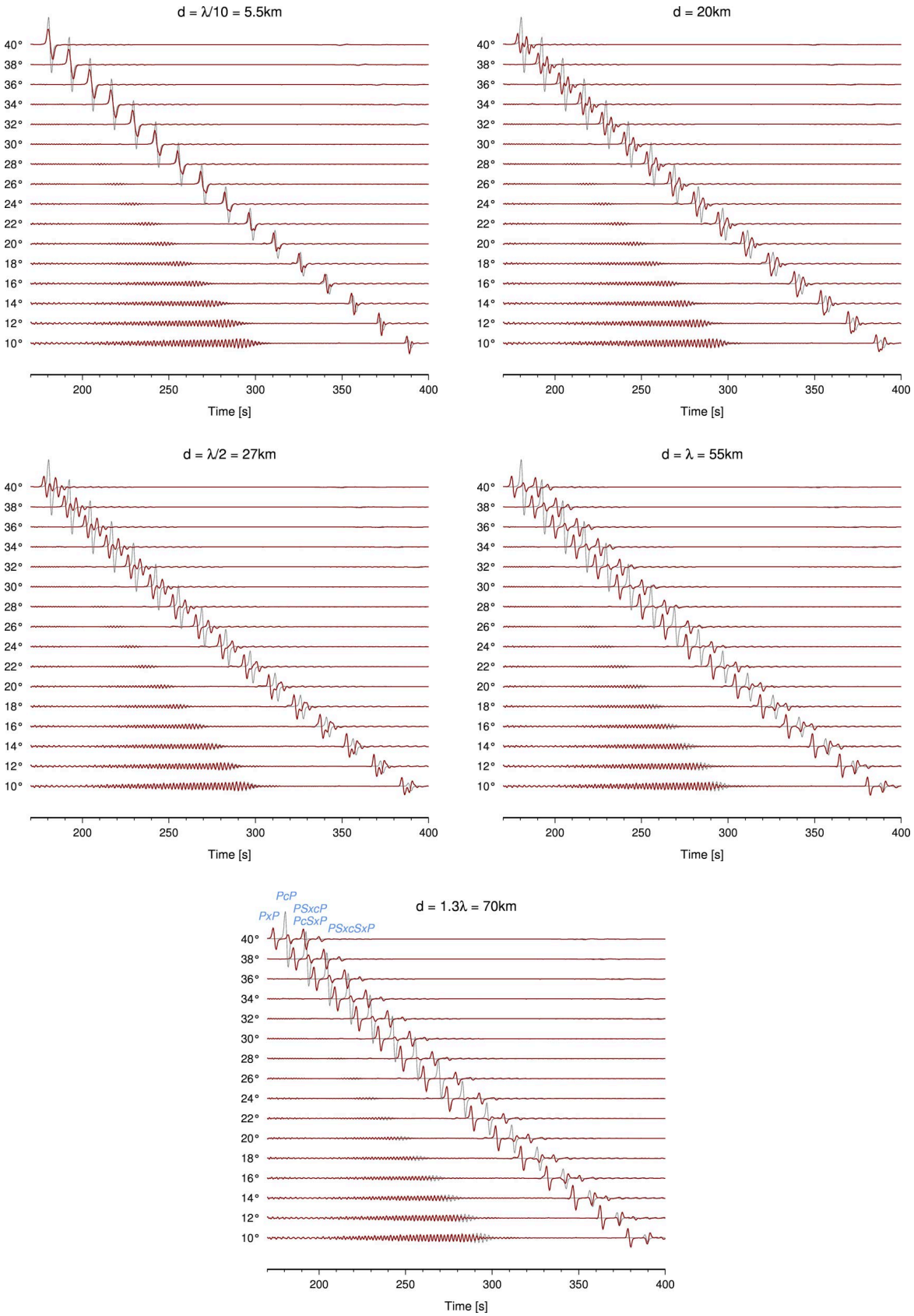

Fig. 3.16: Velocity proportional waveforms for model -10%-30%+30% and a first order **discontinuity** atop the ULVZ. Grey seismograms show the smooth results, whereas the red traces refer to the ULVZ model illustrated for the five different anomaly thicknesses. The produced pre- and postcursors are marked at d = 70 km. Note that the scaling is little different compared to figures 3.14 and 3.15.

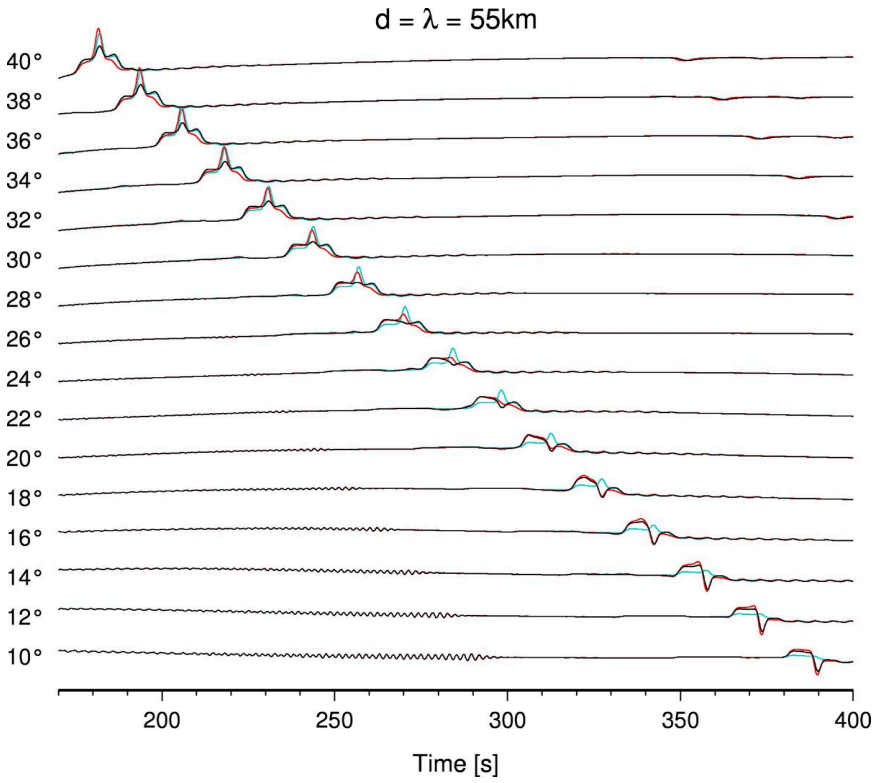

Fig. 3.17: Comparison of waveform distortion. The models -10%-30%+30% (black), -10%-30%+15% (blue) and -5%-15%+30% (red) are shown. For distances up to 20° the models with +30% density generate equal waveforms.

So far, only waveforms for model -10%-30%+30% has been shown. However, in correlation with the reflection coefficients it should be clear that waveforms behave in a similar manner for all other ULVZ configurations. With increasing layer thickness the impulse base becomes extremely broadened and is overlain by a notch that fits the input signal frequency. The smoother the low-velocity anomaly, the smaller are these waveform features. In case of $\delta|V_P| = \delta|\rho|$ the pulse shape is primarily a spike. A comparison with the results of lower velocity contrast ratios of 1:2 shows also equivalent impulse effects.

Summary of sections 3.3 and 3.4

- Damping effects are negligible within the studied distance range and anomaly thicknesses.
- Beginning of the waveform distortion at d = $\lambda/2$ beyond 30° using T = 4 s.
- Broader impulse bases for increasing layer thickness, distance and model contrasts.
- Travel time differences of PcP cannot be observed.
- Half-space reflection coefficients can reproduce the amplitude behaviour of $\mathrm{PcP}^{mod}/\mathrm{PcP}^{smooth}$
- The larger the density variance, the larger is the distance for the polarity change.

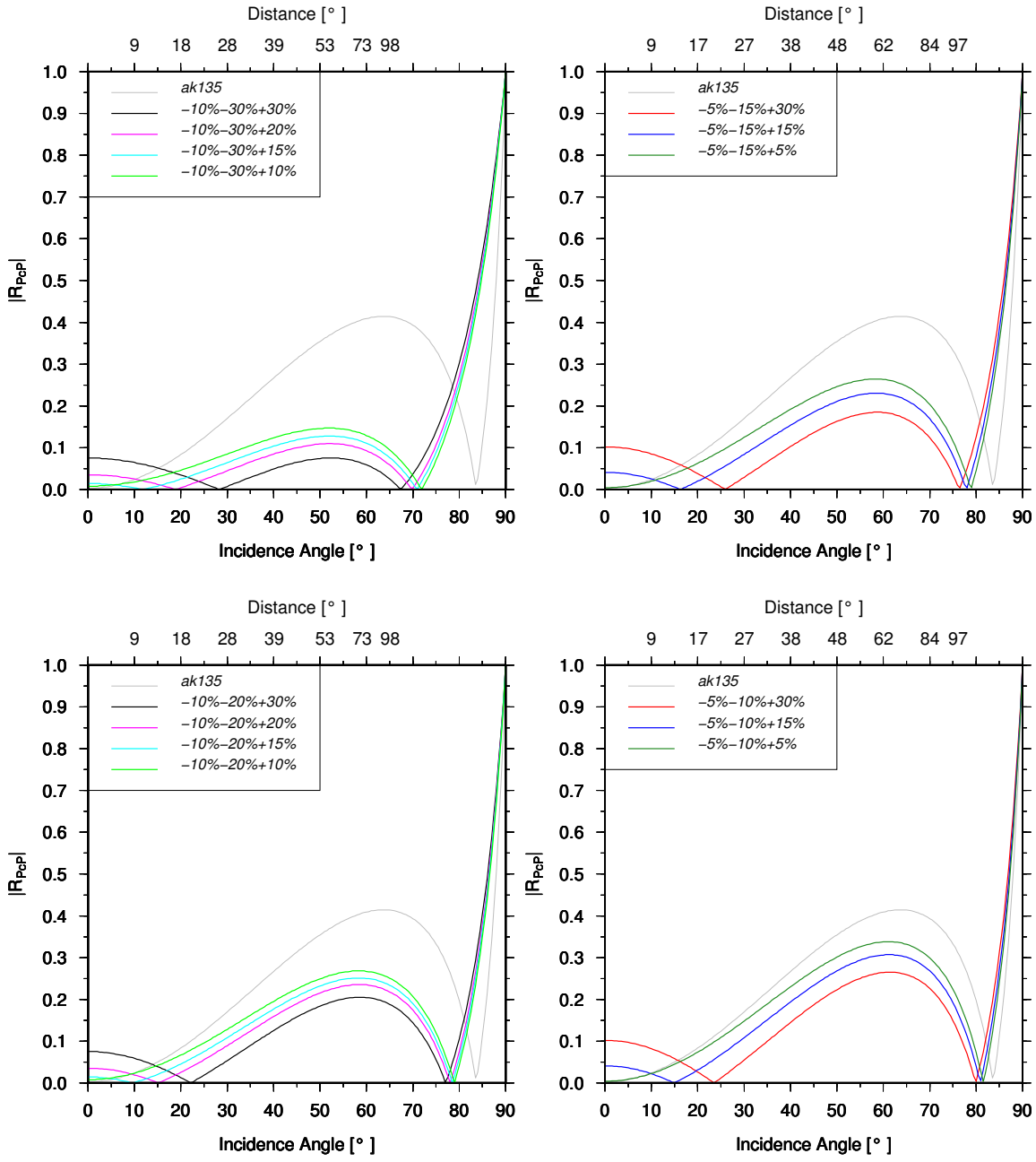

Fig. 3.18: Reflection coefficients of PcP for the ULVZ models used. The figures are split with respect to velocities since the calculated epicentral distance depends on the P velocity. Therefore the incidence angles refers to different distances when varying P velocity reductions are used. The grey line shows the coefficient for the global model. Note that the shown distances does not coincide with the smooth incidence angles (cf. figure 3.1). **Top:** δV_P to δV_S = 1:3 . The absolute half-space coefficients are consistent with synthetic seismograms and related amplitude ratios. **Bottom:** δV_P to δV_S = 1:2. Reflection coefficients remain constant up to an incidence angle of about 15° and are larger beyond that point than for a greater shear velocity reduction of 30%. The occurrence for polarity reversals are little shifted to closer distances.

3.5 Modelling with Wavelets of 1 Hz

Explosion sources have a typical source period around 1 second when observed at teleseismic distances. Therefore the systematic PcP study was repeated using a wavelet of 1 Hz. When the source frequency increases by a factor of four the number of samples per wavelet decrease by the same value down to 5. In order to preserve a higher wavelet sampling, the time increment has been shortened to 0.1 s. In this context the number of samples of the seismogram have been doubled to 8192 points which yield again a trace length of 819.2 seconds. Unfortunately, the numerical noise becomes much larger using a sampling rate of 10 Hz. Different cosine tapers and time domain aliasing suppressions were tested to reduce these aliasing effects. Finally, an upper frequency limit of 4 Hz and no cosine taper were used. In addition, a time domain aliasing suppression of 400 s was applied. The noise still remains stable and does not influence the PcP signal. Otherwise all further parameters remain constant.
The diagrams below are based on calculations for dissipative media by the parameters of ak135 Kennett et al. [1995]. Here three different thicknesses were tested, according to the wavelength λ of about 13.5 km at the CMB.

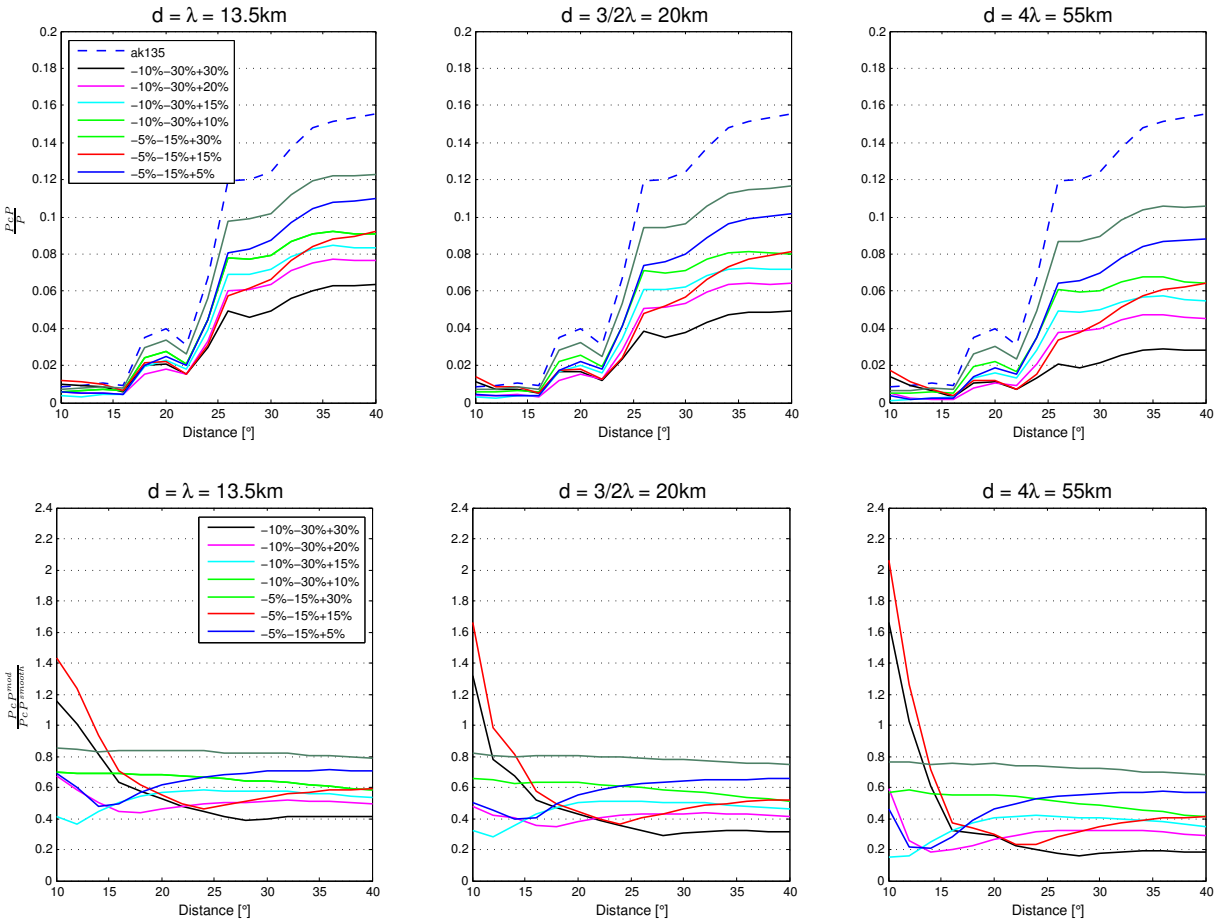

Fig. 3.19: Amplitude ratios for modelling with a dominant source period of 1 s in case of **gradient** ULVZ. The anomaly thickness refers to a wavelength λ of about 13.5 km at the CMB. **Top:** PcP/P scaling. **Bottom:** $\mathrm{PcP}^{mod}/\mathrm{PcP}^{smooth}$ amplitude ratio. Concerning a thickness of 20 km, PcP is about 10% smaller using a wavelet of 1 Hz compared to a source period of 4 s (cf. figures 3.4 and 3.5). Short-period wavelets may enhance the resolution of thin anomalies.

Since the half-space reflection calculations are independent from the signal frequency, the location of polarity reversals should be retained.
Figure 3.19 presents the results for the PcP/P ratio and PcP scaling using gradient ULVZs. The same main features occur for this short-period computations at 1 Hz. Density and velocity effects for near and far distances, respectively, as well as polarity changes are in agreement with the results of the 4 s modelling. Generally, amplitude ratios decrease with increasing layer thickness. The differences between the two source frequencies refer to the layer thicknesses and the wavelengths. In general, both amplitude ratios for d=λ=13.5 km coincide with the results of a d=20 km using a 4 s source period. This feature is most pronounced for distances beyond 30°. Little variations occur in the steep-angle range. Furthermore, amplitudes for 3/2λ=20 km (1 s) calculations equal the PcP scalings in case of λ/2=27 km (4 s). For instance, at a distance of 40° the PcP/P ratio is 0.6 for d=20 km (4 s) and also for d=13.5 km (1 s). Similarly, PcP/P is 0.5 for d=λ/2 (4 s) and also for d=3/2λ=20 km (1 s). Compare also figure 3.22. Consequently, this means that any amplitude ratio (> 30°) could results from a thinner layer when a dominant source period of 1 s is considered. In other words, concerning a thickness of 20 km, the PcP impulse is about 10% smaller using a wavelet of 1 Hz compared to a source period of 4 s. Thus, a short-period signal may enhance the resolution of thin anomalies. Otherwise, a numerical uncertainty cannot completely ruled out even the influence of the number of homogeneous layers has been tested. For this purpose those number has been both increased and reduced for the calculations at 1 Hz. A doubled number of homogeneous layers generates no changes in the seismograms, i.e. the chosen approximation of the velocity gradient is still sufficient for that short-period wavelet. For halved layers the computations become unstable and the signals cannot be produced.

The frequency dependent interrelation of thickness and wavelength can also be observed in the waveforms illustrated in figure 3.20 for the example of model -10%-30%+30%. When the anomaly thickness amounts to one wavelength of 13.5 km, the impulse shapes still fit the smooth waveform beyond 30° (which is in correlation with the findings for d=20 km (4 s)). For closer distances the generation of a negative peak can be noted as mentioned above. However for a somewhat thicker layer of 3/2λ = 20 km, a waveform distortion occurs at distances beyond 30° which coincide with the 4 s modelling at λ/2 (see blue ellipses). The base of the pulse becomes broader and a weak notch develops. Hence, relating to the wavelengths, an ULVZ has to be three times thicker using a wavelet of 1 Hz to create a waveform distortion compared to a source period of 4 s. The amplitude ratios at 55 km are identical with the 4 s solutions and therefore independent from the wavelength. Again, the wave deformation is much more pronounced. The polarity reversal becomes very clear with an accompanying impulse base broadening about 13 seconds. The produced notch fits the frequency of the wavelet.

The amplitude results for a first-order discontinuity using a source frequency of 1 Hz are given in figure 3.21. The uppermost row shows the PcP/P ratio. As in case of the 4 s modelling, the amplitudes do not decrease with increasing ULVZ thickness (cf. figure 3.9). It should be noted that also for discontinuities the 13.5 km thick layer can be compared with a 20 km thickness using a 4 s wavelet since amplitudes do not further decrease for thicker layers than 13.5 km or 20 km, respectively. Therefore, short-period signals may enhance the resolution of such first-order discontinuity low-velocity anomalies.

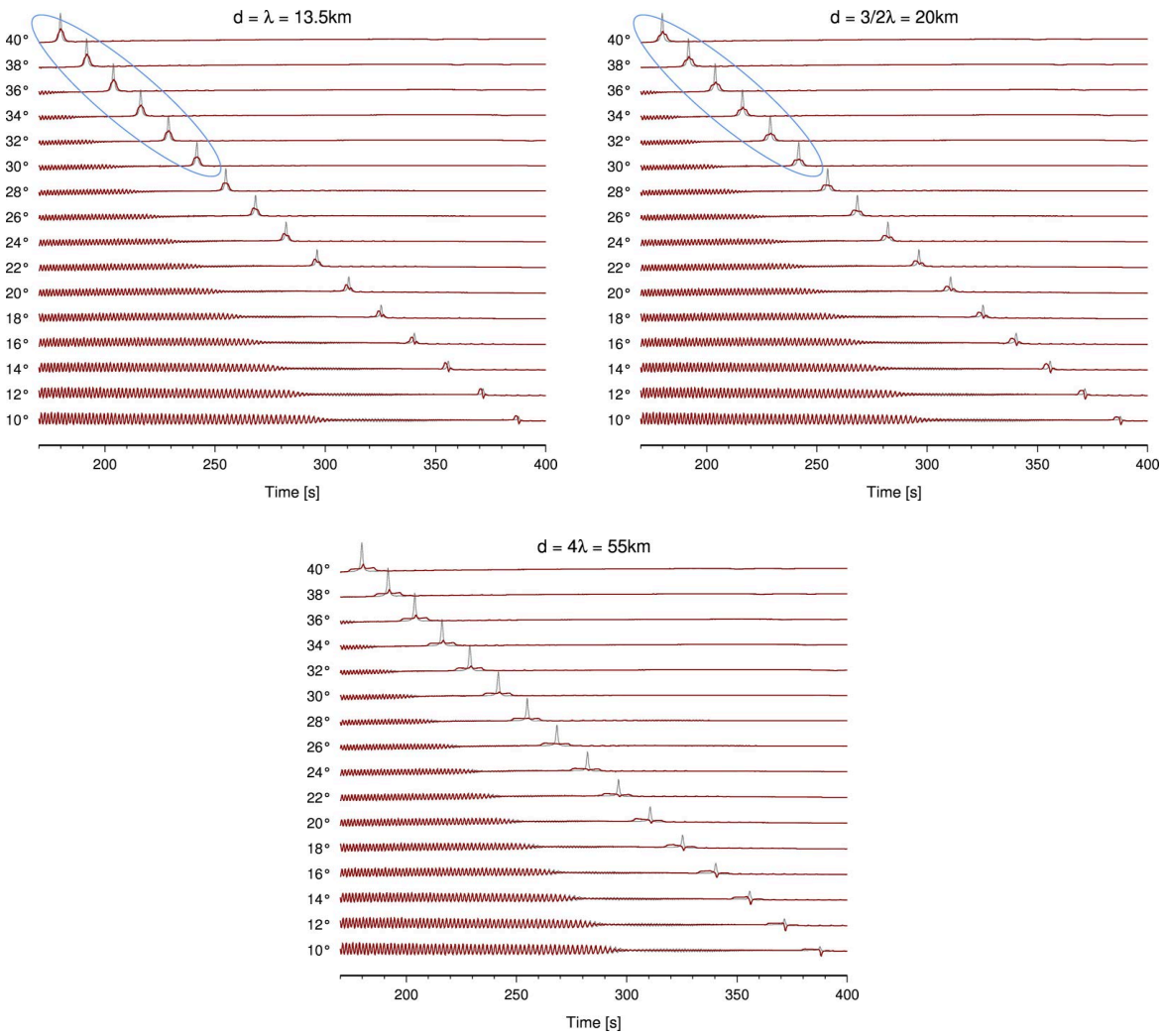

Fig. 3.20: Displacement proportional waveforms for model -10%-30%+30% and **gradient** ULVZ using a source period of 1 s. Grey seismograms show the smooth results, whereas the red traces refer to the ULVZ model illustrated for the three different anomaly thicknesses. Larger numerical noise occurs using a sampling rate of 10 Hz. The beginning of the waveform distortion at distances beyond 30° is marked with the blue ellipse.

Similar statements are true for the PcP scaling shown in the middle row of figure 3.21. The relations of PxP to PcP do not change for short-period source time functions. The small deviations of the peak amplitude ratios rise from the location of the polarity reversals and lead to measurement uncertainties as already mentioned in section 3.3. The thinner the anomaly are, the more interference occurs between the precursor and PcP. In combination with the attenuation this causes a lower precision of amplitude measurements.
In conclusion, it can be said that the analysis of different source frequencies yields a complex interrelation of the wavelength and layer thickness. This behaviour is summarised in figure 3.22 for the example of the gradient model -10%-30%+30% model at 40°. The PcP/P ratio is here a function of the wavelength. Short-period signals may enhance the resolution of thin anomalies since an ULVZ seems to be thicker (+7 km) when a source period of 4 s is applied.

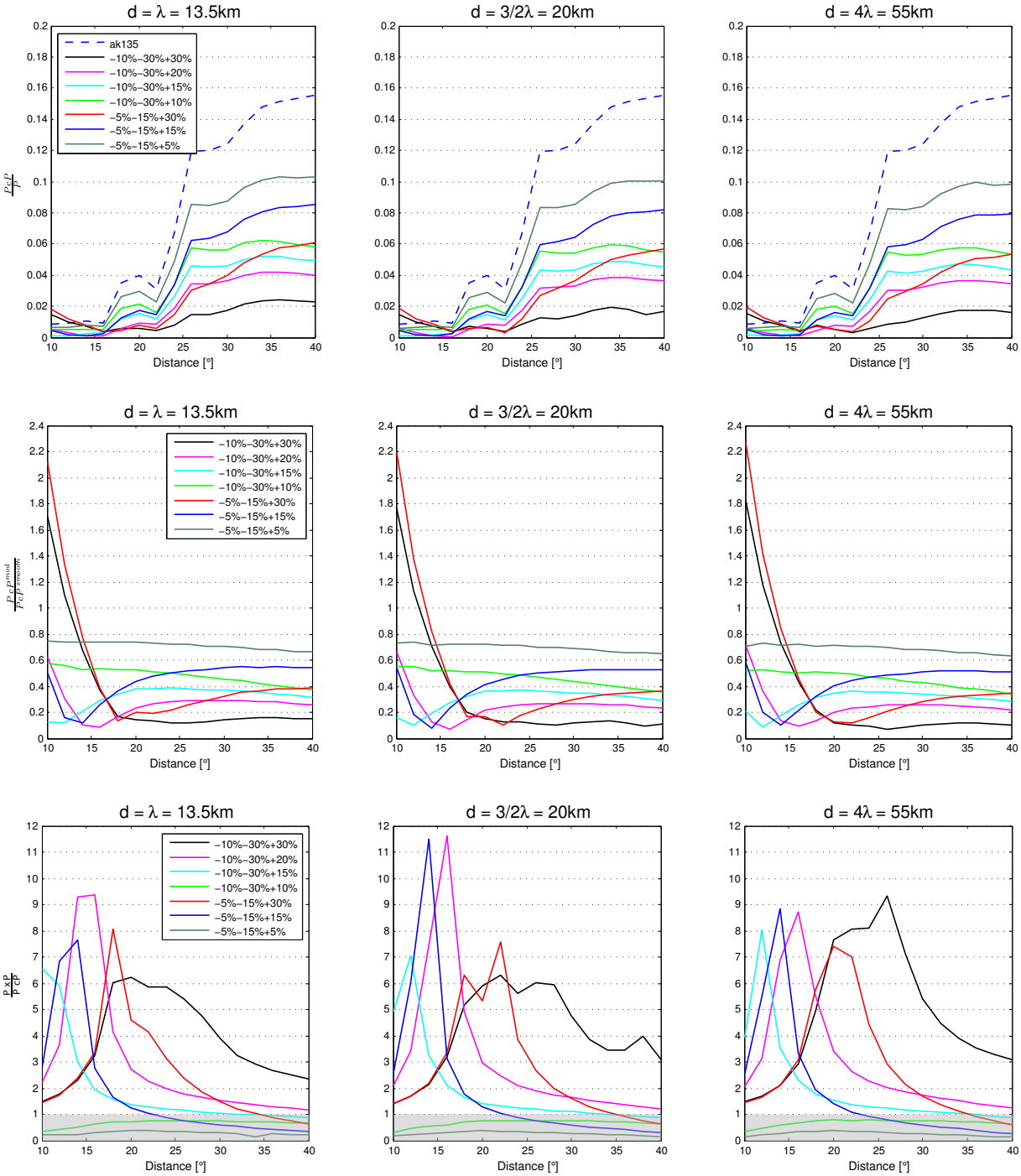

Fig. 3.21: Amplitude scaling for models with first-order **discontinuities** atop the ULVZ using a wavelet of 1 Hz. From top to bottom: PcP/P, PcP^{mod}/PcP^{smooth} and PxP/PcP. PcP does not decrease for increasing anomaly thicknesses as in case of the 4 s calculations. A short-period source yields no enhancement of the resolution. Compare to figures 3.8, 3.9 and 3.10 for the 4 s wavelet.

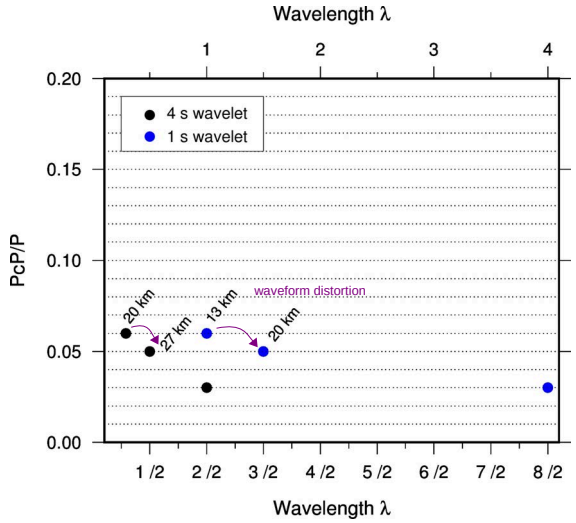

Fig. 3.22: Frequency dependent interrelation of the wavelength and anomaly thickness. Shown are the PcP/P measurements of the gradient -10%-30%+30% model at 40°. A 20 km thick anomaly, using a wavelet of 4 s, yields the same amplitude ratio as a 13 km thick ULVZ and a 1 s wavelet. Therefore, short-period signals may enhance the resolution of thin low-velocity anomalies.

The only possibility to make a statement about the basal layer thickness seems to be the investigation of travel time differences between PxP and PcP which is given in figure 3.23. The times were measured from peak amplitudes on the attenuated, velocity proportional seismograms using a wavelet of 1 Hz. The solid lines show the results of model -10%-30%+30%, dashed lines for model -5%-15%+5%. The colours refer to ULVZ thicknesses of 13.5 km, 20 km, 27 km, 55 km and 70 km, respectively. For a 5.5 km thickness PxP cannot be separated from PcP. In addition, a comparison with travel time differences with a 4 s source period were made for 55 km where no frequency induced deviations occur. The arrival time difference for model -10%-30%+30% is larger since the medium is comparatively slower than for -5% V_P, -15% V_S. Thus the travel time difference between PxP and PcP increases. This time shift becomes larger for increasing layer thickness and amounts up to about 0.2 s for 13.5 km and 20 km and about 0.5 seconds for 55 km.

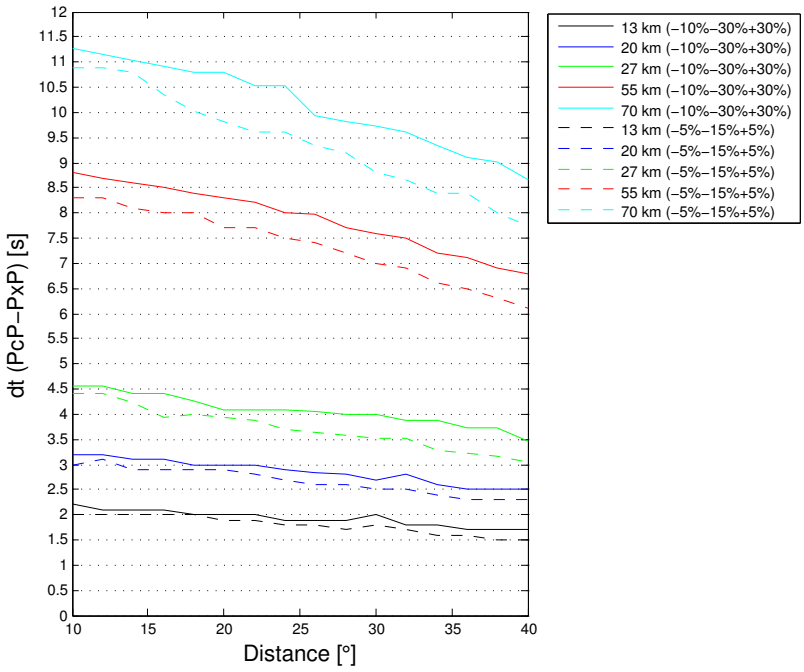

Fig. 3.23: Travel time differences dt of PxP to PcP using attenuated, velocity proportional synthetic data with a wavelet of 1 Hz. Times were measured at peak amplitudes. Solid lines show the results of model -10%-30%+30%, dashed lines for model -5%-15%+5%. Different colours refer to ULVZ thicknesses of 13.5 km, 20 km, 27 km, 55 km and 70 km, respectively. The travel time difference for model -10%-30%+30% is larger since the medium is slower than for -5% V_P, -15% V_S. Thus the travel time of PcP with respect to PxP increases. This time shift becomes larger for increasing layer thickness and amounts to about 0.5 seconds for 55 km but only up to 0.2 s for 13.5 km and 20 km.

3.6 Notes on Theoretical Ground Velocities

Amplitude ratios were measured from theoretical ground displacements. Since most of the instruments record ground velocities a comparison of displacement and velocity proportional synthetics is shown here. Figure 3.24 illustrates the gradient results for a 55 km thick anomaly using source periods of 1 s and 4 s. PcP^{mod}/PcP^{smooth} and PcP/P relations are shown. The derived ground velocities are indicated as dashed lines. As has been shown in section 3.1 the strong velocity gradient atop the ULVZ causes also weak pre- and postcursors on velocity proportional traces instead of waveform distortions on displacement seismograms. Thus, the amplitudes were determined from the whole signal.

Obviously, significant frequency dependent effects do not occur for this layer thickness. Regarding to the PcP scaling, within the steep range up to 15° and beyond 35° no decisive differences can be observed. Again, the largest variances coincide with the PcP polarity reversal of the highest density contrasts (+20% and +30%) where the signal completely diminish and amplitude measurements are less precise and definite.

An analysis of the PcP/P ratio reveals slightly larger variances between 18° and 35° where the deviation amounts up to -0.02 s around 30° for all models. Solely at 20° a negative kink occurs for a 1 Hz wavelet. However, all important effects discussed above are preserved. These negative amplitude anomalies on velocity proportional traces are also true for thinner ULVZ layers (not shown here). When a first-order discontinuity is included the variances between displacements and velocities are small and within the bounds of resolution.

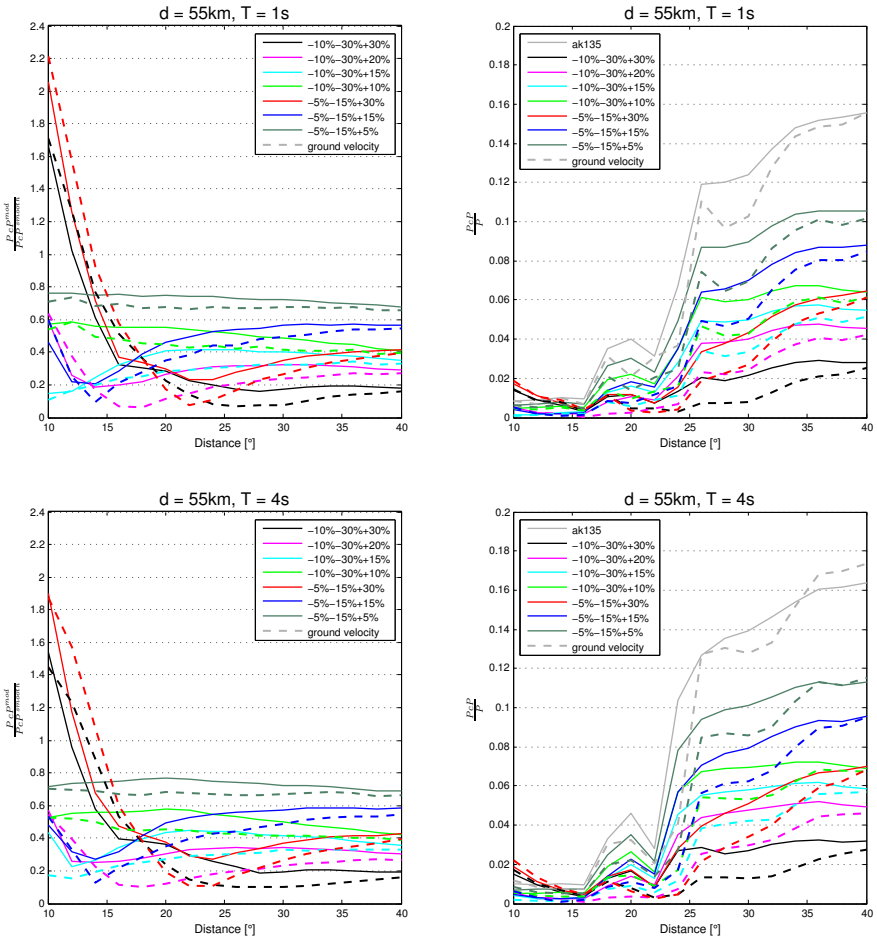

Fig. 3.24: Comparison of theoretical ground displacements (solid line) and velocities (dashed line) for an ULVZ thickness of 55 km. **Top:** Using the short-period wavelet of 1 s and **Bottom:** for a dominant source period of 4 s. The gradient models are shown for $\mathrm{PcP}^{mod}/\mathrm{PcP}^{smooth}$ and PcP/P relations, respectively. No frequency dependent features can be observed for both PcP scalings. The small differences for that relations result from polarity reversals where PcP diminish and measurements are less precise. For a PcP/P amplitude ratio the deviations are larger between 18° and 35° up to -0.02. However, all important characteristics described above are preserved.

Concluding, this shows that a comparison of synthetic displacement amplitudes with real ground velocities is allowed with respect to $\mathrm{PcP}^{mod}/\mathrm{PcP}^{smooth}$ considerations and discontinuities atop an ULVZ. In case of PcP/P amplitude measurements on gradients the deviation between 18° and 35° have to taken into account.

3.7 Notes on Spectral Components

Beside the amplitude ratios and waveforms also the spectral components of PcP were inspected. Though, it is not possible to compare the frequency domain of real data with the synthetic results and a detailed analysis has no practical purpose. Therefore the following will only depict the qualitative findings using a Fourier transform.

The spectral investigation were applied using a time window of 30 seconds around the PcP signal and a thickness of 55 km. Density contrasts of +30% show greater amplitudes than the smooth model at 10° and 12° which is in agreement with the amplitude ratio diagrams and

waveforms. At 14° distance the amplitudes are only enlarged within the low-frequency range up to the source period. The amplitude increase for higher periods correlates with the waveform broadening described in section 3.4. Also the models with a density contrast of +15% indicate a similar spectrum independent from their velocity configuration. For increasing distances the model with the smallest velocity and density contrast reveals the largest amplitudes over the entire frequency range whereas model -10%-30%+30% results in the lowest spectrum.
These results are true for gradient ULVZs as well as for first-order discontinuities. Hence, the manifold low-velocity features can be also seen on spectral components.

3.8 Modelling using Raytracing

So far synthetic seismograms have been calculated using the usual reflectivity method. In order to verify the obtained characteristics of PcP the Gauss-Beam method (GBM) was used. As mentioned in section 2.3 the advantage of this method is the analysis of single phases and the modelling of 2D effects on discontinuities. The reflectivity method only allows the computation of 1D models, i. e. medium parameters can vary only with the depth. In the Gauss-Beam calculations the generation of the pre- and postcursors can be controlled and synthetic seismograms will be calculated for each phase separately. At first, the assumed flat models were applied to the GBM to compare them with the reflectivity results. Subsequently, different topographies were included atop the low-velocity basal layer.
The graphic user interface of the program *Xgbm* is based on the FORTRAN code by Weber [1988] and is described in Davis and Henson [1993]. Firstly, the smooth global model ak135 with first-order discontinuities only at the Moho and the CMB was used as input model. The lateral range of the model was restricted to 90°. A model can be displayed as flatten earth using the EFA by Müller [1977] or as radial symmetric earth, where ray tracing processes only work for the flat earth model. The region between the discontinuities is divided into several layers at which the number is defined in the input model (here 31 layer). Each layer is decomposed into triangles of different sizes which represents slowly or fast varying structures. The width of the triangles is 100 km. Inside a triangle the velocity and density parameters varying linearly. Thus, the triangles correspond to the number of homogeneous layers in case of the reflectivity method which approximates the gradients. A constant quality factor is applied to each triangle. The source was located at a depth of 130 km and the receivers cover a range of 10° to 50° with a spacing of 2°. Each phase can be selected individually as well as the number of rays. The larger this number, the more rays arrive at the receivers. Hence, to increase the precise of the calculations a sufficient number of rays should be chosen. For the following computations 400 rays are used, respectively.
Figure 3.25 shows the P and PcP ray paths only with 100 rays, respectively, in order to enable visualisation. The triplications, caused by the steep velocity gradients within the upper mantle transition zone, can be seen very clearly. Strong focusing effects can be expected at 16°, 20° and 22°. The scaling of the figure refers to the earth's radius in km. The appropriate minimum and maximum take-off angles are determined automatically by the program.
The same parameters as in case of the reflectivity method were used to calculate synthetic seismograms by *Xgbm*: an explosion source with a source time function that equals a Küpper signal with one maximum and a duration of 4 seconds. This single peak corresponds to a displacement proportional impulse shape in the far-field. Furthermore, a sampling rate of 5 Hz and 4096 samples per seismogram were set so that the trace length is again 819.2 s. However, the application of a velocity reduction is not possible with the GB program. The latest Gaussian beam parameter described in section 2.3 was applied as well as the absorption mode.

3.8.1 Flat ULVZ

Similar to the usual reflectivity method only traces with P and PcP were calculated. At a first step the pre- and postcursors were generated (as they are drafted in figure 3.7) by the ray tracing program since they are not included in the provided phase list. The production of non-standard

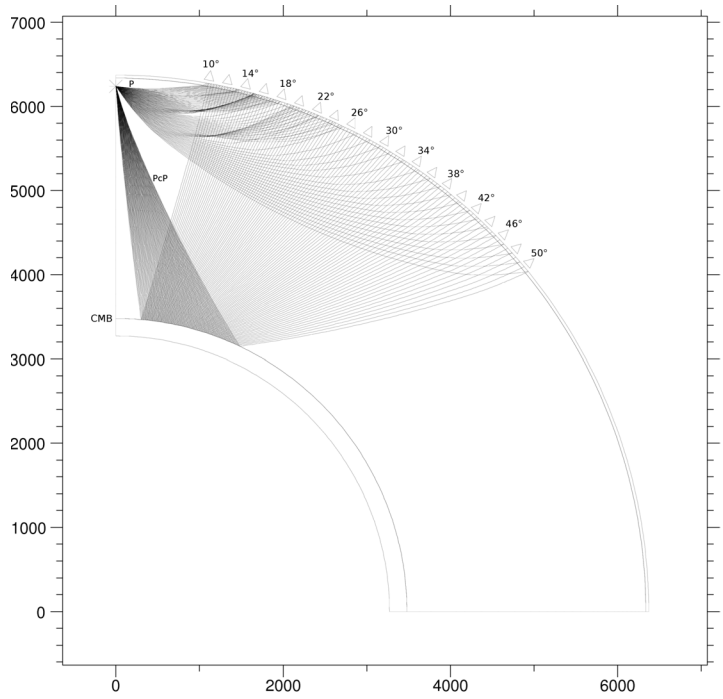

Fig. 3.25: Ray paths for the used smooth model using the Gauss-Beam method. The extension of the spherical earth was restricted to 90°. The scaling of the figure refers to the earth's radius in km. An explosion source was set to a depth of 130 km and the receivers cover a range between 10° and 50°. To enable the presentation only 100 rays per phase are shown here.

phases is the most important advantage of this program because thereby an identification of unusual signals is possible. Figure 3.26 displays the amplitude relations based on the GB synthetics. All model configurations as used before were applied to the GB method in case of a 55 km thick ULVZ with a first-order discontinuity.

The overall distance dependent velocity and density effects can be reproduced as shown for the reflectivity method in figures 3.8, 3.9 and 3.10. Up to 14° the modified PcP amplitude is enhanced for the largest density contrasts of 30%. Beyond the polarity reversal locations the velocity effect becomes prominent at which the moderate velocity contrasts of -5% V_P and -15% V_S result in higher amplitudes and different slopes compared to the -10% V_P and -30% V_S modifications. When $\delta|V_P|$ equals $\delta|\rho|$ the distance dependency is fairly weak (cf. figures 3.8 and 3.9).

The differences between these two methods appear mostly at 30° and 38° which are already visible as fluctuations on the smooth PcP/P amplitude ratio. A comparison of the waveforms between reflectivity and GB synthetics has shown a varying P amplitude where PcP remains unchanged. Therefore these anomalies in the PcP/P diagram result from the GB P-wave which may arise from poor ray coverage. Similar negative kinks could be seen on the velocity proportional amplitude ratios of figure 3.24. At the PcP^{mod}/PcP^{smooth} diagram the only decisive variance occur at 10° for the models -5%-15%+5% and -10%-30%+10%. The main deviation refers to a comparison of the PxP/PcP relations (see figure 3.10). In case of the reflectivity method the density characteristic before the polarity change is also visible on the precursor scaling. In contrast, the GB synthetics reveal no such agreement. Within the steep-angle region all models are well separated and solely the peak amplitude ratios correspond to the polarity reversals. The location of the polarity reversals are much more discrete whereby the amplitude

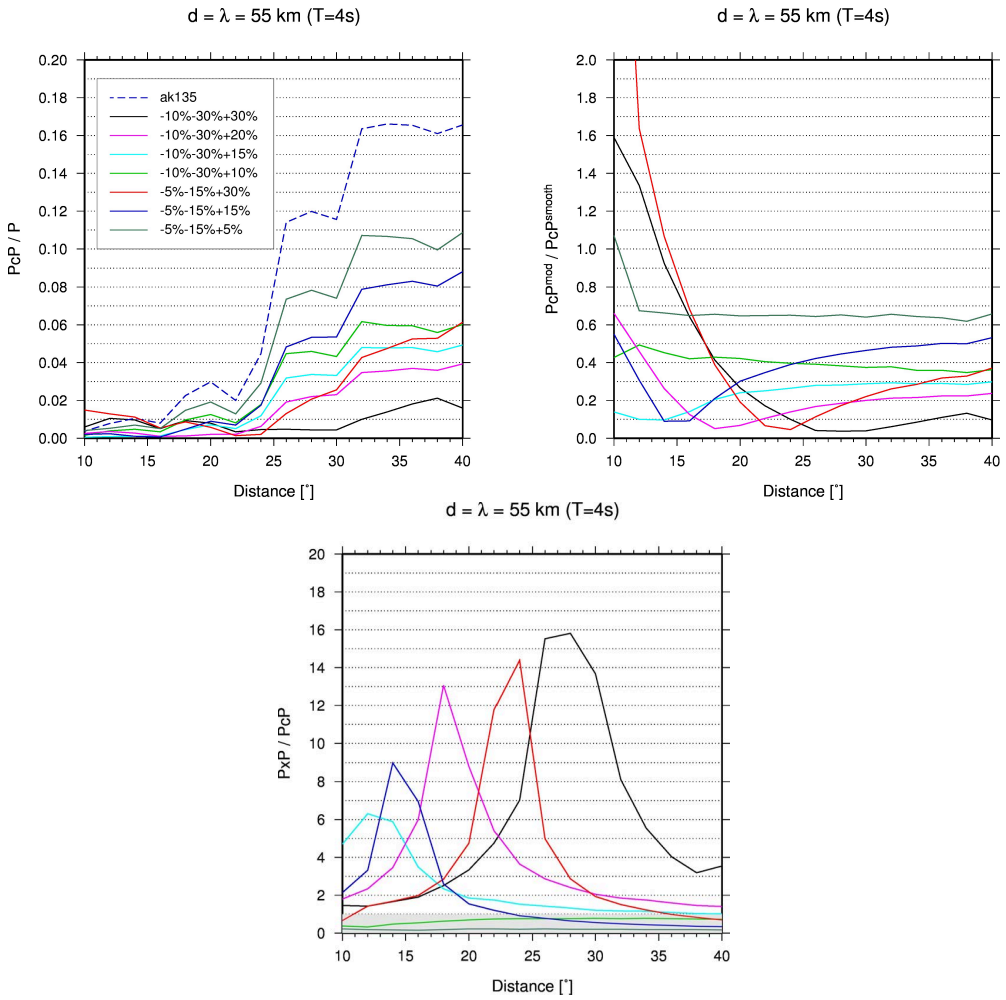

Fig. 3.26: Resultant PcP amplitude ratios using ray tracing by the Gaussian beam method. The same models were applied as in case of the reflectivity method. Compare figures 3.8 (middle right), 3.9 (middle right) and 3.10 (bottom left). The GB synthetics were calculated for a ULVZ thickness of 55 km and a first-order discontinuity with a source period of 4 s. In general, all distance dependent effects on PcP/P and PcP^{mod}/PcP^{smooth} ratios can be reproduced. The main deviation occurs for the precursor scaling.

behaviour appears distorted. Furthermore, measured peak amplitude ratios are higher using the GB method but this attribute results again from the resolution of the polarity change when PcP decreases. Hence, the region of polarity reversals should be carefully considered. However it should be noted that the overall amplitude trends are preserved: The highest model contrasts of -10%-30%+30% and -10%-30%+20% create always larger PxP than PcP and a constant ratio is obtained for equal V_P and density contrasts.

The computation of synthetic GB seismograms was repeated for a gradient low-velocity layer. Though, the resultant amplitude characteristics are in good agreement with the reflectivity method whereas a waveform distortion could not be generated.

Moreover, *Xgbm* enables the generation of travel time tables for the desired phases PxP, PcP, PSxcP, PcSxP and PSxcSxP. A comparison with the determined travel time differences of PxP to PcP displayed in figure 3.23 verified the correct identification of the pre- and postcursors and confirm the reflectivity results.

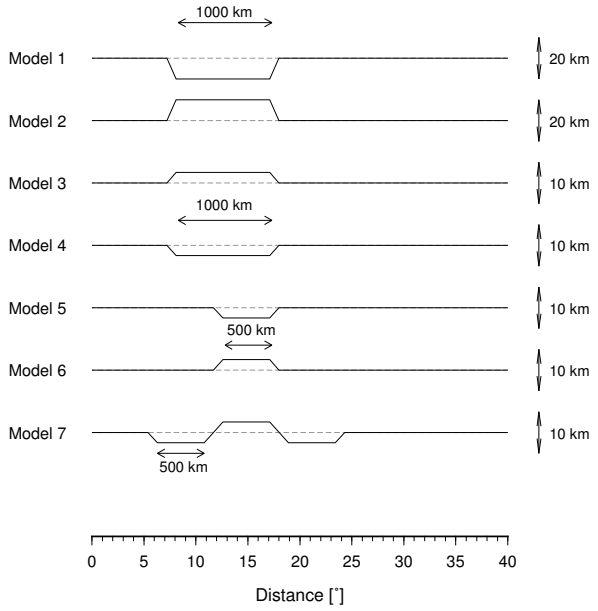

Fig. 3.27: Sketch of tested undulations on a low-velocity basal layers above the CMB. Model -10%-30%+30% with a layer thickness of 55 km were used. The dashed grey lines refer to a flat upper ULVZ boundary. A topography width of 500 km and 1000 km were used plus ups and downs of 10 km and 20 km, respectively. Model 7 is a combination of both. The distance scale meets the range at the lower mantle as well as the surface due to the flatten earth approach.

3.8.2 Undulations on the ULVZ

A reflector such as a low-velocity zone will probably not exhibit a simple flat upper boundary. Rather, strong and/or weak undulations can be assumed which induce focussing and defocussing effects on the pre- and postcursor of PcP. It has been shown by Kampfmann and Müller [1989] that a topography at a short-period source signal of 1 Hz produces huge amplifications and reductions of PcP using different periodic topography on the CMB. They used small- and large-scale undulations with a height of 1 km and 0.5 km, respectively. Those models with a long-wavelength undulations from 100 km to 600 km reveal strong amplitude scattering between medium (25°) to large (70 °) distances. Variances up to 50% could be generated for topography widths of 200 km and 400 km where the minimum and maximum deviations alternate within distances less than 5° - 10°.

Similar effects should be expected in case of an ULVZ with a first-order discontinuity. Here seven topography models were embedded onto a 55 km thick low-velocity zone of the configuration -10%-30%+30% and are drafted in figure 3.27. The shown distances meet the location of the reflection but also the surface distance using the EFA. Moreover, the distances in degrees can be regarded as an approximation of the incidence angles. Large-scale undulation widths of 500 km and 1000 km were applied as well as elevations and depressions of 10 km and 20 km which are denoted by ups and downs in the following figure, respectively. Model 7 is a combination of two downs and one up. In addition, a potential frequency connection was investigated for the PxP/PcP displacement amplitude ratio displayed in the upper diagrams of figure 3.28. The flat ULVZ solution is shown as dashed, grey line.

A comparison of the 4 s and 1 s results in figure 3.28 (top row) indicates only few differences. As a consequence of the better resolved polarity reversal, enormous amplitude ratios occur for

the short-period diagram. Models 6 and 7 create remarkable deflections at 28° and 30° for a source period of 4 s in contrast to the short-period solution where all models produce huge amplitudes ratios at that range. Otherwise, focussing and defocussing effects look very similar for the different models. An example is discussed for model 2 and 6 (cf. figure 3.27) at 22° and 24° also for both source frequencies. Model 2 (yellow line) is twice as large as model 6 (dark red) but yields the same scattering up to +60% respect to the flat ULVZ. The only common feature is the topographic high. At 38° model 2 produces for T=4 s a strong defocussing instead of the amplification for T=1 s. The greatest contrast with respect to the other models is obtained for model 7, the combination of up and downs, since already the first reflection point at 5° (epicentral distance is 10°) hit the undulation. Models 1-4 have the first reflection at about 7° and models 5-6 at about 12°. Therefore large (de)focussing effects can be seen beyond 14° and 22°, respectively. Minor scattering within the steep-angle region arise from weak discontinuity undulations due to uncertainties in model preparation.
The lower diagrams of figure 3.28 illustrate the topography influence on the PcP/P and PcP^{undu}/PcP^{smooth} scaling. Only the results for a 4 s signal are shown since the short-period effects are almost identical. The flat solutions are indicated as dashed, grey lines. Both diagrams reveal larger scattering for distances up to 18° and beyond 28°, i. e. within the range of polarity change no undulation configuration is able to amplify the PcP signal. For the larger distances the deviations amounts up to ±50%. The near distance fluctuations are more pronounced on the PcP scaling. Here the models 2, 3 and 7 cause defocussing effects whereas model 1 and 4 result in small focussing features. The overall influence on PcP is weak since the wave is only transmitted through the ULVZ.

Beside the strong amplitude variations a topography on the low-velocity upper boundary also influences the travel time of the pre- and postcursors. The travel time differences of PxP compared to the flat ULVZ were determined from the peak velocity proportional amplitudes and are displayed in figure 3.29. The solutions for a 4 s wavelet were used. The diagrams are separated with respect to the topography width of 500 km and 1000 km to enhance the presentation. A waveform distortion can only be recognised for the largest model 1 of 1000 km by 20 km at an epicentral distance of 24° and 26°, which is also illustrated in the upper figure 3.30. The unusual travel time residual at 26° result from the wave splitting since times were measured at peak amplitudes. However, the first onset also agrees with the other travel times. At the edges of each topography, independent from the size, (almost) total defocussing occurs. This is denoted by open circles in figure 3.29. Solely model 2 (yellow) shows also defocussing in between the height. Hence, the large topographies of model 1 and 2 cause exceptionally dynamic features. In consideration of the ups and downs also travel time variances can be seen. In case of a width of 500 km the valleys cause doubled travel time residuals compared to the appropriate height models. This result from the fact that PxP propagates twice through a topographic low. The lower seismogram section of figure 3.30 shows model 7 with its up and two downs where the different travel time residual can be seen very clearly. With respect to the 1000 km undulations such a kinematic effect is only poorly developed even though 10 km or 20 km depressions were applied.

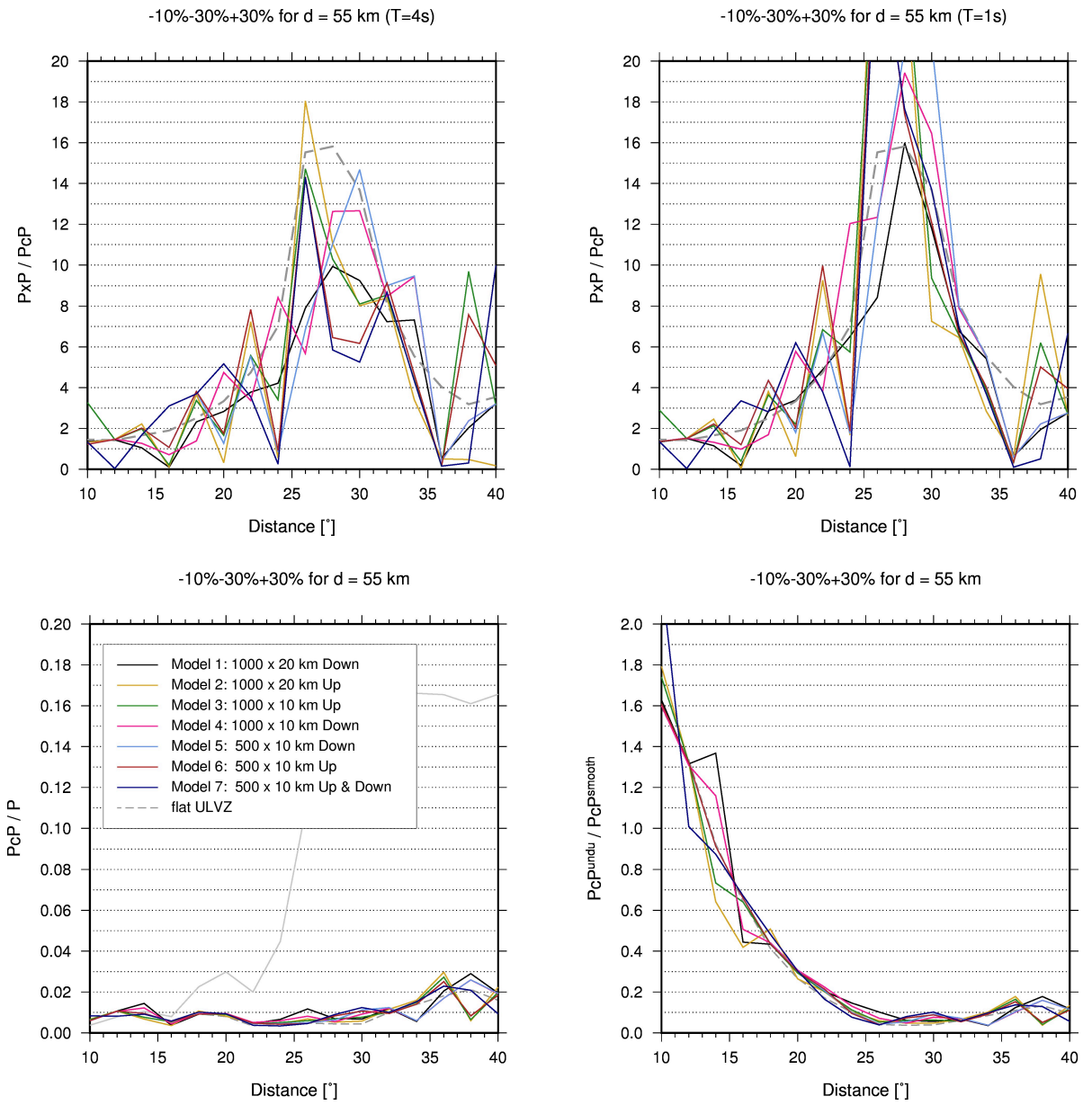

Fig. 3.28: Top: PxP/PcP displacement amplitude ratio using the topography models for dominant source periods of 1 s and 4 s. Undulations were tested for the -10%-30%+30% discontinuity model of 55 km thickness. Strong distance dependent focussing and defocussing effects occur which are in general independent from the source period. Entirely different undulations are able to produce similar or even equal amplitudes. For instance model 2 and 6 at 22° and 24°. **Bottom:** Relations of PcP/P and PcP^{undu}/PcP^{smooth}. The flat amplitude ratios are indicated as dashed, grey line. The smooth global model is also illustrated as solid, grey line. A topography atop an ULVZ reveals no significant influence on PcP amplitude ratios. All variations seems to be undetectable. Only the results for 4 s are shown here since the 1 s solutions are almost equal.

A correlation of defocussing on topographic heights, strong amplitude variations and the simultaneously absence of travel time shifts as mentioned by Thomas [1994] cannot be observed. She studied topography effects on the D" discontinuity with an V_P increase of 3% at a depth of 2605 km but using the same program. Obviously those attribute discrepancies result from the different medium contrasts, i.e. the overcritical reflections in her case. It should be noted that focussing and defocussing effects as well as travel time shifts are also seen on the postcursors,

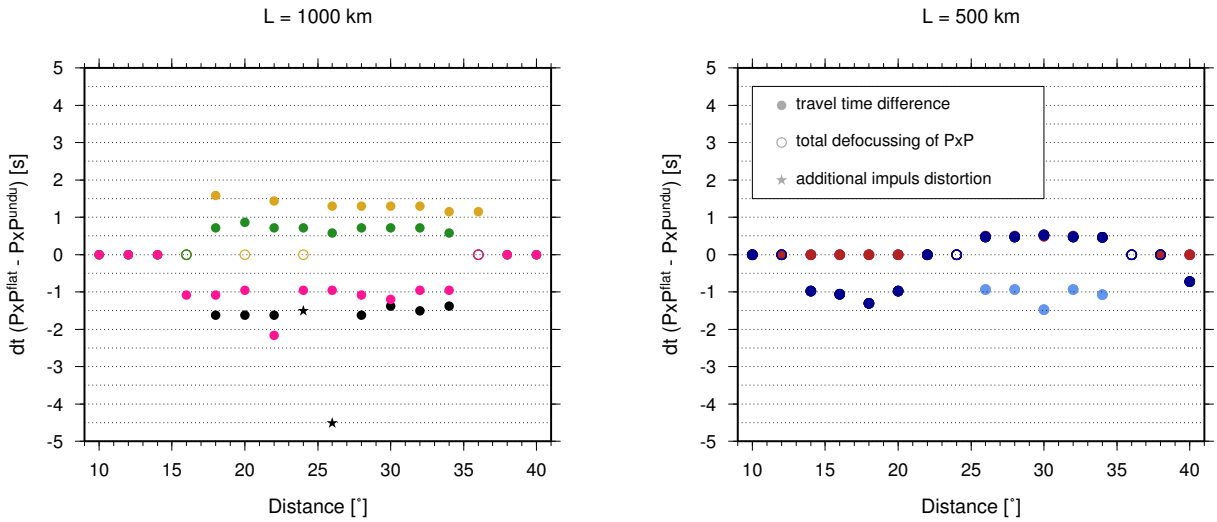

Fig. 3.29: PxP travel time differences between undulating and flat ULVZ. The colored dots refer to the seven undulation models illustrated in figure 3.28. Diagrams are separated respect to the topography width L of 500 km and 1000 km. Only for the largest undulation model of 1000 km by 20 km a waveform distortion (marked by black stars) occurs at 22° and 24°. The travel time differences in case of models with downs are larger compared to the appropriate 'up' model since PxP have to propagate twice through the valley. However, this kinematic effect is much more pronounced for the narrow downs of 500 km than for models of 1000 km width.

much stronger than for PcP, due to the underside reflection at the ULVZ discontinuity. However, this feature was not analysed in detail since postcursors are potential subjected to an interference with the source structure which is included in the PcP signal. Thus, only the exceptionally huge postcursor amplitude at 30° in figure 3.30 has to mention. PxP and PcP on the contrary remain constant compared to the nearest traces. As a consequence strong postcursor variations may occur within very short distance ranges of about 220 km. Furthermore, an inspection of the velocity proportional amplitudes yielded no discrepancy from the shown results. In conclusion from seismic records at the surface an assumption about a specific topography is not possible since manifold configurations are able to produce similar amplitude ratios. In addition, Schweitzer [2002] has shown that any interpretations about the CMB topography derived from travel time data should be regarded as highly unsure. Most of the observed residuals could also be caused by heterogeneities along the ray path or event location errors. Similarly, this is true for the ULVZ reflected phase PxP. Therefore, the data analysis described in the next chapter only briefly touch on travel time residuals.

In the context of sampling the ULVZ surface the lateral resolution of it should be discussed which is defined by the effective Fresnel zone. This is an elliptic area in case of layered medium where all features inside that zone contribute to the reflection energy of the Fresnel ray at the receiver. Hence, features within the Fresnel zone cannot be resolved. A typical explosion source and also PcP impulses show a dominant frequency around 1 Hz which gives an effective Fresnel zone of about 170 km by 110 km for an incidence angle of 30° at the CMB. The larger the incidence angle, the larger the effective Fresnel zone and the smaller the resolution of a basal layer. Essentially, the Fresnel zone is rather a circle than an ellipse within the steep-angle area. The resolution also increases for higher signal frequencies. All tested topography models have much larger dimensions than such a Fresnel zone up to 40°. It should be noted that the true resolution limits are much more complicated if the interface has undulations.

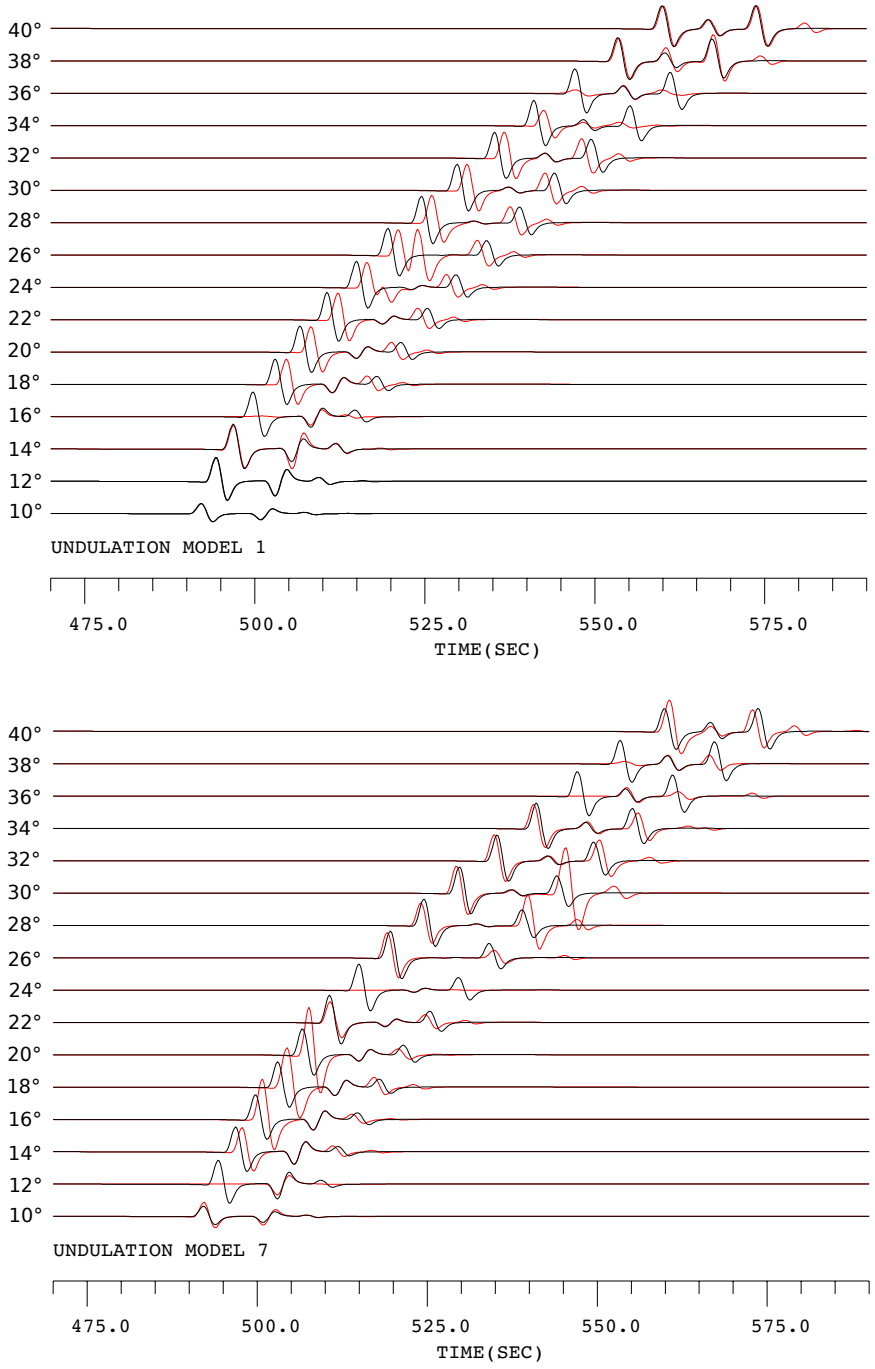

Fig. 3.30: Velocity proportional synthetic seismograms for the undulation models 1 (top) and 7 (bottom). Time scale refers to the absolute travel time since no velocity reduction were used. Black traces show the flat ULVZ of model -10%-30%+30% for a 55 km thick layer. The solutions using a wavelet of 4 s are shown. Red seismograms mark the results using the topographies. Note the strong waveform distortions for model 1 at 24° and 26° as well as the amplified postcursor at 30° for model 7.

Chapter 4

Data

The practical part of this thesis includes the analysis of two different datasets - nuclear explosions and deep earthquakes. Both of event types have assets and drawbacks. Deep earthquakes are less frequently than shallow events and spatially restricted to subduction zones. An event determination involves a large uncertainty of the depth and thus also the epicentre coordinates cannot be located exactly. Another uncertainty follow from the focal mechanism and the derived radiation pattern. This might influence the PcP/P amplitude ratio since the measured ratio from the seismograms have to be corrected for the radiation pattern to make them comparable with other events. This potential error larger, the closer the rays emerge at the nodal plane. For this reason moment tensor solutions should be always obtained from the same agency to make sure that the same inversion technique is used. Otherwise deep earthquakes generate a higher stress drop and smaller source dimensions for a discrete magnitude compared to shallow events. Thus, theoretically more high-frequency and simpler impulse forms are radiated.
The usage of nuclear explosions is interesting since they often cover non tectonic active regions. Smaller and simple source processes and dimensions are expected as well as short-period and coherent PcP waveforms [Bormann, 2009]. A correction for the radiation pattern is not necessary. In correlation with earthquakes the location of man-made explosion sources is more accurate. However, because of the sources are located within the uppermost 1000 m complex wave trains occur due to multiple crustal interactions.
Since the PcP impulse has rather weak amplitudes (cf. 3.4) it is expedient to use seismic arrays to enhance the signal. The Gräfenberg (GRF) and NORSAR array in central Europe allows the study of nuclear explosions as well as deep earthquakes within an epicentral distance range of about 45° and from different directions. In the following all test and event sites used are briefly described. The exact location of the events can be taken from figures 4.2 and 4.19. Further, all source parameters are summarised in tables 4.1 and 4.2. In case of the explosions the event details were obtained from DTRA Verification Database [2012] which is on the behalf of the U.S. Department of Defense. This database provides information of all kinds of worldwide explosions. Common event bulletins as ISC International Seismological Centre [2010] and the PDE (Preliminary Determination of Epicentres) [United States Geological Survey, 2010] do not include all explosion events and give no correct depth locations (all depth information are set to zero).
The selection of appropriate earthquakes are based on the event catalogue of ISC where the obtained events were compared to the PDE solutions. At this, the ISC bulletin have proven to be more completely. All moment tensor solutions or strike, dip and rake information were obtained from the Global Centroid Moment Tensor Catalogue (CMT) [Ekström, G. and Nettles, M., 2012] from which the correction for the radiation pattern can be calculated.

The analysis of the data is based on beamforming processes. Prior to this a ground motion restitution concerning the instrument response was applied to the velocity proportional vertical seismograms. Slowness vespagrams in time domain have been created for a sufficient large slowness range to determine the maximum P and PcP amplitudes, respectively. This means that the beamforming process described in section 2.4 is repeated for several slowness values and a discrete BAZ. Hence, each beam trace corresponds to a distinct slowness value and P and PcP were separately measured from that beam (slowness) trace which shows the largest absolute amplitude - independent from the theoretical slowness value. Above all for PcP a large scattering of the determined slowness values arise from this process for different events from the same region. This might be a result of the poor slowness resolution due to the array geometry and/or because of a mislocation as a consequence of the receiver site (see sections 4.1.1 and 2.4 for details). In addition, slowness deviations can occur for waves which not propagate along great circle paths or are influenced by scattering effects. Afterwards, the determined 'raw' PcP/P scaling has been corrected for the radiation pattern. For that purpose, using the strike, dip and rake parameters from CMT, a normalised radiation pattern was calculated. With suitable take-off angles for P and PcP (given by *TauP* [Crotwell et al., 1999]) the proper 'focal mechanism' PcP/P scaling is obtained which is simply called Rad-Pat in table 7. Finally, the 'raw' amplitude scaling is divided by the 'focal mechanism' PcP/P scaling.
Similar to the synthetic study the PcP scaling has been analysed. To avoid misunderstandings the notation follow from the relation:

$$\frac{PcP^{mod}}{PcP^{smooth}} \hat{=} \frac{PcP^{data}}{PcP^{smooth}} := \frac{\left(\frac{PcP}{P}\right)^{data}}{\left(\frac{PcP}{P}\right)^{smooth}}$$

During the Cold War hundreds of nuclear explosions were conducted in the former Soviet Union. In this study the test sites at Semipalatinsk and Novaya Zemlya were investigated as well as the Peaceful Nuclear Explosions (PNEs) close to the Caspian Sea.
The PNEs get the name from their non-military application. The priority aim was the exploration of oil and gas, the creation of storage cavities and mapping of the crustal and upper mantle structure below the site. Between January 1965 and September 1988 122 of such explosions were triggered over a wide range of the Soviet Union [Sultanov et al., 1999]. For the purpose of this study only the strongest events are useful, most of them located to the north of the Caspian Sea. This source site belongs to the region of the North Caspian Basin that consists of huge salt sediment complexes up to 23 km thick [Große, 1989]. A typical depth for the PNE is about 1000 m whereby simultaneously two or three devices were detonated in the same borehole. The maximum body wave magnitude m_b reaches 6.0.
The nuclear explosion test site at Novaya Zemlya, an archipelago to the north of Russia between Barents and Kara Sea, is divided into two subregions: Krasino and Matchokin Shar. The analysis is restricted to the latter site because of numerous strong body wave magnitudes up to 6.0. 33 underground explosions were conducted between September 1964 and October 1990. The test site is located close to the river Matchokin Shar, which divides Novaya Zemlya into two islands. Each detonation took place in adits (a tunnel with only one opening) mined into the frozen bedrock, consisting of hard metamorphosed shales and sandstones with significant topography. The surface elevation ranges from 100 to 400 m above the study region. All source depth

information are highly uncertain since they have been estimated by the official yield range of 0.001 to 150 kt at which in turn a discrete yield value was approximated from the body wave magnitude. Furthermore, mostly multiple devices were applied, which also affect the yield estimation. In case of the events used the mean source depth is about 350 to 500 m [Khalturin et al., 2005; DTRA Verification Database, 2012].
Most of the Soviet underground nuclear explosions were conducted at the Semipalatinsk test site between 1949 and 1989 with a total of 363 events. The events analysed belong to today's East Kazakhstan and are located northeast of Lake Balkhash. This test site is divided into four major subregions: Balapan, Degelen, Murzhik and Ground Zero Technical Area, where only events from the first two sites were investigated. The majority of the explosions occurred in boreholes at Balapan (since 1965) located inside a rather flat terrain of siliceous sandstone. The Degelen subregion is completely different from the further eastern situated Balapan since the events took place in horizontal excavations similar to Novaya Zemlya. Moreover the rock massif of the Degelen Mountain complex is permeated by tectonic faults and extensive fractures. Unfortunately, a detailed information about all device depths is not available. From some individual explosion descriptions a mean source depth of about 300 m can be assumed [Adushkin and Leith, 2001]. However other authors as Yang et al. [year unknown] set all depths to zero.

Deep earthquakes below 100 km and with larger magnitudes than 5.0 are infrequent in central Europe. As a consequence of the convergence of African and Eurasian plate a few very deep earthquakes occur in southern Europe (above all in Spain) where an exact explanation remains outstanding. One event in Spain and four events north of Sicily were considered. The Spain event is exceptionally and very rare with its depth at about 620 km and a moment magnitude of 6.3. Another, very deep events up to 500 km, took place close to Naples. Because of the poor SNR and the very low reflection coefficient of PcP these events are useless for the analysis in this thesis. Furthermore, intermediate deep intracontinental earthquakes occur in Romania, in the southeast bend of the Carpathian arc. The Sicily and Romania events are then only analysed using the GRF array.
The Hindu Kush region shows great promise for probing the CMB since a couple of strong earthquakes occur below 200 km and are located within an area of 77 km by 37 km. In view of a preferably coherent sampling of the CMB only events with similar epicentre, depth and focal mechanism were selected. The deep earthquakes in the region of the Afghanistan-Pakistan border line occur as a result of the convergence of the Eurasian and Indian plate. In this process a part of the Eurasian plate is subducted which allows the generation of deep earthquakes although they occur at a continent-continent collision.

Figure 4.1 gives an overview of the main phases which are expected in case of shallow nuclear explosions and deep earthquakes with mean depths located at 0.5 km and 200 km, respectively. The global model ak135 [Kennett et al., 1995] and a velocity reduction of 12.2 km/s were applied using *TauP* [Crotwell et al., 1999]. The shallow source causes the generation of numerous phases due to crustal multiple interactions. For the parameters used Pn (refraction at the Moho) is the first arrival up to a distance of 20° where the true distance depends on the thickness of the crust. Beyond that range P becomes the first onset with the triplications around 17° and 22° resultant from the large velocity gradients at 410 km and 660 km depth. The depth phases of P, sP and pP, arrive almost at the same time for such shallow sources and probably cause complex wave trains above all within the triplication range. For distances up to 30° the surface reflection PnPn

arrives after P and is called PP beyond that location. At this distance triplications are created which are visible around 34° and 44°. These second PP triplication interferes with PcP. Within the near-distance range up to 17° and 18° the crustal surface reflections PbPb and PgPg can be observed, respectively. Pb is the refraction at the Conrad discontinuity and Pg is the direct wave propagating through the upper crust. The direct S wave with its triplications crosses PcP at 22°. PcP itself is also superimposed by its depth phases pPcP and sPcP.
A deep source seems to simplify a PcP study since the depth phases are well separated and no multiple crustal reflections occur. However the overlap with the PP triplication remains which will influence the investigation of some events.

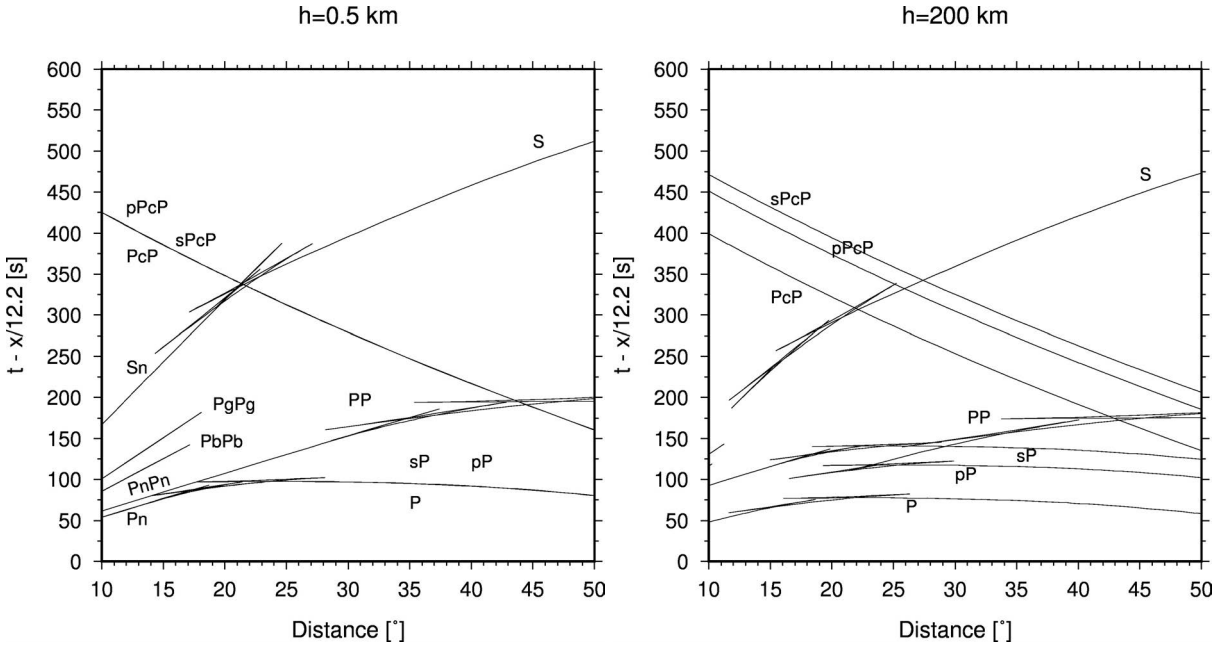

Fig. 4.1: Travel time curves for a depth of 0.5 km and 200 km. A velocity reduction of 12.2 km/s was applied using the global model ak135 [Kennett et al., 1995].

Table 4.1: Event list for **earthquakes**

No.	Event	Lat	Lon	Depth	Mw	Region
1	2011-May-14 21:07:22	36.4090	70.7480	207.3	6.0	Hindu Kush
2	2009-Oct-29 17:44:32	36.3822	70.7684	213.9	6.2	Hindu Kush
3	2005-Jul-23 14:40:23	36.4116	70.7255	203.2	5.5	Hindu Kush
4	2004-Aug-10 01:47:31	36.4177	70.7630	206.5	6.0	Hindu Kush
5	2002-Mar-03 12:08:18	36.4960	70.5170	208.9	7.3	Hindu Kush
6[b]	1993-Aug-09 11:38:31	36.4307	70.7223	215.5	6.3	Hindu Kush
7[b]	1991-Jul-14 09:09:12	36.4196	71.1455	218.9	6.6	Hindu Kush
8[b]	1990-Jul-13 14:20:42	36.4504	70.7917	202.8	6.3	Hindu Kush
9[a,b]	1987-May-05 15:40:48	36.22	70.55	207.6	6.2	Hindu Kush
10[b]	1986-Mar-11 23:07:38	36.4805	70.6429	204.4	5.5	Hindu Kush
11[c]	2009-Jan-03 20:23:20	36.4572	70.7439	209.0	6.6	Hindu Kush
12[c]	2007-Apr-03 03:35:06	36.5173	70.6851	213.0	6.2	Hindu Kush
13[c]	2005-Dec-12 21:47:44	36.4059	71.1035	223.9	6.5	Hindu Kush
14[c]	2001-Feb-25 02:22:00	36.42	70.88	202.0	6.1	Hindu Kush
15	2010-Apr-11 22:08:11	37.0866	-3.5350	618.2	6.3	Spain
16	2006-Oct-26 14:28:38	38.7612	15.3956	219.2	5.8	Sicily
17	2004-May-05 13:39:42	38.5470	14.7922	228.6	5.5	Sicily
18	1998-May-18 17:19:05	39.2955	15.1111	287.5	5.5	Sicily
19	1994-Jan-05 13:24:11	39.1634	15.1770	290.5	5.8	Sicily
20	2005-May-14 01:53:20	45.6888	26.4850	142.0	5.2	Romania
21	2001-May-24 17:34:01	45.6900	26.4190	142.4	5.2	Romania
22[b]	1999-Apr-28 08:47:55	45.4850	26.2190	150.2	5.4	Romania
23[b]	1986-Aug-30 21:28:35	45.5373	26.3138	137.0	7.2	Romania

[a] Event neither included in ISC nor in PDE

[b] Not available by NORSAR

[c] Only used for NORSAR study

Table 4.2: Event list for nuclear **explosions**

No.	Event	Lat	Lon	Depth	mb	Region	Sub-Site
1	1978-Sep-15 02:37:00	49.9283	78.8617	0.3	6.0	Semipalatinsk	Balapan
2	1985-Jun-15 00:57:03	49.9086	78.8428	0.3	6.1	Semipalatinsk	Balapan
3	1988-May-04 00:57:09	49.9494	78.7503	0.3	6.1	Semipalatinsk	Balapan
4	1988-Sep-14 04:00:00	49.8778	78.8231	0.3	6.1	Semipalatinsk	Balapan
5	1987-Jun-20 00:53:07	49.9367	78.7464	0.3	6.1	Semipalatinsk	Balapan
6	1982-Dec-05 03:37:15	49.9183	78.8867	0.3	6.1	Semipalatinsk	Balapan
7	1982-Jul-04 01:17:17	49.9586	78.8117	0.3	6.1	Semipalatinsk	Balapan
8	1984-May-26 03:13:15	49.9789	79.0056	0.3	6.1	Semipalatinsk	Balapan
9	1987-Apr-03 01:17:10	49.9181	78.7803	0.3	6.2	Semipalatinsk	Balapan
10	1984-Jul-14 01:09:13	49.9094	78.8772	0.3	6.2	Semipalatinsk	Balapan
11	1984-Oct-27 01:50:13	49.9147	78.9281	0.3	6.2	Semipalatinsk	Balapan
12	1982-Apr-25 03:23:08	49.9183	78.8867	0.3	6.1	Semipalatinsk	Balapan
13	1983-Oct-26 01:55:07	49.9125	78.8217	0.3	6.1	Semipalatinsk	Balapan
14	1987-Apr-03 01:17:12	49.7539	78.144	0.3	6.2	Semipalatinsk	Degelen
15	1987-Jul-17 01:17:09	49.7758	78.0197	0.3	5.8	Semipalatinsk	Degelen
16	1978-Jul-28 02:47:00	49.755	78.145	0.3	5.7	Semipalatinsk	Degelen
17	1984-Apr-15 03:17:11	49.7606	78.0892	0.3	5.7	Semipalatinsk	Degelen
18	1987-May-06 04:02:08	49.7758	78.0122	0.3	5.6	Semipalatinsk	Degelen
19	1981-Oct-01 12:14:59	73.3148	54.7933	0.489	6.0	Novaya Zemlya	Matochkin
20	1983-Aug-18 16:10:00	73.3494	54.9798	0.441	5.9	Novaya Zemlya	Matochkin
21	1983-Sep-25 13:10:00	73.3234	54.5468	0.398	5.8	Novaya Zemlya	Matochkin
22	1987-Aug-02 02:00:02	73.3393	54.5917	0.398	5.8	Novaya Zemlya	Matochkin
23	1988-Dec-04 05:19:55	73.3614	55.0068	0.441	5.9	Novaya Zemlya	Matochkin
24	1984-Oct-25 06:30:00	73.3504	54.9958	0.398	5.8	Novaya Zemlya	Matochkin
25	1990-Oct-24 14:58:00	73.3264	54.7628	0.358	5.7	Novaya Zemlya	Matochkin
26	1979-Oct-18 07:10:00	73.3241	54.7541	0.398	5.8	Novaya Zemlya	Matochkin
27	1979-Sep-24 03:30:00	73.3428	54.6873	0.358	5.7	Novaya Zemlya	Matochkin
28*	1978-Oct-17 04:59:59	47.85	48.12	1.00	5.8	PNE	Azgir A-7
29*	1979-Jan-17 07:59:58	47.92	48.12	0.965	6.0	PNE	Azgir A-8
30**	1979-Jul-14 04:59:58	47.88	48.12	0.916	5.6	PNE	Azgir A-11
31*	1979-Oct-24 05:59:59	47.85	48.14	0.948	5.8	PNE	Azgir A-10

* Simultaneous detonation of 2 devices in the same hole
** Simultaneous detonation of 3 devices in the same hole

4.1 Gräfenberg Array

4.1.1 Location of Events and the Array

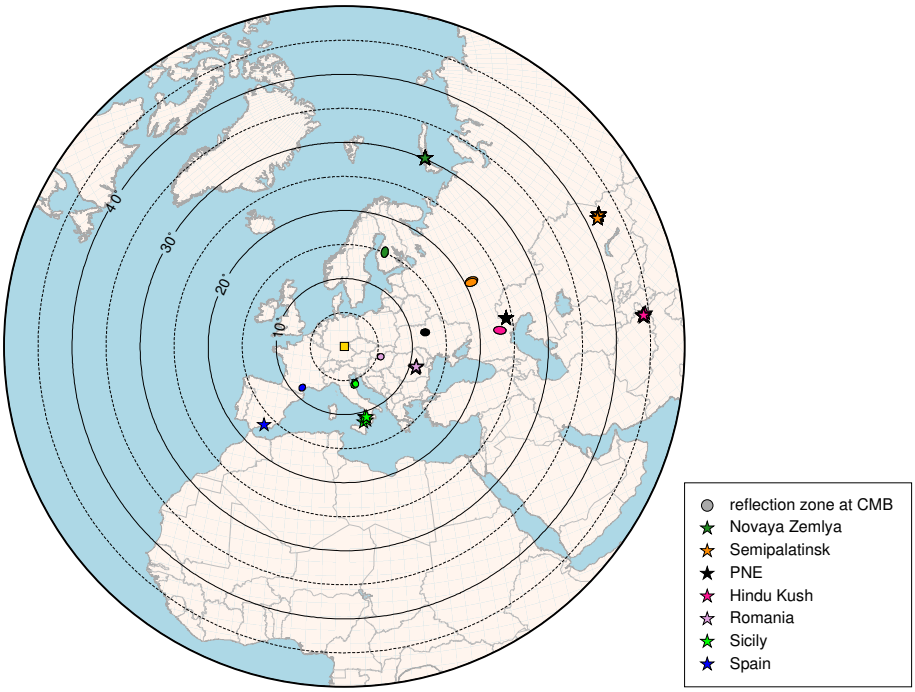

Fig. 4.2: Map of all analysed events respect to the Gräfenberg array which is located in the centre of the plot and marked as golden square. Shown is an azimuthal equidistant projection up to 50°. Earthquakes and nuclear explosions are marked as stars. The projected ellipses correspond to the appropriate effective Fresnel zones at the CMB.

The Gräfenberg array is located on the Franconian Jura in Bavaria, Germany (indicated as a yellow square in figure 4.2). Since January 1980 it consists of 13 broad-band velocity proportional instruments. The installation of the first three stations took place in January 1975. All 3-component Streckeisen STS-1 were replaced by STS-2 instruments in 2006. A sampling rate of 20 Hz was chosen for the used data, which are available from the Seismological Central Observatory [2012]. A crucial attribute of the GRF array is the systematic mislocation of P-waves respect to slowness and azimuth values. Krüger and Weber [1992] have shown an P-slowness reduction especially for events from the northeast. Also the corresponding BAZ reveal notable mislocations up to +15° respect to a theoretical BAZ of about 90°. Hence, large mislocations can be expected for the events from Novaya Zemlya, Semipalatinsk, Hindu Kush and Caspian Sea. The derived mislocation vectors from their study were compared to a f-k analysis and an event location determination in time domain as far as possible. In several cases the results are ambiguous and finally the slowness values from the event location in the time domain were used since exact mislocation vectors are not available for all required slowness/direction combinations. In contrast, for southerly events a higher P-slowness is expectable, though the data coverage is poor in that region. The reason for those effects could be a consequence of a NNE dipping low-velocity sedimentary wedge below the receiver site where the layer thickness increases towards the north-northeast. However, there is still no evidence that such a geological structure is in

fact able to produce slowness deviations up to 1.5 s/° as can be observed for some Semipalatinsk events.
Another interesting feature is marked by travel time and amplitude anomalies among the different GRF stations [Weber, 1994b]. Waves arriving with a higher slowness than predicted show smaller amplitudes and vice versa. This is not only a frequency- and direction-dependent effect but also sensitive to the regional geology at the receiver site (after the removal of the station averages). The anomalies are most pronounced on short-period ranges for events from the northeast and southeast. In addition, the GRF array can be divided into three clusters respect to the A, B and C stations (see figure 2.3). Amplitude and travel time residuals are largest for the southernmost stations GRB5 and GRC1-GRC4. The cause for that kinematic and dynamic anomalies is in agreement with the explanation of the previous study by Krüger and Weber [1992]. However, for the purpose of this study mostly beamed broad-band data are considered whereby such effects are averaged. A short note on those station related amplitude residuals will be given for the Hindu Kush events.
Regarding to the resolution of the array, poor slowness resolution can be assumed for the Semipalatinsk, Hindu Kush and PNE events. Though the analysis of the BAZ should be very well for that directions. On the contrary, the deep earthquakes from southern Europe should show best slowness and worse BAZ resolution (see section 2.4 for details).
Figure 4.2 illustrates all events used on an equidistant azimuthal map projection. The black circles show the epicentral distances in steps of 5° respect to GRF. The ellipses are the surface projections of the reflection zones of PcP at the CMB in the size of the appropriate effective Fresnel zones which become larger for increasing distances.

4.1.2 Analysis of Nuclear Explosions

Nuclear explosions show a typical dominant source period of about 1 s. For a better understanding the explosion data have been filtered using a short-period bandpass filter between 0.5 and 1.5 Hz and third order. Moreover a high-pass filter of 4 s (third order) was applied to remove the oceanic micro waves. However, it will be shown that the PcP impulse can be best seen on broad-band data. Hence, the detailed amplitude study has been done on broad-band seismograms. Figure 4.3 illustrates how the PcP impulse looks like after the application of a high-pass filter of 4 s and a short-period band-pass filter of 0.5-1.5 Hz. The velocity proportional and attenuated synthetic using a 1 Hz wavelet was chosen at 40° distance. Note that the time scale refers to a velocity reduction of 12.2 km/s and a time reduction of 20 s.

4.1.2.1 PNE (Caspian Sea)

As mentioned above the PNE events are distributed over wide regions of the former Soviet Union. Though, a reliable study of the CMB character requires several events at the same site to make a quantitative assumption about PcP amplitudes and waveforms. After the investigation of events with differing magnitude it became apparent that a minimum m_b of 5.5 is needed to distinct PcP clearly from the noise level. Unfortunately, these preconditions restrict the suitable data to only 4 events (see table 4.2). The investigated data are situated at the Azgir test site where the Azgir A-9 event could not be used because of the recording by only three stations. It should be noted that two and three devices were used in the same borehole. However, the results are unambiguous and provide nonetheless a sufficient assumption about the CMB below Kiev with

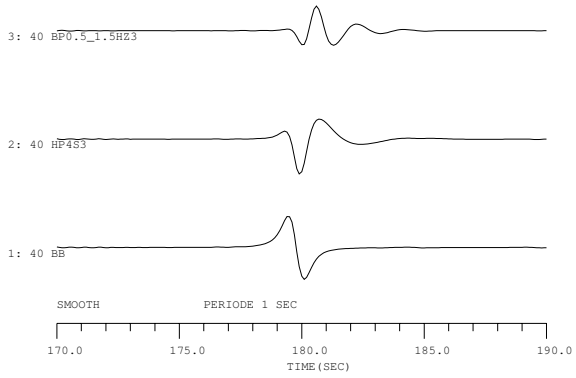

Fig. 4.3: Smooth velocity proportional and attenuated PcP impuls at 40° using a source period of 1 sec. The traces show the 'broad-band' PcP results as well as high-pass filtering of 4 sec and band-pass filtering with 0.5-1.5 Hz. Time scale refers to a velocity reduction of 12.2 km/s and a time reduction of 20 s.

an effective Fresnel zone of 110 km by 140 km.
The mean distance to Gräfenberg is 24.2° with an BAZ of about 80°. This is exactly the range for triplications from the upper mantle. In combination with a source depth of about 1 km a highly complex P wave train is generated with nine main phases that arrive within a time window of 2.5 s, i. e. the direct P wave, its depth phases pP and sP as well as the two triplication phases and their depth phases, respectively.

Große [1989] has shown that the first arrivals of the Azgir events correlate with the refracted wave below the 410 km discontinuity. This can be determined from the slowness values which are different from the direct wave and refractions from the 660 km discontinuity. That assumption has been checked and is in agreement with the previous results.
For the vespagrams a BAZ of 85° has been applied, respectively, according to the mislocation at the GRF array. The theoretical P-slowness (u_P) is 9.1 s/° and 2.1 s/° for PcP (u_{PcP}). The obtained maximum amplitudes yield a slowness deviation of +0.1/-0.7 s/° for P and +0.5/-0.7 s/° for PcP. Figure 4.4 shows the best beam results for each event from which the amplitudes were measured. The PcP beams (black lines) are underlaid by the P beams (red lines) to emphasise the coherency of these phases. Each trace is normalised to its maximum amplitude within the displayed time window. The uppermost trace shows the summed signals. Explosion sources always induce a positive first onset of P due to the radially emitted compressional wave. Thus, in case of the PNE events shown this first amplitude is fairly weak and the following negative peak is much more pronounced accompanying by a second large positive amplitude. This polarisation pattern is also true for PcP. The overlay of the two phases indicates that the anomalous waveform results from the sophisticated P wave train. The correlation of P and PcP can be seen even better on the bandpass filtered data, using a butterworth filter between 0.5 - 1.5 Hz of third order, on the bottom seismogram section. Beside the event on trace 4, where only 5 stations are available, the signal-noise-ratio (SNR) is fairly good and the waveform coherence of P and PcP is very high. Note that the polarity of that short-period filtered signal is almost opposite to the theoretical results of figure 4.3 because of the large negative peak.
Considering the amplitude ratios, the measurements of PcP/P reveal a ratio of about 0.05, both for the broad-band data and the short-period filtered recordings. This is in good agreement with the global model as can be seen in figure 4.18. The standard deviation is small and even smaller

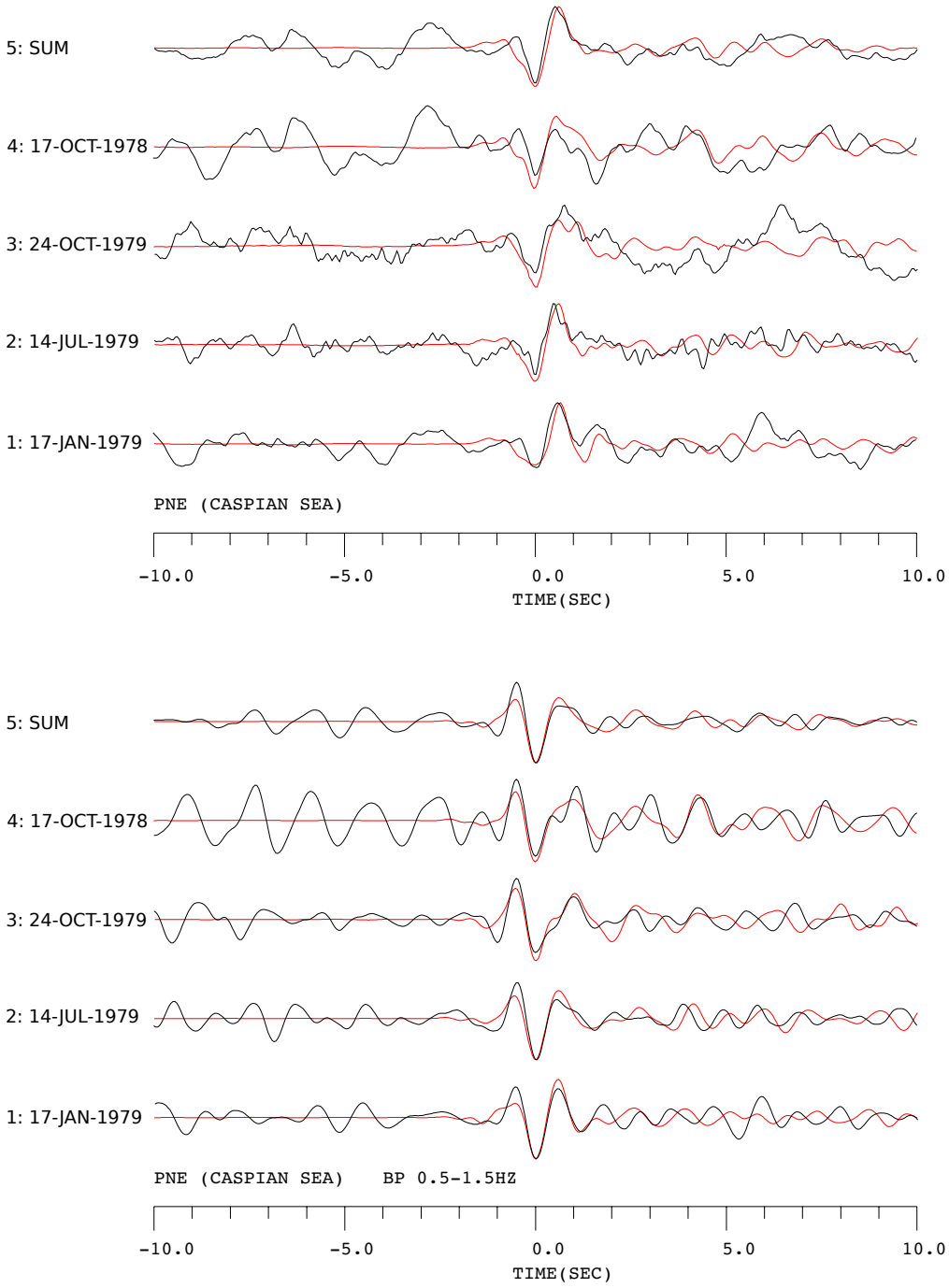

Fig. 4.4: Analysed **PNE** events from the Caspian Sea respect to GRF. Shown are the appropriate P beams (red lines) and PcP beams (black lines). **Top:** Broad-band beams and **bottom:** using a short-period bandpass filter of 0.5 - 1.5 Hz. Traces are aligned on the negative P and PcP peaks, respectively. Each trace is normalised to its maximum amplitude within the displayed time window. The uppermost trace shows the summed signals, respectively. The average distance to Gräfenberg is 24.2° with an BAZ of about 80°.

for frequencies around 1 Hz. The determination of the double-scaled PcP^{data}/PcP^{smooth} ratio gives 0.9, i. e. the measured PcP/P ratio is about 90% of the smooth PcP/P ratio (see figure 4.5). A value of 100% would mean that the observed signal completely fits the conditions of the global model. There is no evidence for a precursor. As a consequence of these results a thick ULVZ below Kiev cannot be detected. It was shown in section 3.1 that a very thin low-velocity anomaly of about 5 km and with only little V_P and density changes of 5% could produce such minor amplitude reductions: A PcP/P scaling cannot indicate an anomaly at this distance range but the PcP^{mod}/PcP^{smooth} relation is able to denote a very thin and moderate ULVZ with a first-order discontinuity. Otherwise, the modelled findings provide an additional interpretation of the data. A thin, mushy CMB - rather a mantle-side Core-Mantle Transition Zone (CMTZ) - may also generate small PcP reductions.
Naturally, also other features as little undulations, anisotropy or inhomogeneities could explain these slight PcP amplitude reductions. Moreover, the CMB itself seems to be fairly flat without an detectable topography which would be seen on the short-period data since larger undulations are sensitive to high-frequency signals [Kampfmann and Müller, 1989].

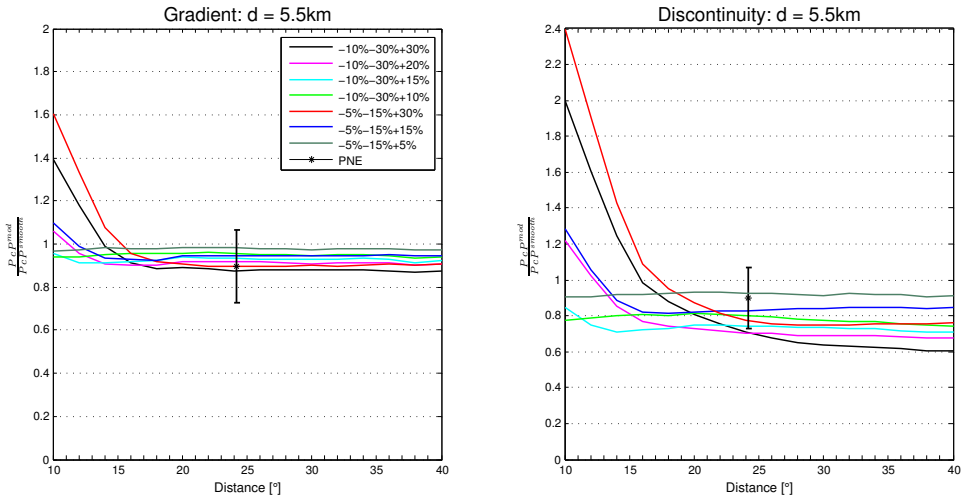

Fig. 4.5: The PNE results are overlaid by the synthetic modelling for a 5.5 km thick low-velocity anomaly. **Left:** A gradient, very thin anomaly may rather refer to a mantle-side Core-Mantle Transition Zone (CMTZ) - independent from the velocity and density contrasts. **Right:** The first-order discontinuity synthetics can also explain the data in case of a moderate ULVZ with -5%-15%+5% contrasts.

4.1.2.2 Novaya Zemlya

Nine events from the Matchokin Shar test site show a sufficient large magnitude between 5.7 and 6.0. Even larger events occurred, but prior to the GRF installation. The mean distance to Gräfenberg is 30.2° with an BAZ of about 23.3°. That distance is uncomplicated since it is beyond the triplication range and no interferences with other phases as S and PP occur. The CMB is probed below south-west Finland with an effective Fresnel zone of 110 km by 170 km. A BAZ of 20° was used for the beamforming processes. The beam traces with their maximum P (red) and PcP (black) amplitude are summarised in figure 4.6. The traces are aligned on the positive P and PcP peaks, respectively. All observed PcP slownesses are lower than the predicted value of 2.6 s/°. This is also true for u_P of 8.8 s/°. All PcP beams reveal a second smaller negative onset 1.1 s after PcP which is also well pronounced on the summed trace. The appropriate P beams

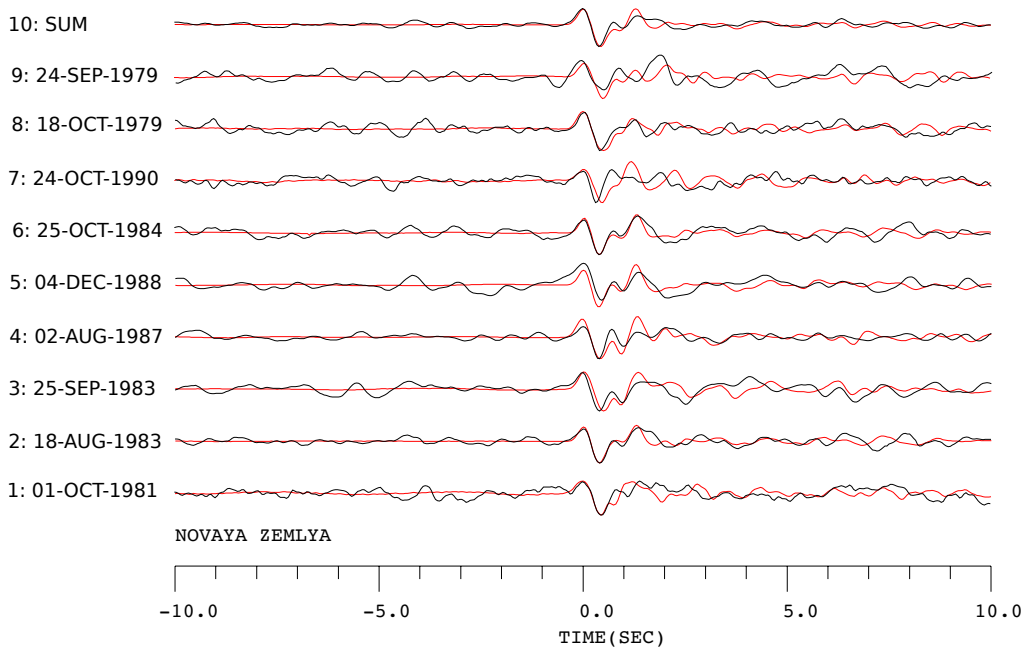

Fig. 4.6: Broad-band PcP beams (black lines) of all analysed **Novaya Zemlya** events are underlaid by the appropriate P beams (red lines). The mean distance to Gräfenberg is 30.2° with an BAZ of about 23.3°. Traces are aligned on the positive P and PcP peaks, respectively. Each trace is normalised to its maximum amplitude within the displayed time window. The uppermost trace shows the summed signals. Obviously, the additional negative peak respect to PcP is caused by the complex P impulse which is probably a result of the source site structure.

have been overlain. Each trace is normalised to its maximum amplitude within the displayed time window. Obviously, the additional negative peak respect to PcP is caused by the complex P impulse which is probably a result of the source site structure. As mentioned above the test site is situated within a mountain chain which is potentially an extension of the Ural Mountains [DTRA Verification Database, 2012]. Due to the source depth of about 400 m and the interaction with the notable topography strong crustal reverberations occur.
Amplitude measurements related to PcP/P yield a mean ratio of about 0.20 for the broad-band data and 0.21 for a short-period range of 0.5 - 1.5 Hz. Thus no high-frequency-dependent effect can be detected although the standard deviation is much larger than for the PNE results (see figure 4.18). The amplitude ratio is clearly raised compared with the global model which may indicate a focussing effect due to a CMB topography. The mean deviation amounts to +90%. Furthermore, also the PcP^{data}/PcP^{smooth} relation potentially shows a CMB undulation since that relation is on average 86% higher than for the smooth model. These potential focussing effects are larger than by Kampfmann and Müller [1989] predicted. The results from this study may indicate a stronger topography at the CMB.

4.1.2.3 Semipalatinsk (Kazakhstan)

The Semipalatinsk test site provides more suitable data since also in the 1980s many large explosions were conducted above all at the Balapan subregion. The mean distance towards GRF is 42.3° with an BAZ of 62.7°. No significant azimuth mislocation could be observed and a BAZ of 62° has been applied for the beamforming. In addition the BAZ resolution should be the best from that direction. Thus this is not a trivial distance range because PP and its triplication

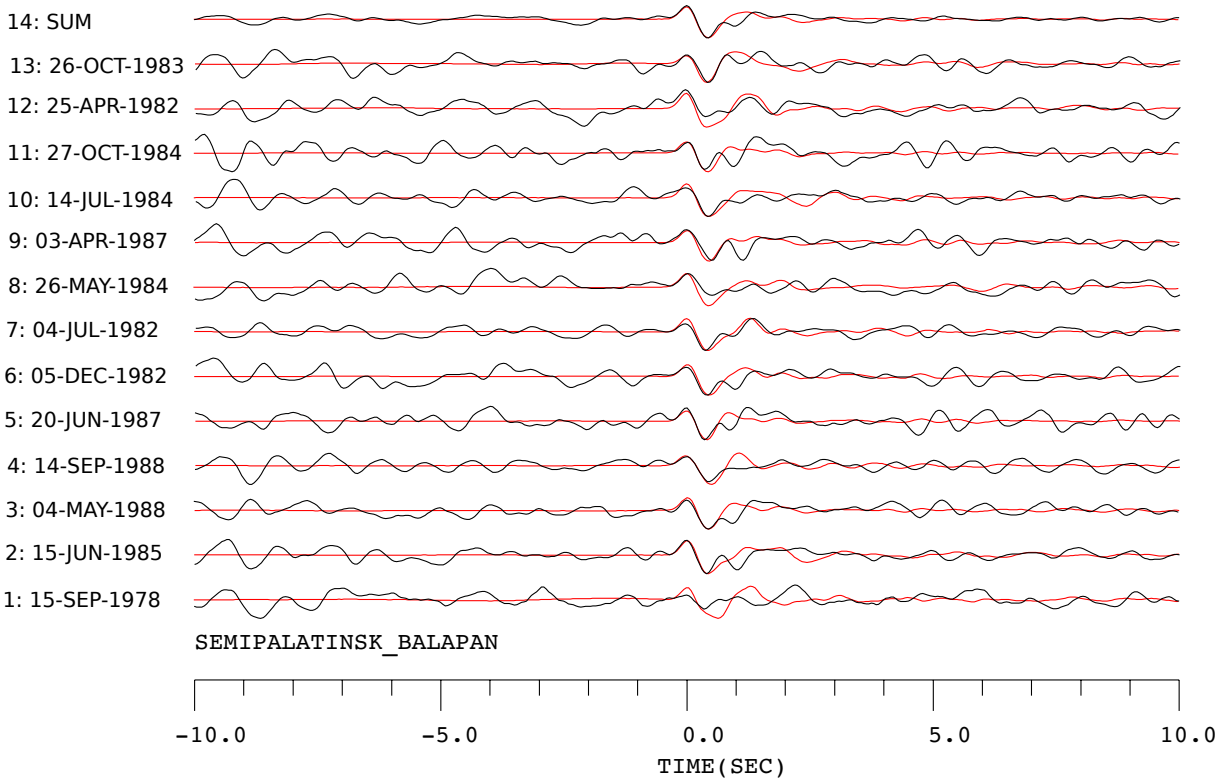

Fig. 4.7: All analysed PcP beams (black lines) underlaid by the appropriate P beams (red lines) for the Balapan subregion of **Semipalatinsk**. The traces are aligned on the positive P and PcP peaks, respectively. Each trace is normalised to its maximum amplitude within the displayed time window. The uppermost trace shows the summed signals. It can be seen very clearly that the second negative peak, accompanying PcP, is not caused by P. The P impulse is very simple for all events and no structural effects occur. Hence, the second negative amplitude is most likely generated by a CMB feature.

phases arrives only about 10 s before PcP and a long wave train can be expected. However with the aim of vespagrams a separation of PcP and PP is possible since u_{PcP} is about 3.3 s/° and the predicted PP slownesses range from 9.5 s/° to 10.8 s/°. The observed PcP slowness values are lowered to about 2.6 (-0.4/+0.8) s/°. An unusual large slowness reduction is obtained for P with a measured slowness of 6.6 (-0.2/+0.4) s/° respect to a theoretical value of 8.1 s/° as it was already shown by Krüger and Weber [1992].

At first the coherence between the P and PcP waveforms have been considered which is displayed in figure 4.7. Again the suitable beam results are illustrated for the Balapan site. As has been shown before for the Novaya Zemlya events the PcP impulse is accompanied by a second negative peak (black seismograms). This can be seen very clearly for almost every event and it is also well pronounced on the summed trace. However, in contrast to the previous test site this additional wiggle does not occur with the P impulse, which is fairly simple for the Semipalatinsk events (red seismograms). Hence this seems to be not a source effect but could be generated by a CMB feature. The significant potential postcursors arrive 1 - 1.5 s after PcP.

Figure 4.8 shows only the beamed PcP seismograms for the Balapan site. Again, each trace is normalised to its maximum amplitude within the displayed time window where the time window is larger compared to figure 4.7. The traces are aligned on the positive PcP peak and the pulses are marked with the red shaded area. The complex wave field prior to the PcP impuls refers to PP. For some events a small precursor can be assumed, i. e. traces 1, 2, 3, 6, 7, 11 and 13

indicate a weak PxP about 1.5 s before PcP arrive. However, the signal-to-noise ratio is very poor and for some events there is no evidence of a precursor.
The best example can be seen on trace 2 where also the frequency of PxP fits well the PcP period. A vespagram with the 4th root was created to suppress all signals with other slownesses much more as it can be achieved by the linearly beam process. The 4th root is extracted from each individual trace before the summation and after the summation of the beam trace the 4th power is taken from it. Though the waveform and amplitude information is lost with this method, since it is a nonlinear process, the sign of each phase is kept [Rost and Thomas, 2002]. Therefore this alternative beamforming is only suitable for checking the slowness distribution. For the 1985-Jun-15 event (trace 2) a small precursor with the same slowness as PcP is detectable on those 4th root beams (figure 4.9). In addition the potential postcursor is highly indicative also with the same slowness as PcP. Beside that event weak evidence for PxP can be seen for the events at traces 5 and 11 (see figures 7.1 and 7.2 in the appendix). All other 4th root vespagrams are not able to enhance the slowness resolution in terms of a possible precursor partly because of the overall high noise level.
Additional 5 events were found from the Degelen subregion which are displayed in figure 4.10. Those test site is situated about 100 km southwestern from Balapan whereby an almost identical Fresnel zone at the CMB is obtained. Only one event with a magnitude larger than 6.0 is available using the GRF array. This 1987-Apr-03 event (trace 1) with a m_b of 6.2 shows a huge, clear postcursor in contrast to the other events. In general, the amplitudes of this conduction are much larger than for the others with magnitudes around 5.7. Thus the postcursor on the summed trace is mainly a result of the big explosion and a comparison between these events is rather difficult. A potential precursor can be assumed on trace 2 and 3.

An evaluation of the amplitude ratios yielded more reliable information than the waveform analysis. The average PcP/P ratio for the Balapan test site gives a value of 0.104 and at Degelen an almost identical relation of 0.105. All single amplitude ratios, measured from the absolute P and PcP amplitudes, are listed in table 7.2 in the appendix. Due to the same amplitude ratios and effective Fresnel zones the results of both subregions are summarised in figure 4.11. The synthetic calculations for a ULVZ thickness of 13.5 km are shown using a dominant source frequency of 1 Hz which corresponds to a typical explosion source. The measured Semipalatinsk data are overlain whereby the calculated standard deviation is indicated as orange errorbar. Although the scattering of the observed data is fairly high the mean values are clear reduced compared to the global smooth model and range around the moderate model with -5%-15%+5% contrasts. This is true for all amplitude scalings: PcP/P, PcP^{mod}/PcP^{smooth} and PxP/PcP. The double-scaled PcP relation yields a mean value of 0.65 and PxP/PcP gives about 0.5 whereby only 9 PxP amplitudes could be determined from the data.
Taking all these results into account a moderate, thin ULVZ can be assumed. The first indication results from the well pronounced postcursor which is not generated by any structural reverberations. The PcP/P and PcP^{mod}/PcP^{smooth} ratios provide both same mean amplitude lowering which correlates to -5% V_P, -15% V_S and +5% density. Also the PxP/PcP ratio it consistent with this assumption even if there is no convenient precursor detectable. However, if the assumption about such a ULVZ is true, it is improbable to observe a clear PxP impulse since the synthetic calculations predict always smaller precursors than PcP for such a moderate low-velocity anomaly. In this case a precursor may not be distinguishable from the noise level.

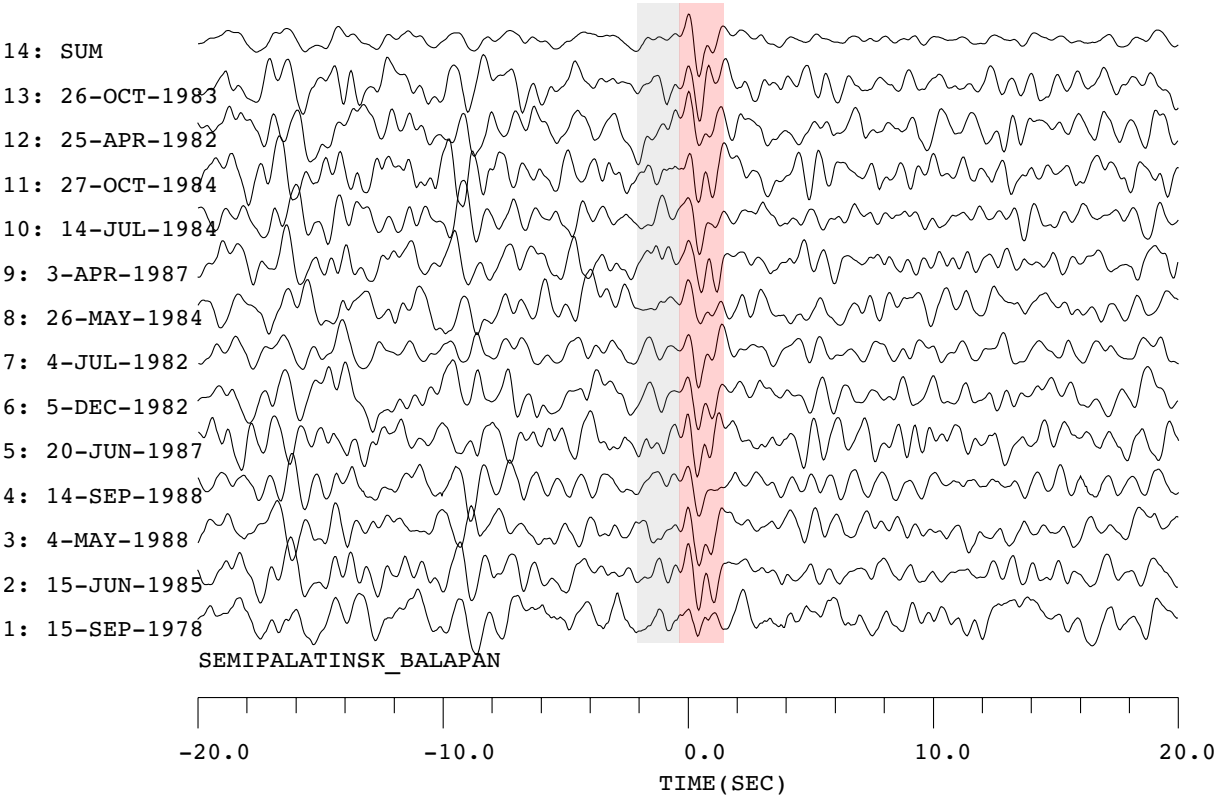

Fig. 4.8: All analysed events of **Semipalatinsk**, at sub-site **Balapan**, for the Gräfenberg array with a mean distance of 42.26° and a BAZ of about 62.7°. Shown are the broad-band optimal beams of each event. The traces are aligned on the positive PcP peak. Each trace is normalised to its maximum amplitude within the displayed time window. The uppermost trace shows the summed PcP signals. Red shaded area indicates the PcP impulse with an accompanying second negative peak which may refer to a postcursor although this amplitude is fairly incoherent for the single events. The PcP pulse itself is rather coherent with respect to frequency and waveform except for trace 1. Only 7 stations have recorded that 1978 event. For some events (traces 1, 2, 3, 6, 7, 11 and 13) a small precursor PxP can be assumed. However on the summed trace no such precursor energy can be seen since the overall SNR is very poor.

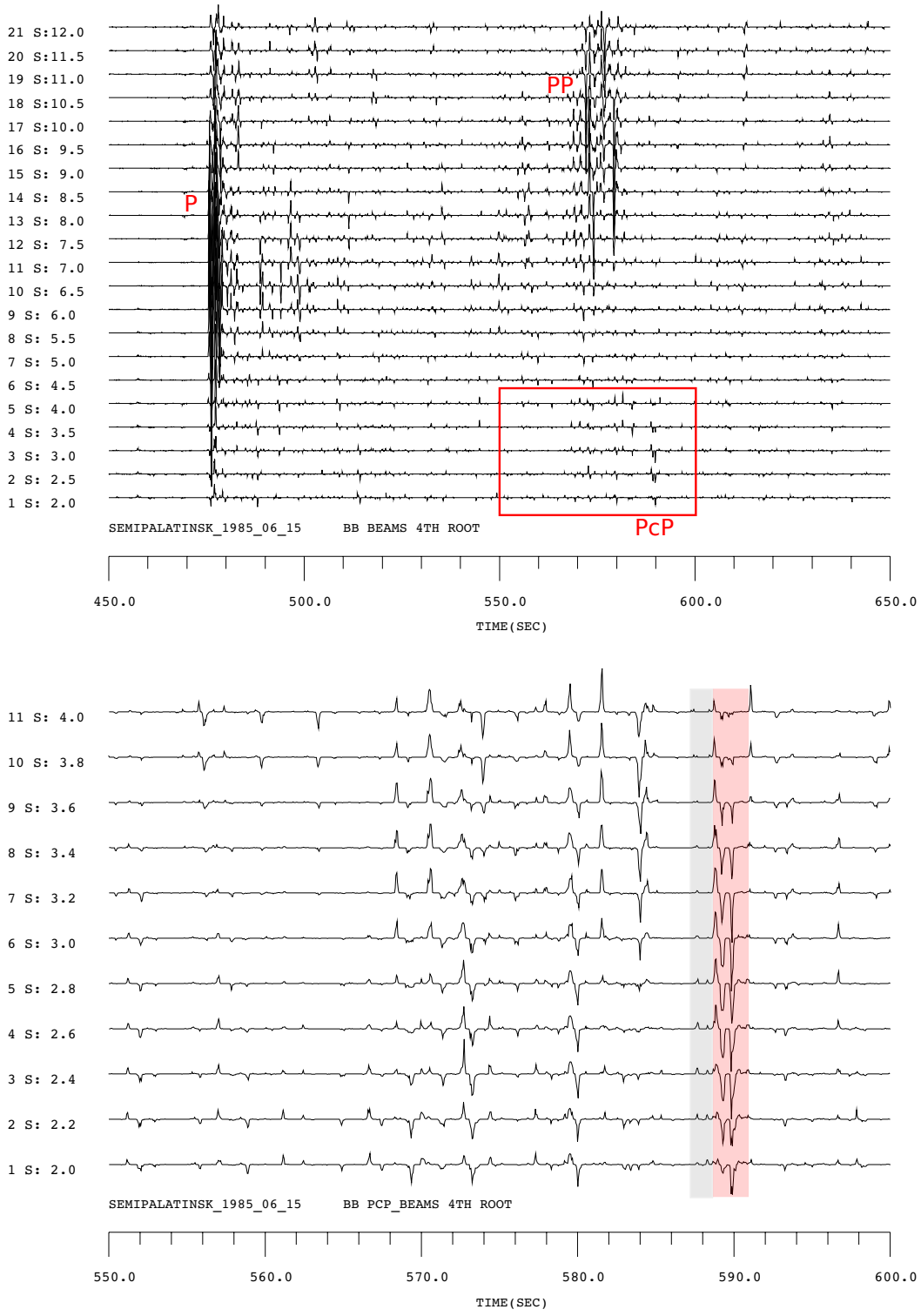

Fig. 4.9: 4th root vespagrams for the 1985-Jun-15 event of **Semipalatinsk**. Upper seismogram section shows the complete relevant slowness range from 2.0 to 12.0 s/° in steps of 0.5 s/°. The wave trains of P, PP and PcP are well resolved and above all the PcP energy is well enhanced. The lower vespagram shows the red marked area in detail for a slowness range from 2.0 to 4.0 s/° in steps of 0.2 s/°. Obviously, the potential precursor (grey shaded area) and postcursor have the same slowness as PcP (red shaded area) with an observed value of 2.6 s/°.

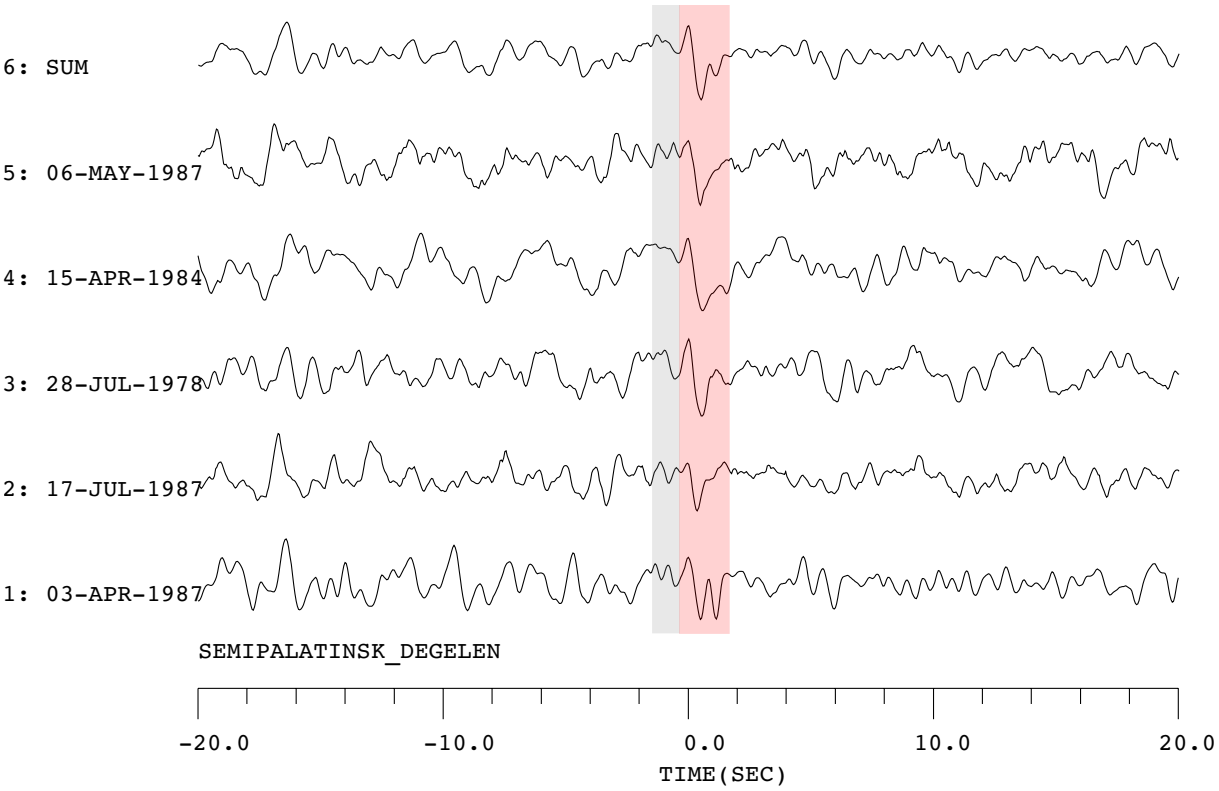

Fig. 4.10: All analysed events of **Semipalatinsk**, sub-site **Degelen**, for the Gräfenberg array with a mean distance of 41.89°. The broad-band traces are aligned on the positive PcP peak. Each trace is normalised to its maximum amplitude within the displayed time window. The uppermost trace shows the summed PcP signals. Red shaded area indicates the PcP impulse. A potential precursor PxP is marked as grey area.

Another evidence arises from the same observed PxP and PcP slowness values as well as the dominant signal frequency. Finally, an assumption about the ULVZ thickness is possible due to the travel time difference of PxP and the postcursor respect to PcP. The measured travel time differences from PxP to PcP as well as PcP to the postcursor amounts up to 1.5 s which can be related to a synthetic thickness of 10 - 13.5 km for a distance at about 42° (cf. figure 3.23). Those low-velocity anomaly would be situated about 600 km ESE of Moscow where the effective Fresnel zones reach about 120 km by 200 km.

Similar to figure 4.3 the PcP impuls of models -5%-15%+5% and -5%-15%+15% with a thickness of 13.5 km were filtered. Figure 4.12 illustrates the application of the same high-pass and band-pass filters at a distance of 40° for the 1 Hz wavelet. At these two examples the precursor is only about 50% of PcP and the travel time difference amounts 1.5 s. As a result the filtered wave trains are complex and a clear separation of PxP and PcP is not feasible anymore. Therefore the identification of a precursor should be best on broad-band data which is in agreement with the data analysis experience. In the summary figure 4.18 the short-period Semipalatinsk results are also displayed but only from 11 events a PcP amplitude could be reliably determined. Only small deviations from the broad-band results can be observed. In the lower seismogram section of figure 4.12 model -5%-15%+5% is overlain by the PcP impulse from event 1985-Jun-15. Obviously, the higher frequency event signal does not fit the 1 Hz synthetic wavelet. The larger postcursor compared to the modelled results may arise from undulations since it was shown in

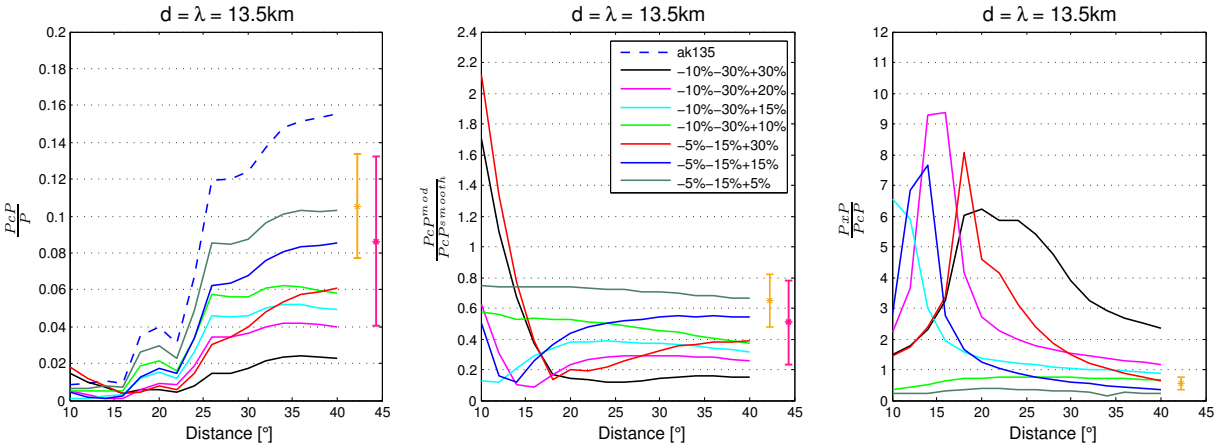

Fig. 4.11: The measured amplitude ratios of the **GRF - Semipalatinsk** events, including both subregions, are overlain by the 1 Hz synthetic calculations for a ULVZ thickness of 13.5 km. The PcP amplitude is clearly reduced compared to the global smooth model as can be seen in the PcP/P and PcP^{mod}/PcP^{smooth} diagrams. Although the scattering of the data is fairly high (the marked orange errorbars give the standard deviations) the mean values range around the moderate model with contrasts of -5% V_P, -15% V_S and +5% density for all amplitude scalings. Also the measured PxP/PcP ratios are clearly below one and support the assumed model. Furthermore, the results of the **NORSAR - Hindu Kush** measurements are indicated as pink mean values and errorbars. Even the data scattering is much higher than for GRF - Semipalatinsk all determined amplitude ratios are clearly lower than the global model and they confirm the assumption of the moderate ULVZ. However, a precursor could not be observed because of the poor SNR.

section 3.8.2 that only postcursors can be amplified by focussing effects whereas PxP and PcP remain unaffected.

In case of an existing ULVZ model -5%-15%+5% would not be the only one that is able to explain the measured values. It has been shown that the results are ambiguous for varying V_S and density contrasts (see section 3.4 and figure 3.18). In terms of the previous results the density contrast might be slightly lower or higher than +5%. Otherwise a completely different ULVZ configuration is also feasible according to the shown half-space reflection coefficients in figure 3.18. Thus a model with contrasts of -10%-20%+10% yields a similar absolute reflection coefficient as -5%-15%+5% at a distance of about 42°. Also for that configuration the precursor would be very small (PxP/PcP < 1) since $\delta|V_P| = \delta|\rho|$.
A further limitation of the assumptions seems not possible in view of seismological aspects. Any additional restrictions could result from mineralogical experiments and geodynamical modellings. In that context the evaluation of a quantitative confidence range for a certain ULVZ model cannot be derived from seismological computations and observations so far.

It should be noted that for the events shown in figures 4.9, 7.1 and 7.2 a notable single, negative peak with a slowness around 3.4 s/° can be seen that arrives about 5 s before PcP (at about 583 s related to the relative time scales). A couple of other events could be found which also indicate such a feature whereas some others do not show this. The observed slowness correlates with the predicted PcP slowness. In view of the synthetic arrival time differences, given in figure 3.23, the travel time difference here would corresponds to a reflector depth of about 2850 km, i. e. 40 km above the CMB. Assuming that this feature is a true signal it seems to be improbable that this is the precursor since the PxP-PcP travel time difference is in the order of the PcP-postcursor

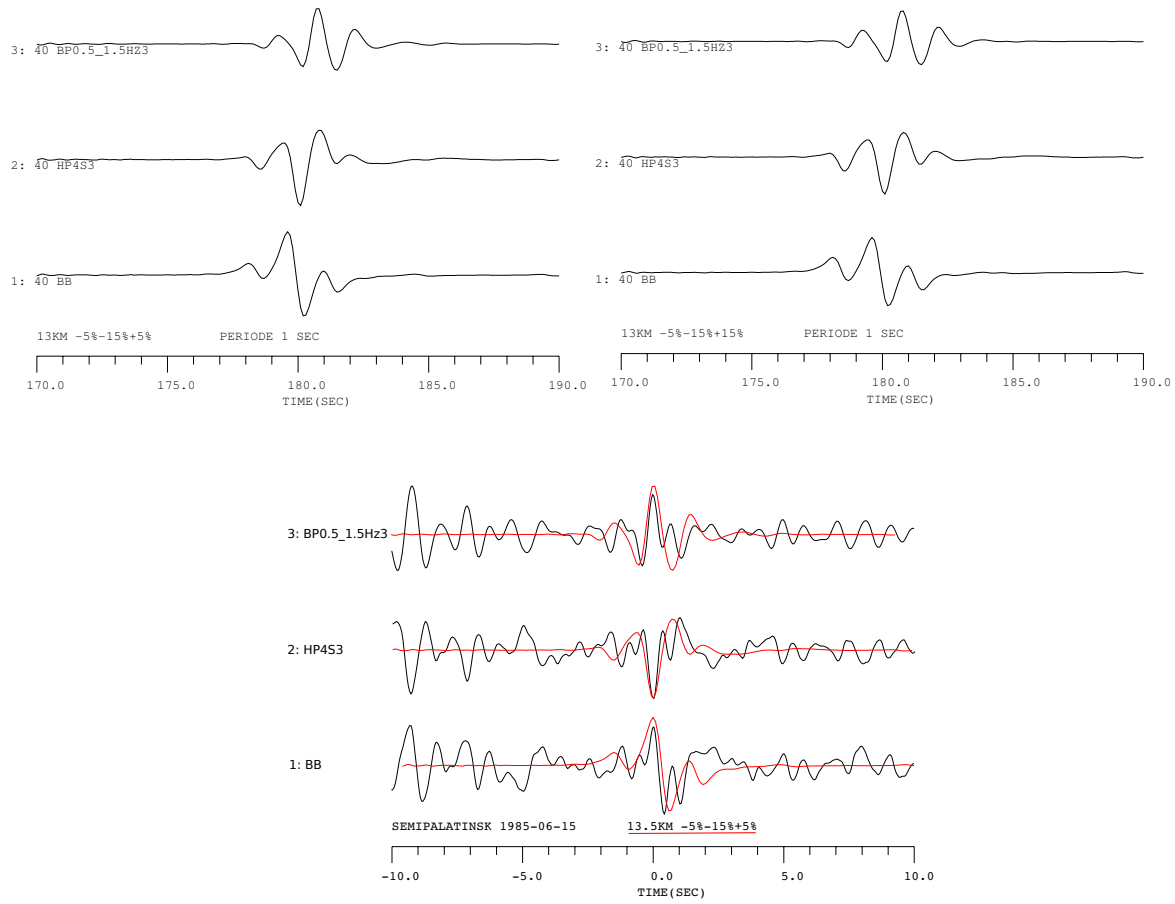

Fig. 4.12: PcP at 40° distance for a thickness of 13.5 km using a dominant source period of 1 sec. **Left:** Model -5%-15%+5% and **right:** Model -5%-15%+15%. The traces show the 'broad-band' PcP results as well as the high-pass filtering of 4 sec and a band-pass filtering between 0.5-1.5 Hz. Note that the time scale refers to a velocity reduction of 12.2 km/s and a time reduction of 20 s. All traces are normalised to the maximum amplitude on all displayed traces within their full length, respectively. Same zoom factor has been applied. The waveforms are almost identical whereby the PcP amplitudes are slightly reduced for the right model contrast, i.e. solely by the pulse shape a distinction between these two model is not possible. In the **lower** seismogram section model -5%-15%+5% is overlain by the PcP impulse from event 1985-Jun-15 whereby the frequency content is even higher.

travel time difference. Since the postcursor is well developed for almost every event, it is quite sure that the postcursor arrives 1 - 1.5 s after PcP. Even in reference to a strong topography, as it was presented in section 3.8.2, it is not possible to generate the observed travel time distortion. Furthermore, a true precursor should yield the same or at least a similar slowness as PcP itself even for a thicker ULVZ. Therefore, the cause for those energy with negative polarity remains unexplained.

4.1.3 Analysis of Deep Earthquakes

4.1.3.1 Hindu Kush Region

The deep earthquakes from the Hindu Kush region enable a high-quality PcP study since the events occur much more frequently than those in central Europe and also with sufficient large magnitudes. 10 events with similar depth and focal mechanism were selected and listed in table 4.1. The depths range between 200 km and 220 km with a dominant trust faulting. The correction factors for the radiation pattern can be found in table 7.2. Both P and PcP emerge far away from the nodal plane. PcP has always the same (positive) polarity as P.
The mean distance towards GRF is 44.3° with a theoretical BAZ of about 84°. A huge mislocation of about +10° was measured for every, event which is consistent with the results from Krüger and Weber [1992]. Therefore the observed BAZ value of 95° or 92° were applied to the beamforming processes. As in case of Semipalatinsk this is a nontrivial distance range since PP and its triplication phases arrive at a similar time as PcP. Nevertheless, the amplitude measurements are somewhat more reliable due to the fact that the complex PP wave train arrives about 7 s after PcP. Figure 4.13 shows the 2009-Oct-29 event within a slowness range from 2.0 s/°to 12 s/°. The predicted u_P is 7.9 s/° and u_{PcP} amounts to 3.4 s/°. All measured P-slownesses are reduced up to -0.9 s/°. Determinations of u_{PcP} revealed an enormous scattering of ±1 s/°, probably due to the poor slowness resolution for that direction. As mentioned above the GRF array can be roughly divided into a northern (CN) and southern cluster (CS) because of the changing geological structure. The thicker sediment layers below the northern stations (A1-B4) generate much larger P amplitudes with respect to the southern cluster for a BAZ of about 85°. This could be observed clearly for the Hindu Kush events, where the beamed PcP/P ratios for CS are almost doubled compared to the beam amplitude ratios of CN since the PcP amplitude is by far less amplified at CN than P. These amplitude anomalies are in good agreement with the findings by Weber [1994b]. However, a similar slowness (or travel time) residual between CN and CS could not be detected but the direct opposite: The measured P-slownesses for CN are clearly reduced with respect to CS although the seismic velocities should be lower at the northern site. Moreover, u_P for CS is almost constant relative to the predicted value of 7.9 s/° though the previous study have shown clearly shorter travel times for the southern stations and almost no difference for CN. In any case, those discrepancies are beyond the scope of this thesis. For the purpose of this study beamed traces of all stations are considered where the site related anomalies are averaged. This process is allowed since only CMB features are relevant.

All beamed broad-band traces for the maximum PcP amplitudes, respectively, are shown in figure 4.14. The PcP impulses are aligned on their positive peaks and marked as red shaded area. After the removal of the radiation pattern a mean PcP/P ratio of 0.17 is obtained where a large amplitude scattering occurs (cf. figure 4.18). The mean value fits the predicted amplitude ratio of the global smooth model. The noise level is highly variable for the single events but no dependency on the seasons can be noticed. Also the SNR is not related to the magnitude. For instance, events 3 and 10 have moment magnitudes of 5.5 but PcP can be identified very clearly due to the high frequency impulse even the SNR is less than 2 (the noise level was determined from the time window 10 s before PcP). All other events have magnitudes larger than 6.0. In general, the coherence of the PcP waveforms and frequencies is less than for the explosion

events but a fairly simple PcP impulse is well developed on the sum trace. The corresponding additional negative peak results from the source signal and is not related to a CMB feature. A significant characteristic is obtained for the short-period range between 0.5 - 1.5 Hz. The PcP/P ratio is clearly increased by about 50% although the data scattering is even higher than for the broad-band relations. Such an high-frequency amplitude anomaly can be correlated with the CMB topography results by Kampfmann and Müller [1989]. They modelled the largest focussing effects for distances up to 45° using a long-wavelength undulation of 200 km with a height of 1 km. Though, it was shown in section 3.8.2 that the magnitude of heights and depressions may have only a secondary effect on structural amplitude amplifications since the modelled ULVZ topography, with ups and downs of 10 km and 20 km, also results in (de)-focussing effects up to 60%. The PcP^{data}/PcP^{smooth} ratio confirms these findings. For the broad-band data no deviations can be seen, i. e. the CMB shows no anomalies. In contrast, a short-period filtering reveals significant larger PcP amplitudes with a mean increase of 60%. To sum up, a strong CMB topography could exist below NNW of the Caspian Sea with an effective Fresnel zone of 120 km by 200 km.

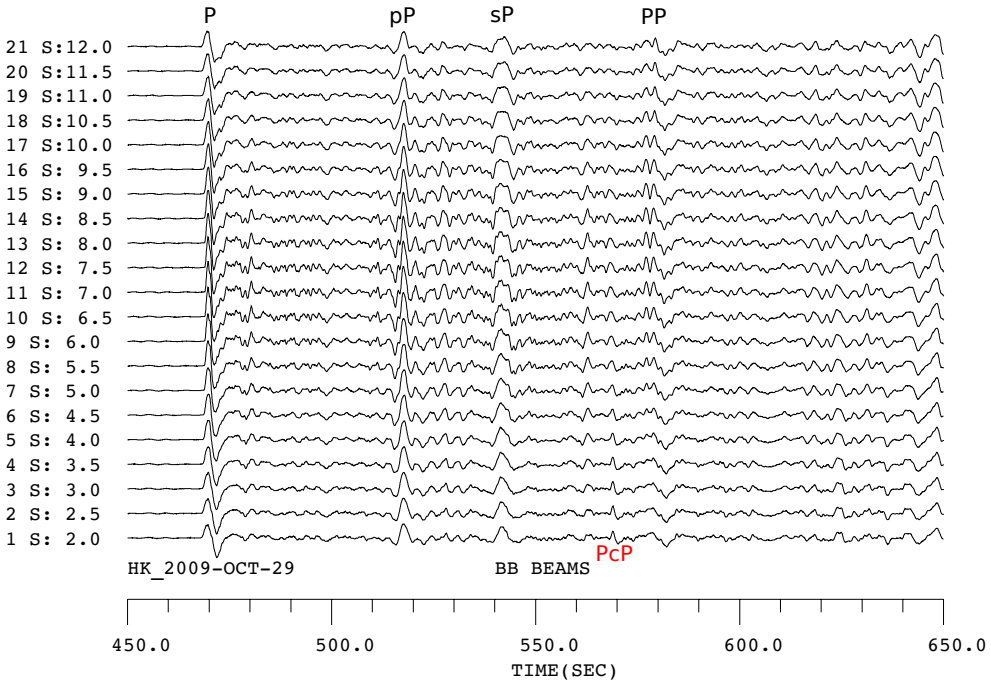

Fig. 4.13: Vespagram from the **Hindu Kush** event of 2009-Oct-29 with a slowness range between 2 s/° and 12 s/°. The distance is 44.38°. The well resolved P, sP, pP, PP and PcP phases are indicated. The relative time scale refers to the origin time. About 6 s before PcP and 20 s after sP a notable wave with negative polarity arrives. Based on the slowness measurements, this signal can be assigned to the highly complex sP wave train possibly caused by subduction reverberations.

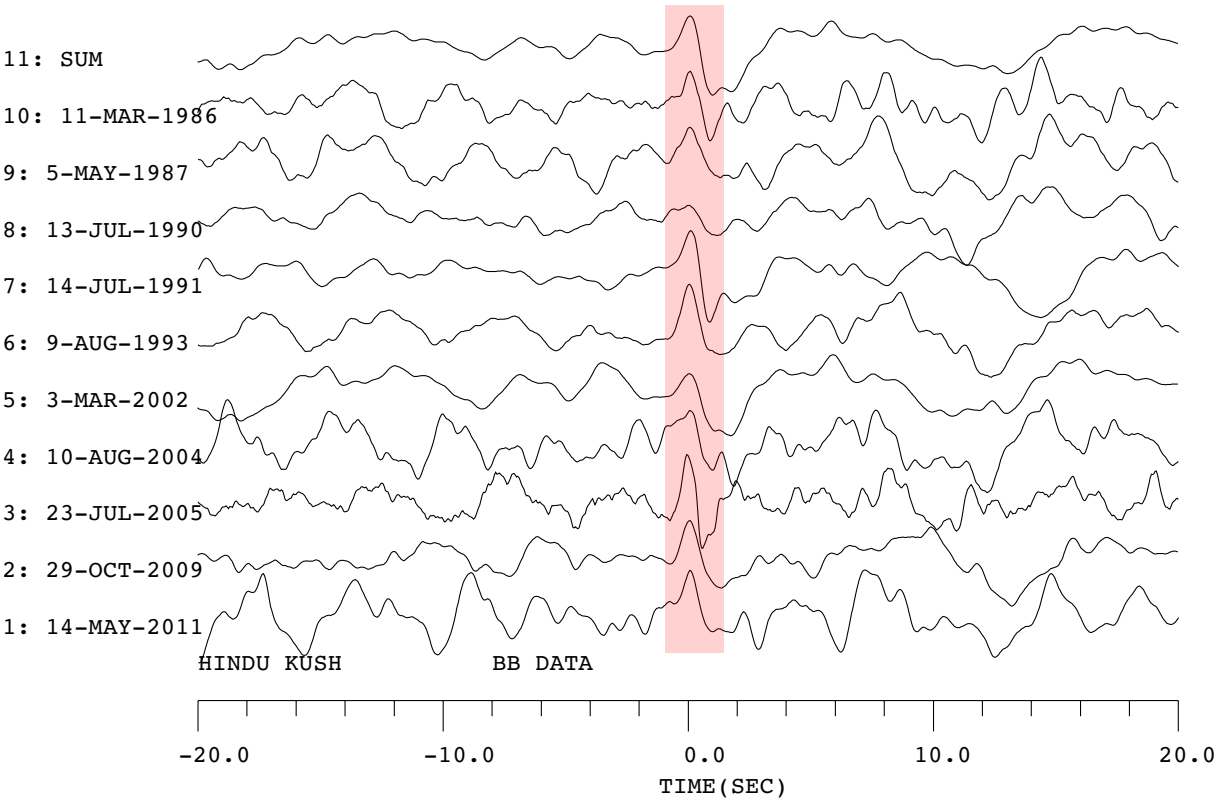

Fig. 4.14: All inspected deep earthquakes from the **Hindu Kush** region. The mean distance is 44.3° with a theoretical BAZ of 84°. Shown are the appropriate beamed broad-band traces of each event and the summed trace. The PcP impulses are aligned on their positive peaks (red shaded area). Each trace is normalised to its maximum amplitude within the displayed time window. The noise level varied highly for the single events where no dependence on the season can be noticed. Also the SNR is not related to the magnitude. The coherence of the PcP waveforms and frequency is less than for the explosion events.

4.1.3.2 Sicily

The deep earthquakes north of Sicily provide a PcP analysis at very steep incidence angles. The mean distance to GRF is 11.1° with a predicted BAZ of about 164°. The slowness resolution should be best from that direction where the azimuth resolution is worse regarding the GRF aperture. A mislocation BAZ of 162° was used for the beamforming. These events are infrequent and occur between 200 km and 300 km depth with a largest moment magnitude of 5.8. The epicentres cover an area of about 100 km by 100 km whereby the effective Fresnel zones overlap and yield almost a circle of about 100 km by 110 km at the CMB, respectively.
Unfortunately, the focal mechanisms are adverse related to GRF since at three of the four selected events either P or PcP emerge on the nodal plane which makes a correction for the radiation pattern useless. No radiation pattern correction was applied for these events since this potential error would be larger than those from a non-use of the correction factor. All other events included in the event bulletins are too weak and noisy.
The P impulse is highly complex and incoherent for the four events thus a PcP determination is difficult. The P-slownesses show a variance of +0.2 s/° and -0.4 s/° compared to the predicted value of 12.6 s/°. The theoretical PcP slowness is about 1 s/°. Measuring the PcP amplitude reveal ambiguous and implausible u_{PcP} between 0 and 2 s/°. Further, a clear PcP identification is not possible since the reflection coefficient is only about 2% of the incident signal and

indistinguishable from the noise level. The PcP resolution is better using a high-pass filter of 4 s (third order) and a short-period bandpass filter of 0.5 - 1.5 Hz which is shown in figure 4.15. The short-period filtered beam traces for the maximum PcP amplitudes (black) are underlaid by the appropriate P signal (red). All impulses are aligned on their largest negative peak. No summed trace is shown due to the different radiation pattern. Again, the results of the amplitude ratios are displayed in figure 4.18 but the measurement uncertainty is quite large (the high-pass filtered ratios are shown instead of the BB data). The PcP/P ratios fit the smooth model and also the standard deviations are still fairly small. A PcP^{data}/PcP^{smooth} ratio gives an increased mean value by about 40% compared to the smooth PcP amplitude. However, these amplitude measurements comprise a large uncertainty and the outcomes should not be overinterpreted.
It should be mentioned that also the very deep events close to Naples were investigated. However, the SNR is too poor, even using a high-pass or short-period filter, so that a PcP analysis is not feasible.

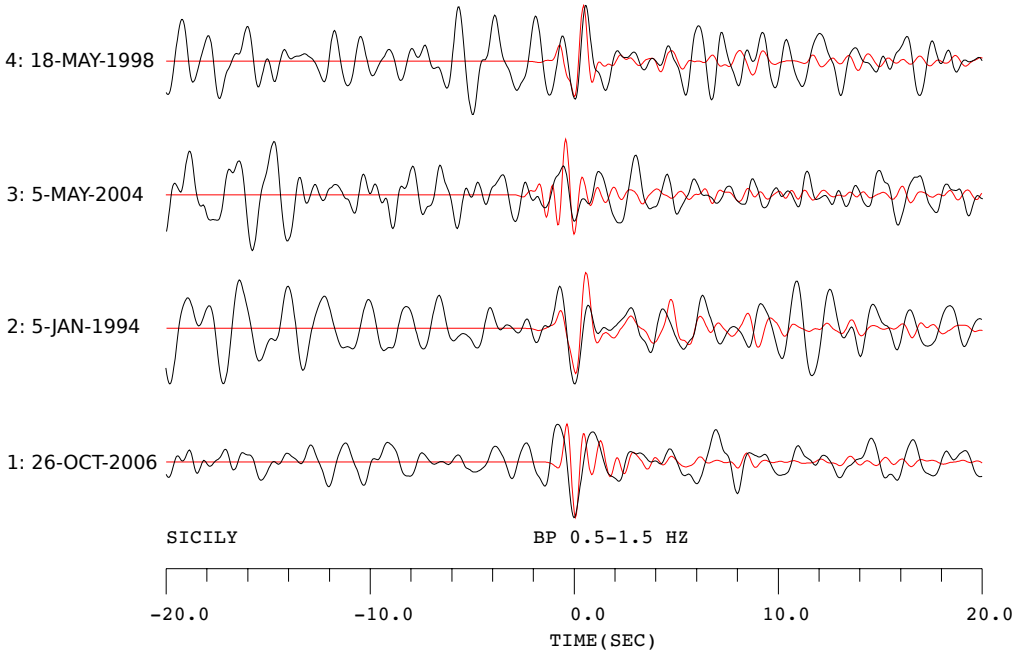

Fig. 4.15: Short-period filtered P (red) and PcP (black) beams of the **Sicily** events used. The mean distance is 11.1° with a predicted BAZ of about 164°. All pulses are aligned on their largest negative peak, respectively. The traces are normalised to the absolute maximum amplitude within the displayed time window. No summed trace is shown due to the different radiation pattern.

4.1.3.3 Spain

One very deep event occurred in Spain with a depth of about 620 km and a moment magnitude of 6.3. The epicentral distance is 16.5° with a theoretical BAZ of 225°. No significant azimuthal mislocation could be observed. The bounce point at the CMB is about 100 km east of Toulouse, France with an effective Fresnel zone of 120 km by 100 km at the CMB.
The first onset of P is very weak, followed by a complex wave train, although that ray does not emerge close to the nodal plane. This may indicate a complex rupture process. Because of the unusual event location, moment tensor solutions from several agencies were compared which are also summarised in the EMSC Database (European-Mediterranean Seismological Centre). In

relation to the PcP/P correction factor using CMT a deviation of -20% (NEIC), -7% (INGV) and +11% (IGN) occur, respectively. Thus, a notable effect on the amplitude ratios cannot be observed.
Moreover, large focussing and defocussing effects are expected due to the location within the triplication range. As a consequence the PcP amplitude is hardly identifiable on broad-band beams. Neither a high-pass filter nor short-period filters are able to enhance the core-reflected signal. Even the application of cross-correlation techniques could not simplify the seismograms. The most suitable broad-band beams are displayed in figure 4.16. Solely the broad-band amplitudes were determined with a resultant positive deviation for PcP/P and an enormous PcP^{data}/PcP^{smooth} ratio (see figure 4.18). However, an interpretation cannot be drawn from these findings.

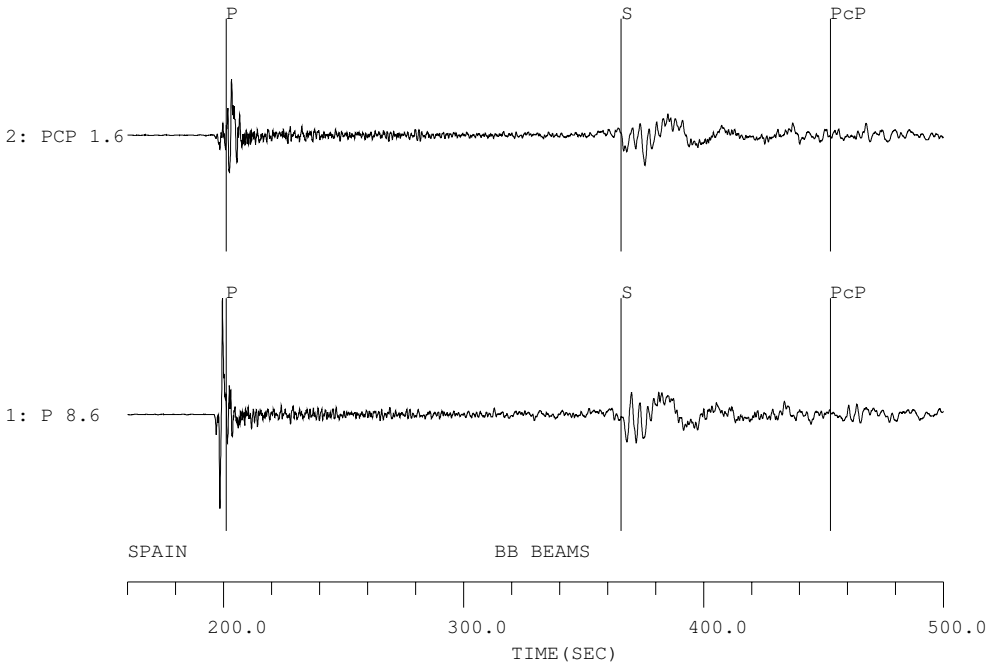

Fig. 4.16: Broad-band beams of the appropriate P and PcP slownesses for the **Spain** event. Indicated are the predicted arrival times of P, S and PcP. The P wave train is highly complex and PcP is hardly identifiable. The traces are normalised to absolute maximum amplitude within the displayed time window.

4.1.3.4 Romania

Intermediate deep earthquakes occur about 120 km north of Bucharest, Romania. The seismic activity in this region is well known and assumed to be a result of a Tertiary and Quaternary convergence of two intracontinental zones. The deep earthquakes indicate the presence of a paleo-slab below the Carpathian Arc [Monfret et al., 1990].
The depths of the selected events range from 130 km to 150 km within an epicentral area of 30 km by 50 km. One very strong event occurred on 1986-Aug-30 with a moment magnitude of 7.2. All other events have magnitudes of 5.2 and 5.4. The calculated radiation patterns show opposite polarities for P and PcP where the first motion is negative respect to GRF. This is in agreement with the recorded waveforms which are illustrated in figure 4.17. A high-pass filter of 4 s has been applied and the predicted arrival times of PcP are marked. The PcP signals are aligned on their large negative peaks. The source distance amounts to 11° with a theoretical

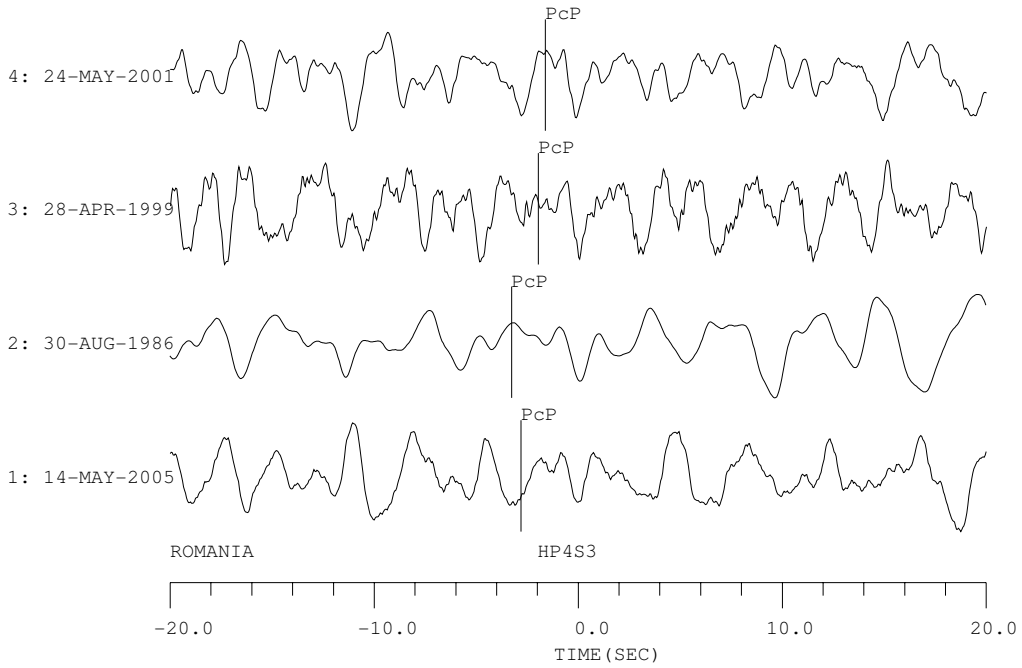

Fig. 4.17: PcP beams of the **Romania** events. A high-pass filter of 4 s has been applied. The PcP signals are aligned on their large negative peaks at time zero. The predicted arrival time are also indicated. Each trace is normalised to its maximum amplitude within the displayed time window.

BAZ of about 106°. A azimuthal mislocation could not be observed. Although the SNR is about 1, the high-pass filtered PcP impulse can be detected because of its frequency and travel time. Moreover, at this distance range no other phases interfere with PcP. A clear determination on the broad-band or short-period filtered recordings was not possible.
The high-pass filtered PcP/P ratios as well as the PcP^{data}/PcP^{smooth} relations yield a huge positive deviation in terms of the global model. Even the measured amplitudes reveal a large scattering, the PcP signals are significantly increased. All P impulses are fairly simple and the source distance is still outside the upper mantle triplication range. Therefore, no uncertainties respect to the P wave should occur. In view of a possible CMB topography the arrival times of PcP have been considered. For all events a time delay can be seen but there is no consistency. The travel time delays, with respect to the predicted PcP arrival time, range between +0.2 s to +1.3 s. In consideration of the synthetic results, an extreme positive density contrast of +30% could also produce such large amplitude amplifications. However there is no evidence for a precursor which would be very strong within this steep-angle region and for a strong low-velocity anomaly. Hence, it is more likely that focussing effects at the CMB generate the unusual PcP amplitudes. The projected reflection zone from the CMB is about 50 km north of Budapest with a small effective Fresnel zone of about 100 km by 100 km. In addition, also a larger data set could change these findings in the future.

4.1.3.5 Summary of the Gräfenberg Data

- PNE: PcP^{data}/PcP^{smooth} ratio provide evidence for a thin, gradient mantle-side CMTZ or a very thin, moderate ULVZ of about 5 km thickness
- Novaya Zemlya: Both BB and SP data reveal focussing effects at the CMB

- Semipalatinsk: Evidence for a 10 - 13.5 km thick ULVZ with possible contrasts of -5% V_P, -15% V_S and +5% density (or -10%, -20%, +10%, respectively)
- Hindu Kush: SP data indicate an undulating CMB
- Sicily: Rather smooth CMB, but the data quality is poor
- Spain: Only one event, no conclusion about the CMB possible
- Romania: Huge amplitude ratios may indicate an undulating CMB

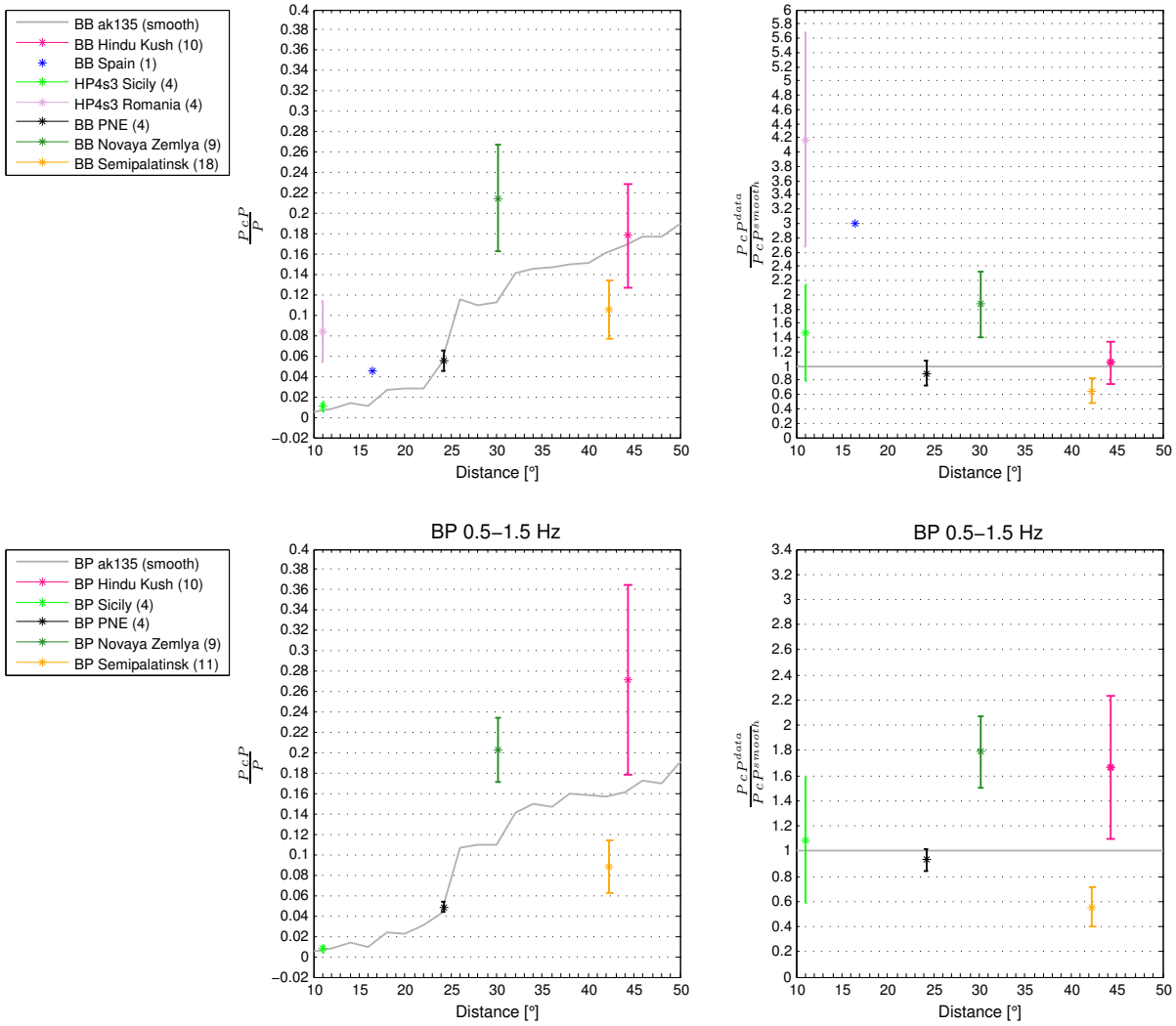

Fig. 4.18: Summary of all measured amplitude ratios analysed from the Gräfenberg data. The grey line in the PcP/P diagrams show the smooth results of the attenuated, velocity proportional synthetics with a dominant source frequency of 1 Hz (calculated by the ray tracing program *Xgbm*). The stars mark the mean values and the errorbars show the standard deviations, respectively. **Top:** Broad-band data or high-pass filtered data in case of the Sicily and Romania events. **Bottom:** A Butterworth bandpass filter of 0.5 - 1.5 Hz (third order) has been applied. Note that not all events could be band-pass filtered. The vertical scales of the PcP^{data}/PcP^{smooth} diagrams are different.

4.2 NORSAR Array

4.2.1 Location of Events and the Array

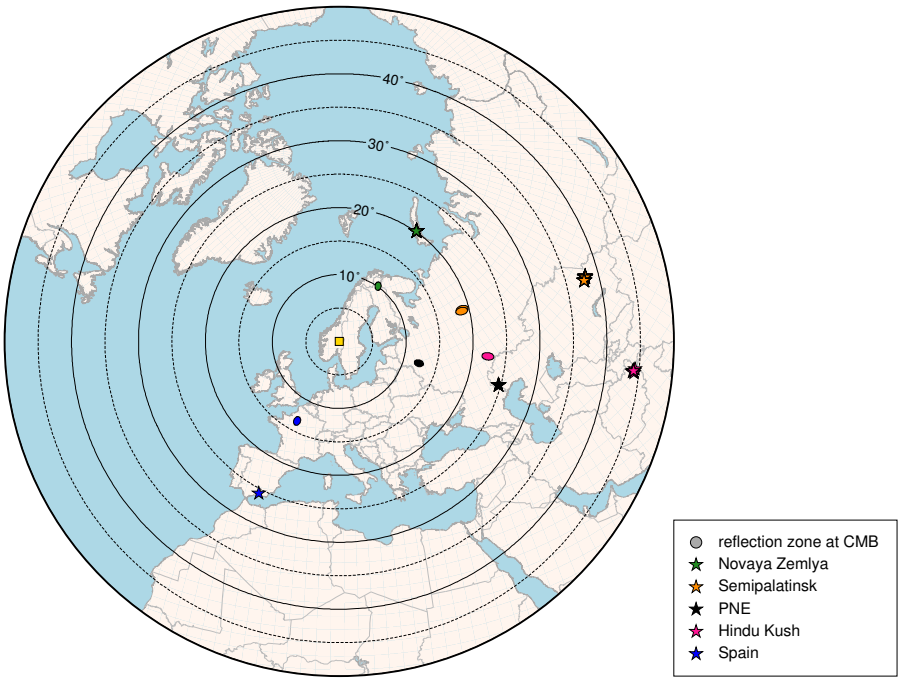

Fig. 4.19: Map of studied events respect to the NORSAR array which is located in the center of the plot and marked as golden square. Shown is an azimuthal equidistant projection up to 50°. Earthquakes and nuclear explosions are marked as stars. The ellipses correspond to the appropriate effective Fresnel zones at the CMB.

The original, large NORSAR array in south Norway was established in 1968 with the main purpose of the verification of compliance regarding to the Comprehensive Nuclear-Test-Ban Treaty (CTBT). The present small-aperture array is in operation since 1976 and denoted by NOA. It consists of 7 subarrays where at each subarray one 3-component broad-band and five 1-component short-period seismometer are deployed (see figure 2.4). Before 1995 long-period instruments were installed instead of the today's broad-band seismometer. This hampers studying earthquakes since BB waveform data are only available after 2000. The installed KS54000 BB borehole seismometer are proportional to ground acceleration which requires a careful restitution. One of the borehole instruments was replaced by a velocity proportional Güralp CMG-3T seismometer in 2000. Both seismometer types have a sampling rate of 40 Hz.
The nuclear explosions were analysed using the short-period instruments. Between 1968 and 1994 NORSAR was equipped with HS-10-1 short-period seismometers which have a gain range of ± 16 V and a sampling rate of 20 Hz [Pirli, 2010]. This small dynamic range and exceptional P-wave focussing effects at the receiver site, described in the next section, cause clipped P impulses for the explosion events even the magnitude m_b is less than 5. Moreover, the recordings by NORSAR involve in general a higher noise level compared to GRF. Because of the array location close to the North Sea and a very deep, large lake directly south of the stations, dominant oceanic microwaves and a generally high noise level can be seen on the recordings.
As at the Gräfenberg array large slowness mislocations are known at NORSAR which are sum-

marised by Schweitzer [2001]. Mean deviations up to 2 s/° occur where no dependence on the direction can be observed. However, due to the large-scale correction vector figures in his study the required BAZ values were determined by event location in time domain.
Due to the circular array aperture no azimuth dependent resolution limits occur as already mentioned in section 2.4. Figure 4.19 shows the inspected earthquake and explosion events using the NORSAR array on an equidistant azimuthal map projection. The epicentral distances in steps of 5° are illustrated. The ellipses are the surface projections of the appropriate effective Fresnel zones.

4.2.2 Analysis of Nuclear Explosions

Since the small-aperture NORSAR array was installed in 1976 more sufficiently strong events could be analysed than at GRF. Unfortunately, the inspected data show P impulses, larger than the dynamic range of the instruments, i.e. the P amplitudes are clipped. This is true for almost all events from Novaya Zemlya, Semipalatinsk and the PNEs. These P-wave focussing effects at NORSAR are well known and described by Mykkeltveit [1990]. Even explosions with body wave magnitudes of 4.5 generated signals which have exceeded the dynamic range of the short-period seismometers. The long-period recordings cannot be used for the high-frequency explosion sources. Therefore, a detailed study and evaluation of PcP amplitude ratios, as was done for the Gräfenberg data, is not possible.
In the following two examples of a PcP impulse are given. Though, as can be seen, the SNR is very bad and PcP is indistinguishable from the noise level, above all if the predicted slowness values and travel times are not reliable. The beam traces for the PNE event of 1979-Jul-14 are illustrated in figure 4.20. The red vespagram results from a linear beamforming process where the black seismograms show the 4th root beams. The predicted arrival time of PcP is marked at the theoretical slowness value of 2.2 s/°. A fast Fourier transform shows a significant spectral plateau between 1 Hz and 3 Hz. All beam traces have then been filtered using a band-pass filter between 0.5 - 1.5 Hz and are normalised to their maximum amplitude within the displayed time window. Other band-pass and high-pass filters were tested and the best solution is shown here. The linear beam traces are not able to resolve the PcP impulse. Only with the overlaying 4th root beams the core-reflected energy becomes visible where the maximum amplitude corresponds to a slowness of 2.8 s/°. Some signals with similar slowness arrive 4 s and 7 s before and also 4 s after PcP. Nonetheless, a reliable analysis is not possible and it remains unclear whether these additional signals are true phases or just noise. One PNE event was found which has no truncated P amplitudes. The Batholith-2 explosion of 1987-Oct-3 with $m_b = 5.3$ yield a PcP reduction of about 20%. The amplitudes were measured from the band-pass filtered recordings (BP 0.6 - 3 Hz). Though the noise level is very high and on the basis of only one event any interpretations are not valid.
Another example is illustrated in figure 4.21 for the Semipalatinsk event of 1985-Jun-15. Here the P wave train is also clipped for all stations and a band-pass filter of 0.6 - 3.0 Hz has been applied. Although this is a strong summer event with m_b of 6.1 and clear waveforms were recorded by GRF, PcP is very weak with a poor SNR.
All further inspected events, even though from the Caspian Sea, Semipalatinsk or Novaya Zemlya, reveal clipped P wave trains and overall noisy data so that also a study of the PcP waveforms is not feasible.

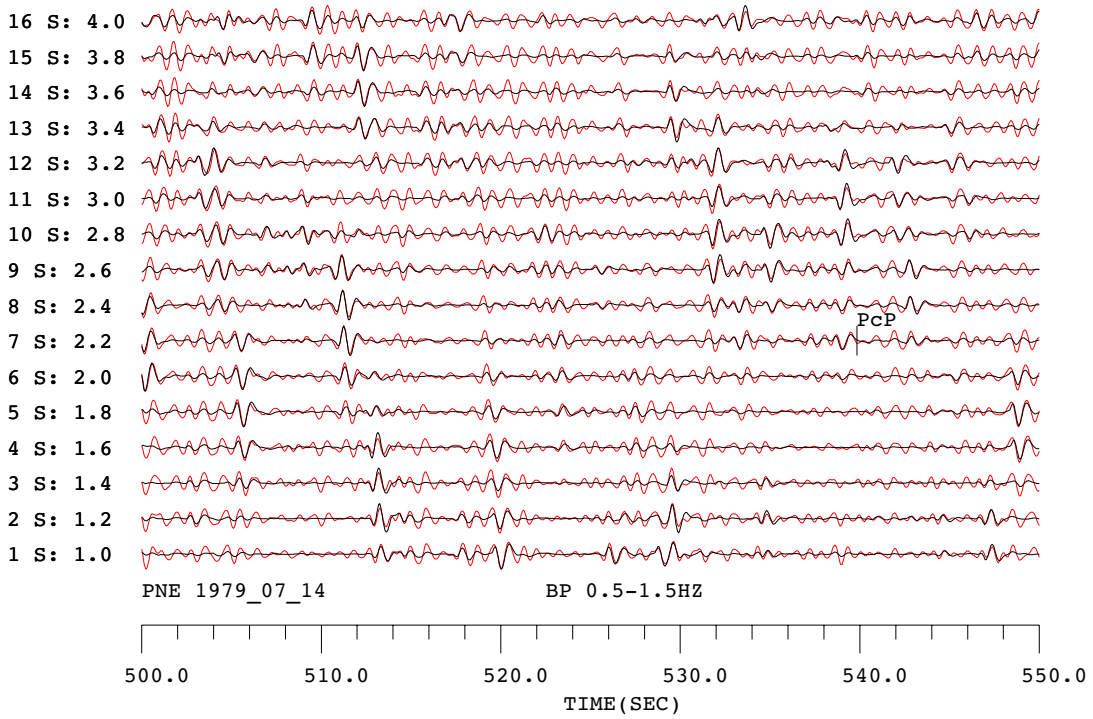

Fig. 4.20: Vespagrams of the **PNE** event of 1979-Jul-14 for a slowness range of 1.0 s/° to 4.0 s/°. The red traces show the results of a linear vespagram where the black seismograms illustrate the 4th root beams. The predicted arrival time of PcP is marked at the theoretical slowness value of 2.2 s/°. The source distance is 24.7° at a theoretical BAZ of 105°. A band-pass filter of 0.5-1.5 Hz has been applied.

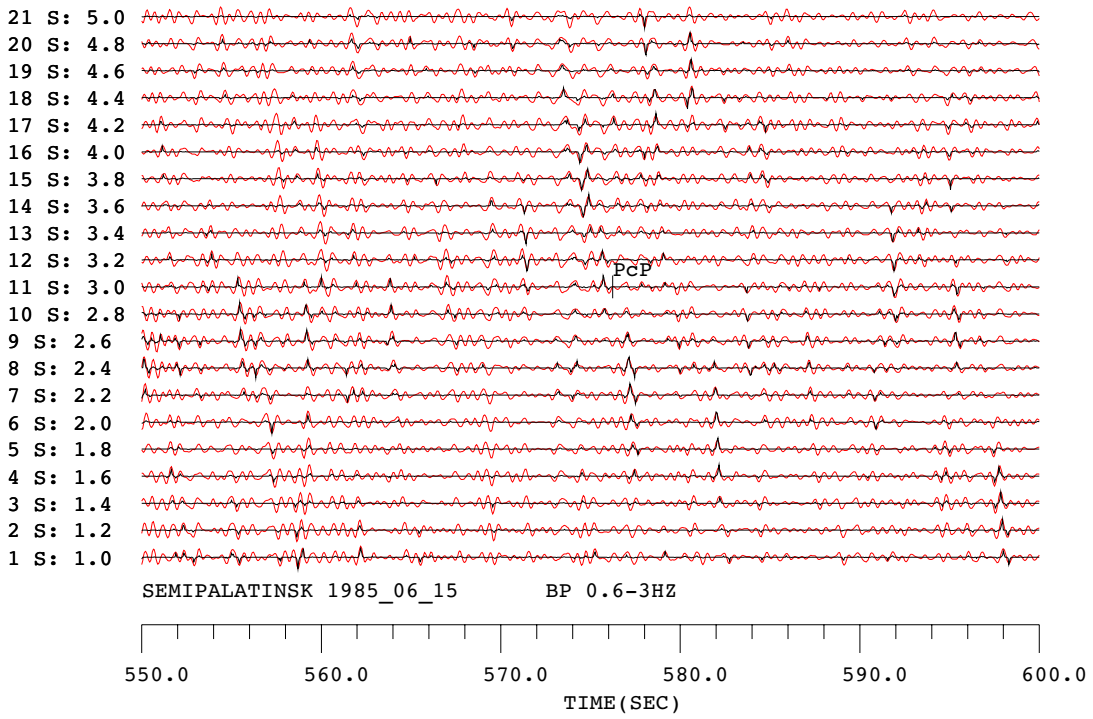

Fig. 4.21: Vespagrams of the **Semipalatinsk** event of 1985-Jun-15 for a slowness range of 1.0 s/° to 5.0 s/°. The red traces show the results of a linear vespagram where the black seismograms illustrate the 4th root beams. The predicted arrival time of PcP is marked at the theoretical slowness value of 3.0 s/°. The source distance is 38.4° at a theoretical BAZ of 75°. A band-pass filter of 0.6 - 3.0 Hz has been applied.

4.2.3 Analysis of Deep Earthquakes

4.2.3.1 Hindu Kush

The deep earthquakes observed at NORSAR stations have a mean distance of 44.4° and a theoretical BAZ of about 95°. An azimuthal mislocation of +8° was determined and applied to the beamforming processes. The radiation patterns with respect to NORSAR are very similar as those of to GRF with take-off angles of P and PcP far away from the nodal plane. Both P and PcP have positive first arrivals. Since waveform data before 2000 are not available, four events between 2001 and 2009 were chosen which are listed in table 4.1. As mentioned in the previous subsection the noise level at NORSAR is much higher compared to GRF. Due to the dominant oceanic microwaves a high-pass filter of 4 s (third order) has been applied and only the filtered data are discussed below. An evaluation of the broad-band recordings as well as short-period filtered data were non-satisfying.
Figure 4.22 shows the vespagram of the earthquake of 2009-Oct-29 for a slowness range between 2 s/° and 12 s/° similar as in figure 4.13. The distance is the same but PcP is not well resolved compared to the recordings by GRF. Moreover an aliasing effects seems to occur for PP which can be seen on the lowermost traces, i.e. higher energy is generated for a slowness of 2 s/°.
The vespagram reveals clearly reduced slowness values both for P and PcP. This is in agreement with the other events studied. The predicted u_P is 7.9 s/° where a mean value of 7.4 s/° is observed. The measured PcP slownesses range between 2.0 s/° and 4.4 s/° where these values are not reliable due to the poor SNR.
Figure 4.23 shows the beamforming results for P (red) and PcP (black) which are aligned on their maximum negative peaks, respectively. For all events the P impulse is very complex and caused by structural reverberations below the receiver site whereas the appropriate GRF recordings have not shown such long wave trains (cf. figure 7.3 in the appendix). The application of a high-pass filter even enhances the complex wave train and for this reason also the PcP signal is highly complex.
Taking all these factors into account the measurements of the PcP amplitudes are nontrivial. As a result a large scatter of the determined amplitude ratios occur. Nonetheless, a clear PcP reduction could be detected both for PcP/P and PcP^{data}/PcP^{smooth} with a mean reduction of -45%. Beside that findings, the key result of the NORSAR - Hindu Kush study is the location of the effective Fresnel zone which is situated close to the reflection zone of GRF - Semipalatinsk (see figure 6.1). The mean distance between the two bounce points is 220 km at the CMB. Therefore, the amplitude ratio results are indicated as pink errorbars in the diagrams of figure 4.11. Although the mean amplitudes are slightly lower than for the Semipalatinsk measurements, both receiver-event arrangements reveal a moderate ULVZ with contrasts of -5% V_P, -15% V_S and +5% to +15% density. However, due to the high noise level and complex wave trains there is no evidence neither for a precursor nor for a postcursor. Hence an assumption of the potential anomaly thickness is not possible. Drawing conclusions only from the NORSAR - Hindu Kush results on an ULVZ is not reliable. Though the joint interpretation with the Semipalatinsk data leads to a predictable, maybe 10-13.5 km thick, low-velocity anomaly about 600 km southeast of Moscow. Including the sizes of both Fresnel zones the potential ULVZ would have an NW-SE extension of at least 450 km.

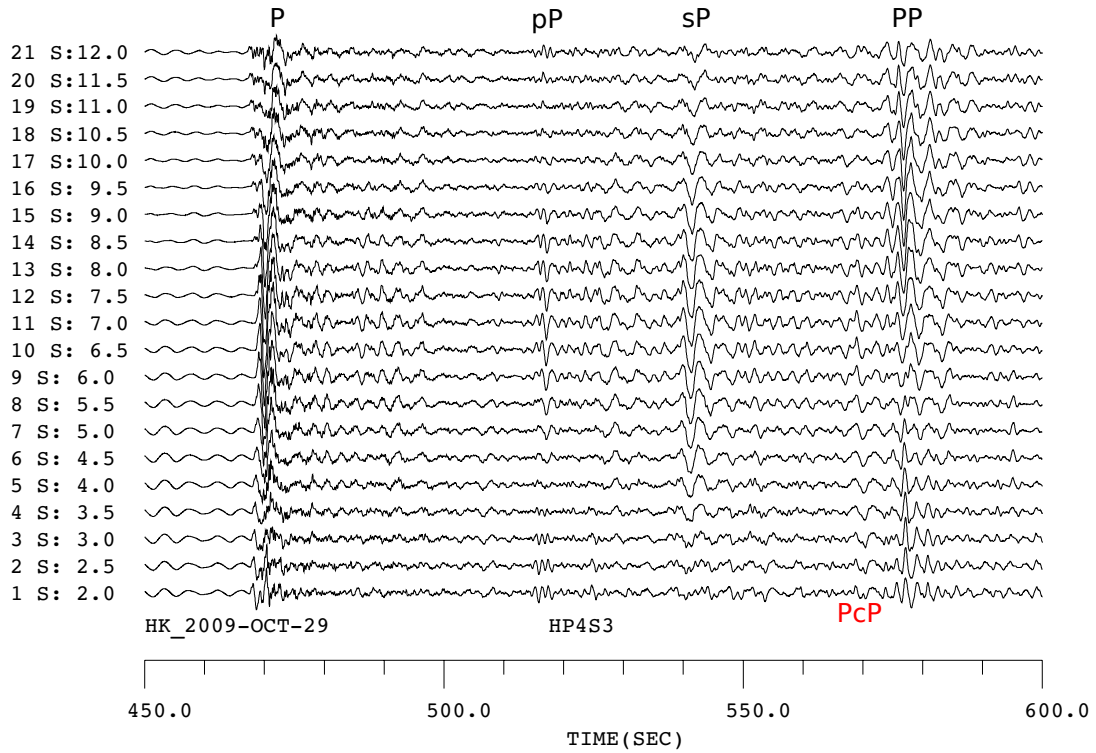

Fig. 4.22: Vespagram from the **Hindu Kush** event of 2009-Oct-29 with a slowness range between 2 s/° and 12 s/°. The distance is 44.36°. The relative time scale refers to the origin time. P, sP, pP, PP and PcP are indicated. Except for PcP the phases are well resolved using the beamforming process.

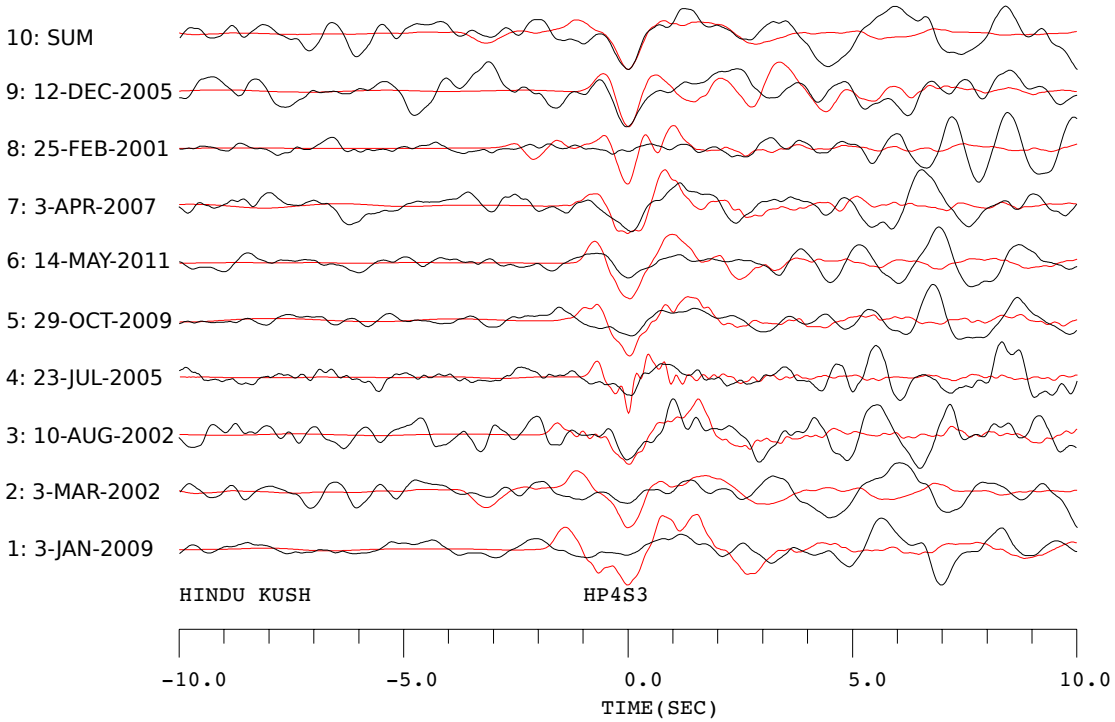

Fig. 4.23: All inspected deep earthquakes from the **Hindu Kush** region measured by the NORSAR array. The mean distance is 44.4° with a theoretical BAZ of 95°. Shown are the appropriate beam traces for P (red) and PcP (black) of each event and the summed traces, respectively. A high-pass filter of 4 s was applied. The impulses are aligned on their maximum negative peaks. Each trace is normalised to its maximum amplitude within the displayed time window.

4.2.3.2 Spain

The large Spain event recorded by the NORSAR array reveal an even more complex wavetrain compared to GRF, though the source distance of 25.5° is beyond the typical triplication range. As was shown for the Hindu Kush events notable crustal reverberations occur at the NORSAR stations. Moreover, a significant mislocation both for the P slowness and the azimuth can be observed. A BAZ deviation of -10° was obtained with respect to a theoretical value of 207°. The P amplitude was measured at a slowness of 9.8 s/° where the predicted value amounts to 8.7 s/°. As a result also the PcP signal is complex but well distinguishable from the noise level. The P and PcP amplitudes were measured on the broad-band beams and yield no deviation from the smooth amplitude ratios. Also the high-pass and short-period band-pass filtered recordings indicate no amplitude anomaly.
The result of a crosscorrelation is shown in figure 4.24 in order to enhance the PcP waveform. A duration of 4 s for the source wavelet was assumed and crosscorrelated with the PcP beam trace. This process should remove the source characteristic. A well resolved, simple PcP impulse is obtained which may refer to a rather smooth CMB. The bounce point at the CMB is situated below Paris with a effective Fresnel zone of about 150 km by 110 km.

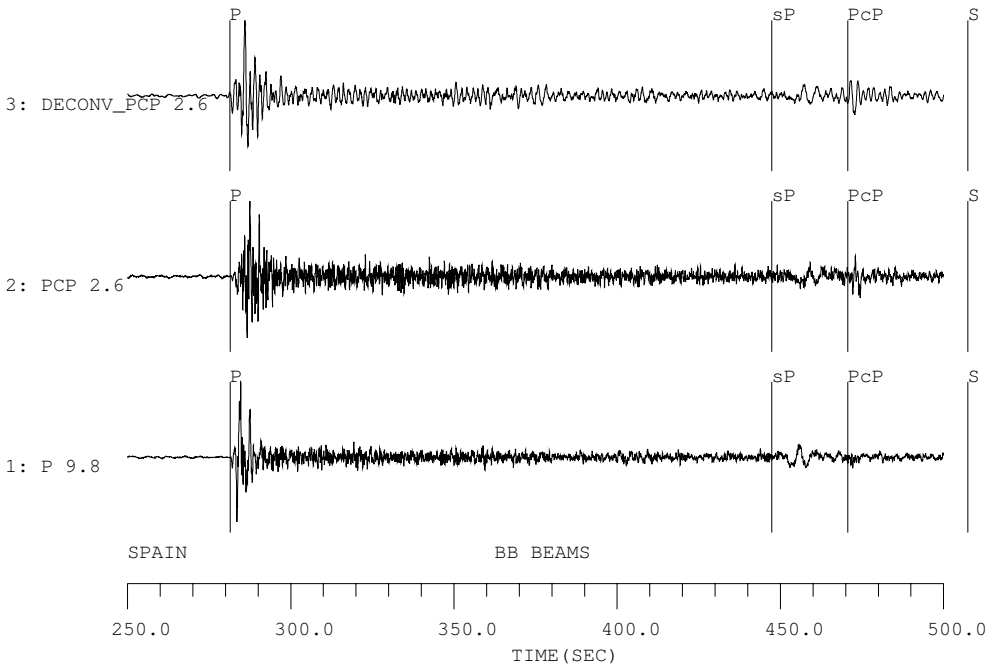

Fig. 4.24: Broad-band beams of the appropriate P and PcP slownesses for the **Spain** event. The source distance is 25.5°. Indicated are the predicted arrival times for P, sP and PcP. The P and PcP wave trains are highly complex but the core-reflected energy is clearly detectable. The traces are normalised to absolute maximum amplitude within the displayed time window. The uppermost trace shows the result of a crosscorrelation of the assumed source wavelet and the PcP beam.

Chapter 5

Discussion

The study of PcP waveform and amplitude anomalies here are based on the assumption that iron alloy from the earth's outer core could penetrate into the solid lowermost mantle. This assumption is several decades old. However, during the last few years a new hypothesis about the character of the lowermost mantle has been developed which is also able to explain the existence of ULVZs without any core-mantle interactions. In that case a large-scale basal magma ocean (BMO) was formed in Earth's early history during the accretion and heat dissipation [Labrosse et al., 2007]. Originally, that BMO reached a thickness of about 850 km above the CMB. Recent mineralogical experiments support this theory whereby it is possible to have iron enrichments in the magma for pressures greater than 76 GPa which correspond to depths below 1800 km [Nomura et al., 2011]. Such an increased silicate depleted material would result from the iron spin crossover which cause a denser partial melt. That material could reveal a density increase of about 8% for $(Mg,Fe)SiO_3$ at the basal mantle respect to the global model PREM.
A detailed view inside the mineralogical processes imply the indications for ultra-low velocity zones. For pressures greater than 76 GPa melts are more dense than solids at same conditions because of iron partitioning as a consequence of iron spin collapse. Therefore they will sink downward. The magma becomes increasingly iron enriched and depleted in silicates. During cooling and accompany very slow fractional crystallization processes the BMO becomes thinner and causes the generation of increasingly dense, Fe-rich, solid piles above the BMO. It is assumed that such piles build up the thermo-chemical steady large low shear velocity provinces (LLSVPs) beneath the Central Pacific and the African continent.
Though intuitively, a dense accumulation of solid material should result in higher seismic velocities and not in reduced shear velocities. The reason for this inverse behaviour is that the aggregate shear modulus μ decreases with a larger formula weight of Fe respect to Mg (magnesiowüstite). Therefore shear velocities are reduced (cf. equation 2.5b) [Speziale, pers. comm.].
Finally, advanced crystallization left behind residual mushy inclusions inside the dense thin layers that may correspond to the ULVZs. Hence, they would have a composition close to magnesiowüstite. These smaller-scale patches, generated in the final stage of crystallization, occur preferably at the edges of the LLSVPs which is in agreement with other geodynamical studies, e.g. by McNamara et al. [2010]. The ULVZs could be thicker at the boundary of the LLSVP by a convergence of mantle flow and CMB. Nomura et al. [2011] assume that drained off melt inclusions result in the non-observations of ULVZs in some regions since the shear velocity would be less reduced. It is important to note that the CMB itself is unaffected by this hypothesis.
Based on recent mineralogical experiments, a wüstite composed material can lead to P- and S-wave velocity reductions of about 30% and 50%, respectively, using a composition of $(Mg_{0.2}Fe_{0.8})O$ [Jacobsen et al., 2002; Wicks et al., 2010]. The density would in turn increase of about 50%. It should be noted that such huge velocity reductions can be achieved by only 1% volume of liquid,

if the liquid is situated in pockets and surrounded by the solid magnesiowüstite [Speziale, pers. comm.]. Thus, large regions of partial melting are not necessary to generate significant shear velocity reductions.
Concluding, this hypothesis is an alternative option because it could explain the seismic (non)-observations that were made so far. However, the order of seismic velocity decrease strongly depends on the amount of iron and is also influenced by anisotropy [Jacobsen et al., 2002]. Moreover, the described laboratory experiments by Wicks et al. [2010] have been conducted at 300 K and no corrections for temperature were applied. Furthermore, the discussed mineralogical results are based on the study of single minerals but the mantle material is chemical heterogeneous and consists of the main components Mg-Si-perovskite, Ca-Si-perovskite, wüstite and post-perovskite.

Beside the mineralogical uncertainties some large-scale geodynamical aspects remain unexplained: How relevant is a self-compression of that very dense layers even they are rather small-scale and thin structures? Would the thickness of the ULVZs decrease with time or are the convective flow processes too dominant? The answer might be provided by future geodynamic studies.

Another possibility of creating ULVZs refers to velocity decreases as a result of liquid silicates, i.e. the usual assumption of regions with partial melts. Williams and Garnero [1996] have described the interdependency of velocity reduction and fluid geometry where melt films are more effective in decreasing velocities. Hence, the question is what is the most likely geometry? Otherwise, is it possible that different solid-liquid geometries exist at different ULVZs, which would result in unequal seismic observations? Furthermore, does such fluid geometries generate a discrete boundary atop the ULVZ or is it rather a gradient behaviour - also in view of a potential time-dependent process?
In case of an iron-rich liquid, the partial melt is much denser compared to liquid silicates. The higher iron content (resultant from interactions with the outer core) additionally shifts the relation of melt geometry and velocity reduction [Williams and Garnero, 1996]. However, the relationship between an iron content and melt fractions is very complex since it depends on the composition of the lower mantle and the phase relations among each other.

Chapter 6

Conclusion

Within the scope of this thesis a large range of low-velocity and density anomalies for the mantle side of the core-mantle boundary have been modelled. The effects on the core-reflected phase PcP have been analysed between 10° and 40° epicentral distance allowing for variations of the key parameters P-wave and S-wave velocities, density, layer thickness, dominant source frequency and ULVZ topography.

Thereby a discrete model space could be developed, but it was shown that this goal cannot be achieved because of the ambiguous findings. The seismic resolution of an ULVZ is limited both for velocity and density contrasts and layer thicknesses. In general, several models create similar amplitude and waveform characteristics. Even more a very thin global core-mantle transition zone (CMTZ), rather than a discrete boundary and also with strong impedance contrasts, cannot be excluded and represents a further development of previous studies: If no precursor is observable but the PcP^{model}/PcP^{smooth} amplitude reduction amounts to more than 10%, a very thin ULVZ of 5 km thickness with a first-order discontinuity at the top and also with a large range of anomaly configurations may exist. Otherwise, if amplitude reductions of less than 10% are obtained, this could indicate either a moderate, thin ULVZ or a gradient mantle-side CMTZ.

The modelling of synthetic seismograms using gradient ULVZs and such with a first-order discontinuity at its upper boundary revealed numerous similarities. Striking amplitude variations occur as function of the distance and the impedance contrasts. Primarily density effects dominate in the very steep-angle range whereas a pronounced velocity dependency in the wide-angle region can be observed. An extreme density increase of 30% is even able to amplify the PcP amplitude in case of an almost perpendicular incidence. The location of polarity reversals of PcP is also dominated by density. Beyond that polarity reversal the velocity reductions dominate the amplitude characteristics where in general the strongest model configuration produces lowest amplitude ratios. These distance dependent features affect also the waveforms and create massive distortions with increasing layer thickness and model contrasts.

Two crucial differences occur between the gradient and discontinuous ULVZs: In case of gradients, the PcP amplitudes decrease with increasing layer thickness whereas for first-order discontinuities the amplitudes remain constant except for thin layers up to 10 km. Hence, a conclusion about the ULVZ thickness - by only considering of the amplitude relations - cannot be drawn. The unique constraint on the structure is provided by the precursor PxP which indicates the anomaly thickness due to its travel time difference with respect to PcP. It was shown that for various models PxP is much larger than PcP. There is a possibility of misinterpretation of the precursor and the core-reflected phase itself above all if the travel time differences are small.

Further conclusions are:

- Damping effects are negligible.
- A source signal with a dominant frequency of 1 Hz may improve the resolution of thin layers.
- The assumed ULVZ undulations create similar focussing and defocussing effects whereby an assumption of a discrete topography is not possible.

The Gräfenberg and NORSAR arrays in central Europe are then used to investigate PcP from deep earthquakes and nuclear explosions. The found characteristics at the CMB below Europe are summarised in figure 6.1. The evaluation of the Semipalatinsk events, measured by the Gräfenberg array, yields several indications of an ULVZ:

- Both PcP amplitude ratios are clearly reduced and can be explained by the same model.
- A notable postcursor, most likely generated by a CMB feature, can be seen for all events with a time delay up to 1.5 s with respect to PcP.
- Some events reveal a small precursor with a similar slowness and frequency as PcP.

Based on the travel time difference of the potential precursor and PcP, the low-velocity anomaly could be 10 - 13.5 km thick. A study of the Hindu Kush events, recorded by the NORSAR array, reinforce the assumption of a moderate ULVZ about 600 southeast of Moscow with a NW-SE extension of about 450 km. Here a single specific assumption about the velocity and density anomaly is not possible but for example the model with contrasts of -5% V_P, -15% V_S and +5% density can explain the measured amplitudes. A configuration of -10%-20%+10% seems also possible.
Furthermore, an undulating CMB can be assumed for some regions below central Europe. Large PcP amplitude deviations of more than 50% can be detected below the SE Finland and NNE of the Caspian Sea. With a view to the previous studies by Kampfmann and Müller [1989] and Neuberg and Wahr [1991], a CMB topography with a wavelength of 200 km and a height of 1-3 km could produce such notable focussing effects.
A third region with an unusual high PcP amplitude is located 50 km north of Budapest. Indeed, the low reflection coefficient indicates a large uncertainty in the interpretation. An interesting limiting case show the PNE data respect to GRF. Here either a CMTZ or a very thin, moderate ULVZ is possible.

Outlook

Even so the depicted evidence for a low-velocity anomaly between SE of Moscow and the Aral Sea is conclusive , it is worthwhile to apply the double-beam method by Krüger et al. [1993] to the Semipalatinsk and Hindu Kush data. Particularly with regard to the potential precursor, this technique shows promise to enhance the resolution of such a weak phase.
Another opportunity to confirm the assumptions of the CMB anomalies forms the extension to a larger dataset. Earthquakes from the southern China to NORSAR generate bounce points that sample the CMB in the vicinity of the predicted ULVZ. However, these are shallow events with depths less than 50 km and in combination with the complex crustal reverberations and the

high noise level at the receiver site a PcP study may become difficult. On the other hand the distance is larger and therewith the reflection coefficient. Otherwise, the China events respect to Gräfenberg probe the CMB close to the Caspian Sea. The conditions at this receiver array may allow a verification of the assumed topography. Further source-receiver combinations which provide a CMB study beneath the western Russia could be earthquakes along the Mid Oceanic Ridge to the FERGHANA and TIPAGE networks in Kyrgyzstan and Tajikistan, respectively. Both are operated by the GFZ Potsdam.
An additional approach of testing the core-mantle region is provided by a 2.5D analysis. Ultimately, the three-dimensional effects of the earth may distort the shown results.
In conclusion, better constraints of the ambiguous anomaly models might be provided by a joined analysis of seismological data, mineralogical experiments and geodynamic modelling.

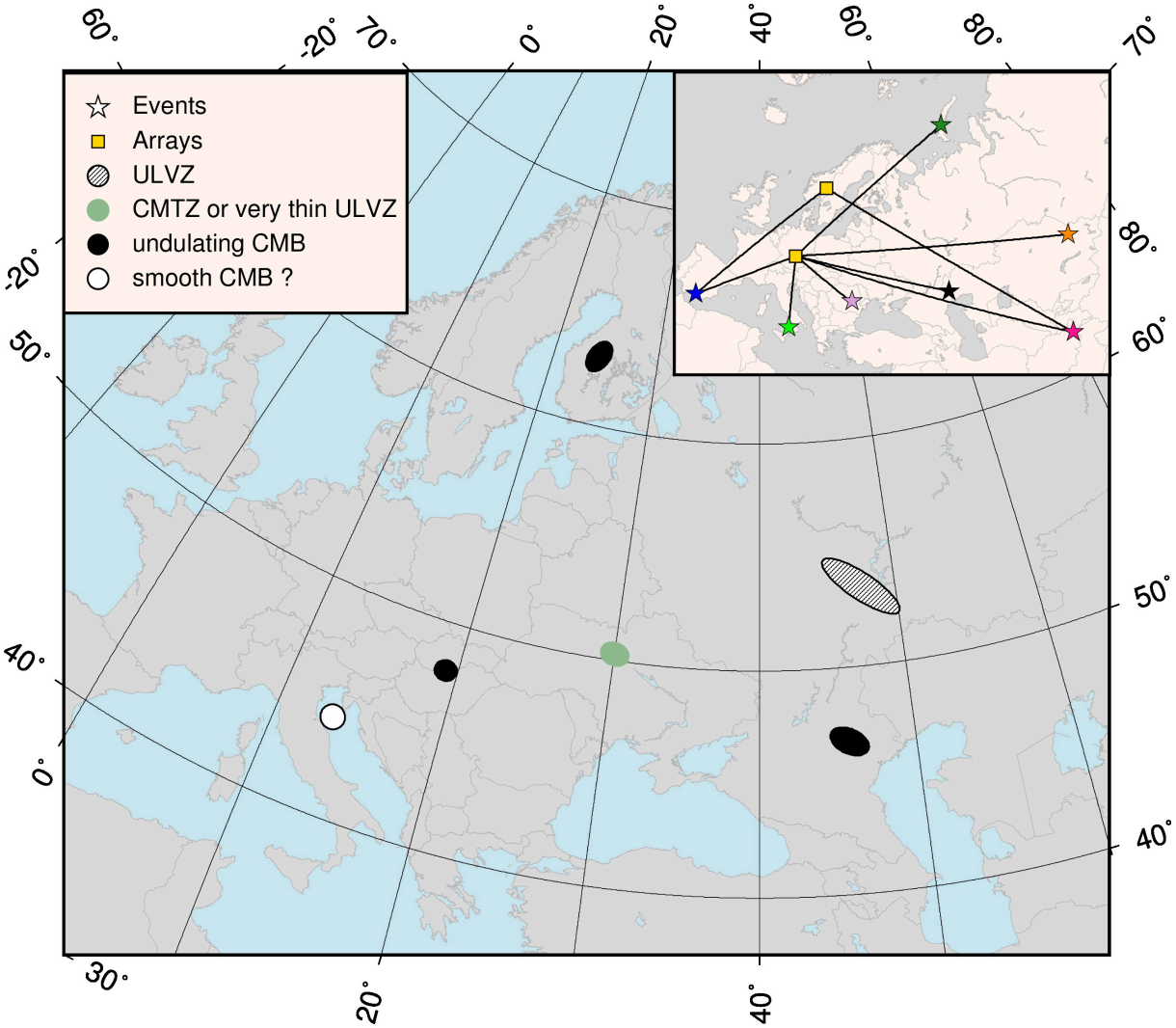

Fig. 6.1: Summary map of the discussed CMB features depending on the effective Fresnel zones, respectively. The projected ULVZ corresponds to its size at the CMB with a NW-SE extension of about 450 km. An azimuthal equidistant projection is used, also for the insert. The insert shows all great circle ray paths of the events studied.

Chapter 7

Appendix

Table 7.1: Summary of amplitude measurements and CMB features for **earthquakes**

	Gräfenberg					NORSAR				
Event	Rad-Pat[a]	$\frac{PcP}{P}$	$\frac{PcP^{data}}{PcP^{smooth}}$	PxP	$\frac{PxP}{PcP}$	Rad-Pat	$\frac{PcP}{P}$	$\frac{PcP^{data}}{PcP^{smooth}}$	PxP	$\frac{PxP}{PcP}$
1	1.358	0.147	1.02	-	-	1.215	0.091	0.53	-	-
2	1.392	0.171	1.01	-	-	1.294	0.107	0.63	-	-
3	1.906	0.139	0.52	-	-	1.514	0.033	0.20	-	-
4	1.255	0.179	1.54	-	-	1.147	0.170	1.00	-	-
5	1.196	0.250	1.18	-	-	1.140	0.068	0.40	-	-
6[d]	1.112	0.200	1.47	-	-	–	–	–	–	–
7[d]	1.264	0.262	1.05	-	-	–	–	–	–	–
8[d]	1.020	0.089	0.82	-	-	–	–	–	–	–
9[d]	1.103	0.172	1.00	-	-	–	–	–	–	–
10[d]	0.949	0.174	0.87	-	-	–	–	–	–	–
11	–	–	–	–	–	1.340	0.087	0.51	-	-
12	–	–	–	–	–	1.785	0.090	0.53	-	-
13	–	–	–	–	–	1.594	0.013	0.08	-	-
14	–	–	–	–	–	1.952	0.118	0.69	-	-
15	1.212	0.045	3.01	-	-	1.572	0.105	0.95	-	-
16	-18[b]	0.009	1.29	-	-	–	–	–	–	–
17	44[b]	0.009	2.43	-	-	–	–	–	–	–
18	0.233[c]	0.006	1.29	-	-	–	–	–	–	–
19	1.067	0.017	0.86	-	-	–	–	–	–	–
20	-1.003	0.062	3.10	-	-	–	–	–	–	–
21	-0.789	0.093	4.65	-	-	–	–	–	–	–
22	-1.538	0.057	2.85	-	-	–	–	–	–	–
23	-0.648	0.122	6.10	-	-	–	–	–	–	–

[a] PcP/P correction factor resultant from the radiation pattern
[b] P on nodal plane respect to GRF
[c] PcP on nodal plane respect to GRF
[d] Not available by NORSAR

Table 7.2: Summary of amplitude measurements and CMB features for **explosions**

	Gräfenberg			
Event	$\frac{PcP}{P}$	$\frac{PcP^{data}}{PcP^{smooth}}$	PxP	$\frac{PxP}{PcP}$
1	0.085	0.52	+	1.0
2	0.125	0.77	+	0.40
3	0.090	0.55	+	0.35
4	0.110	0.68	?	-
5	0.070	0.43	-	-
6	0.090	0.55	+	0.6
7	0.150	0.92	+	0.43
8	0.097	0.60	-	-
9	0.078	0.48	?	-
10	0.160	0.98	?	-
11	0.055	0.34	+	0.46
12	0.127	0.78	-	-
13	0.116	0.71	+	0.55
14	0.078	0.48	+	0.66
15	0.100	0.62	+	0.60
16	0.105	0.65	?	-
17	0.127	0.78	-	-
18	0.133	0.82	?	-
19	0.270	2.34	-	-
20	0.157	1.36	-	-
21	0.238	2.07	-	-
22	0.287	2.49	-	-
23	0.172	1.49	-	-
24	0.155	1.35	-	-
25	0.267	2.32	-	-
26	0.210	1.82	-	-
27	0.177	1.54	-	-
28	0.046	0.75	-	-
29	0.050	0.81	-	-
30	0.070	1.14	-	-
31	0.055	0.90	-	-

+ precursor observable
- precursor not visible
? precursor not clear

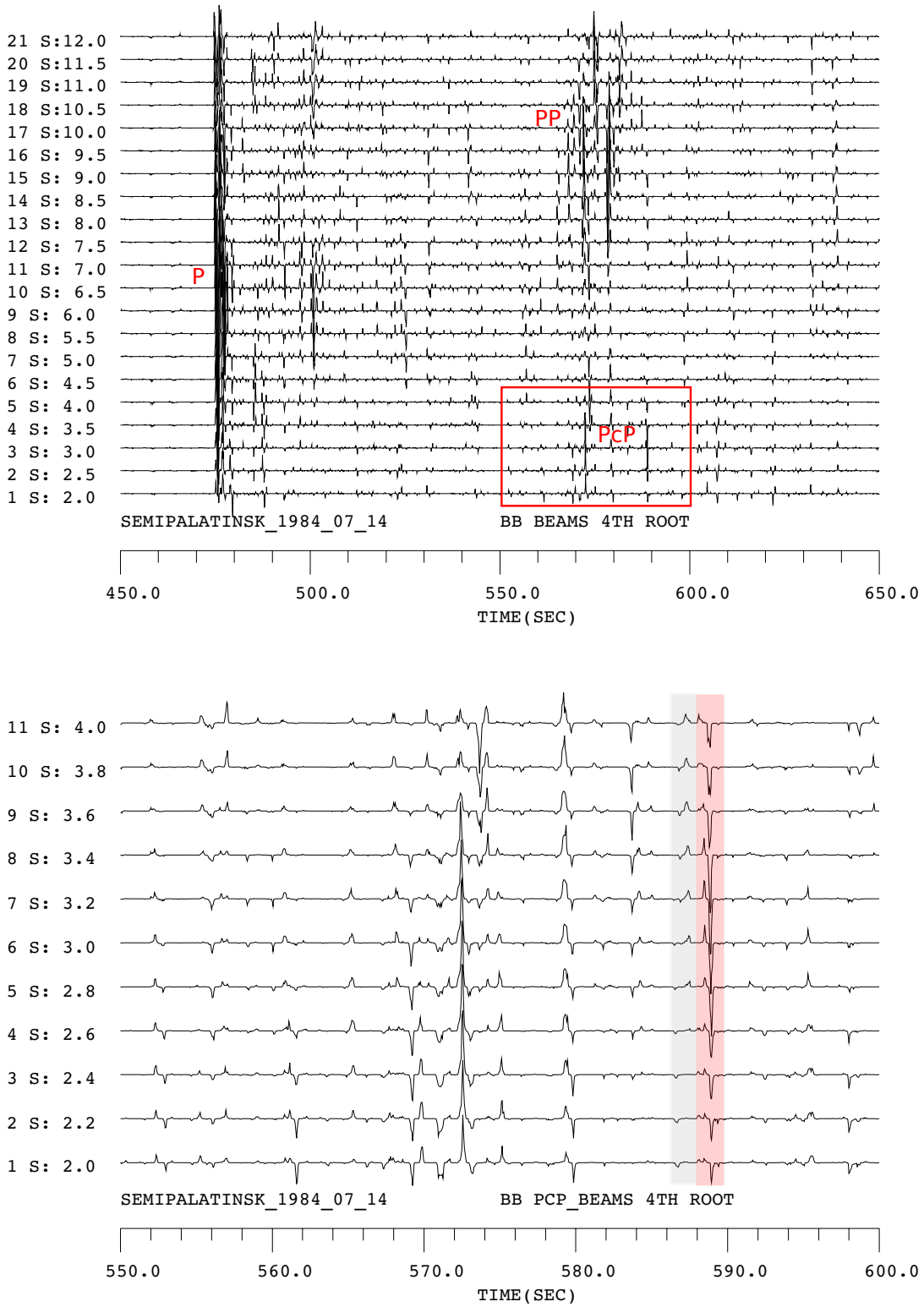

Fig. 7.1: 4th root vespagrams for the **Semipalatinsk** event of 1984-Jul-14 recorded by **GRF**. The upper seismogram section shows the complete relevant slowness range from 2.0 to 12.0 s/° in steps of 0.5 s/°. The wave trains of P, PP and PcP are less resolved than for event 1985-Jun-15 since the overall noise level is much higher. The lower vespagram shows the red marked area in detail for a slowness range from 2.0 to 4.0 s/° in steps of 0.2 s/°. Potential precursor (grey shaded area) and postcursor show a similar slowness as PcP (red shaded area) of about 3.4 s/°. The postcursor is very strong here because of the apparent interference with the negative PcP peak.

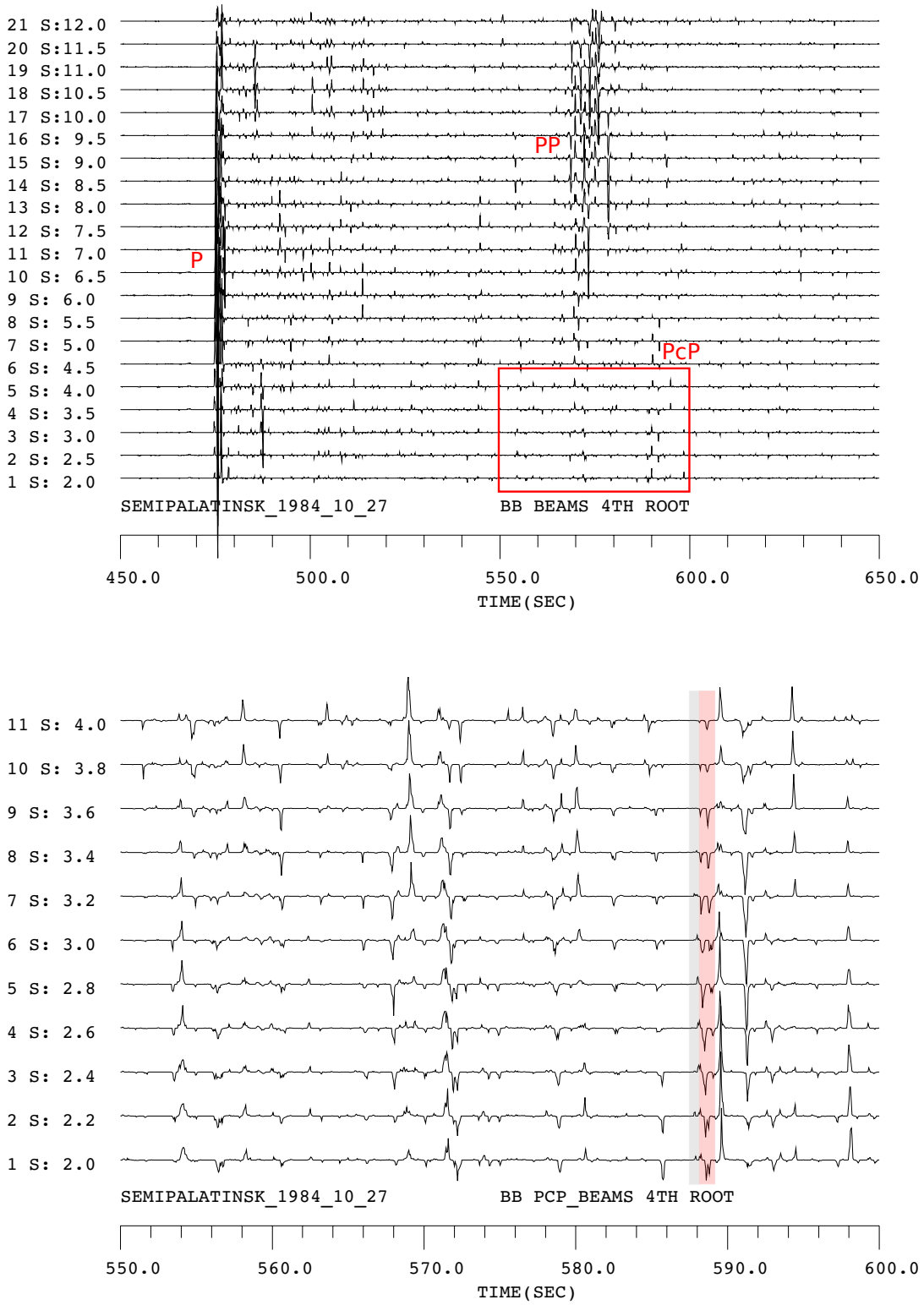

Fig. 7.2: 4th root vespagrams for the **Semipalatinsk** event of 1984-Oct-27 recorded by **GRF**. Upper seismogram section shows the complete relevant slowness range from 2.0 to 12.0 s/° in steps of 0.5 s/°. The wave trains of P and PP are better resolved than PcP. The lower vespagram shows the red marked area in detail for a slowness range from 2.0 to 4.0 s/° in steps of 0.2 s/°. The whole PcP energy is fairly weak for this event with an observed slowness of 2.6 s/°. Extremely narrow pre- and postcursor wiggles can be assumed with a slightly lower slowness of 2.2 s/°.

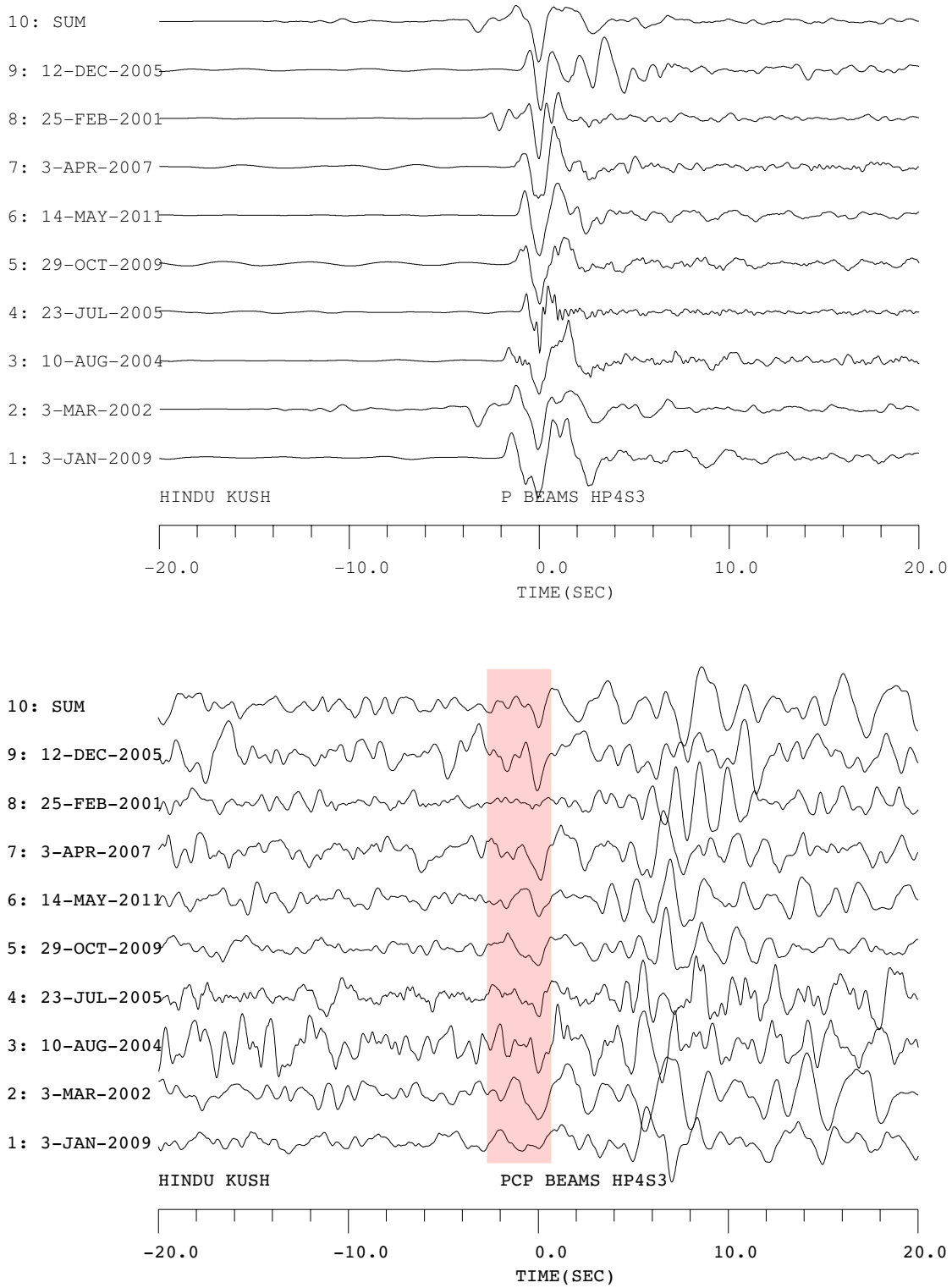

Fig. 7.3: All studied deep earthquakes from the **Hindu Kush** region measured by the **NORSAR** array. Shown are the high-pass filtered beam traces. **Top:** Beam P impulses which are aligned on the maximum negative peaks. **Bottom:** Beam PcP impulses, also aligned on their negative peaks. The mean epicentral distance is 44.4° with a theoretical BAZ of 95°. Each trace is normalised to its maximum amplitude within the displayed time window.

Bibliography

Adushkin, V. and Leith, W. *The Containment of Soviet Underground Nuclear Explosions*, 2001. U.S. Department of the interior Geological Survey.

Aki, K. and Richards, P. *Quantitative Seismology* (University Science Books, 2009), 2nd ed.

Bormann, P. (Ed.). *New Manual of Seismological Observatory Practice (NMSOP-1), IASPEI, GFZ German Research Centre for Geosciences* (Potsdam, 2009).

Brandon, A. and Walker, R. *The debate over core-mantle interactions.* Earth Planet. Sci. Lett., (232): 211–225, 2005.

Buchbinder, G. *Properties of the core-mantle boundary and observations of PcP.* J. Geophys. Res., vol. 73(18): 5901–5923, 1968.

Buffett, B., Garnero, E. and Jeanloz, R. *Sediments at the Top of Earth's Core.* Science, vol. 290: 1338–1342, 2000.

Chowdhury, D. and Frasier, C. *Observations of PcP and P Phases at Lasa at Distances from 26° to 40°.* J. Geophys. Res., vol. 78(26): 6021–6027, 1973.

Crotwell, H., Owens, T. and Ritsema, J. *The TauP Toolkit: Flexible Seismic Travel-time and Ray-path Utilities.* Seis. Res. Letters, vol. 70(2): 154–160, 1999.

Davis, J. and Henson, I. *User's guide to Xgbm: An X-windows system to compute Gaussian beam synthetic Seismograms.* Teledyne Geotech, 1993.

Ding, X. and Helmberger, D. *Modelling D¨ structure beneath Central America with broadband seismic data.* Phys. Earth Planet. Inter., (101): 245–270, 1997.

DTRA Verification Database, 2012. URL http://www.rdss.info/.

Earle, P. and Shearer, P. *Observations of PKKP Precursors Used to Estimate Small-Scale Topography on the Core-Mantle Boundary.* Science, vol. 277: 667–670, 1997.

Ekström, G. and Nettles, M. *The Global Centroid Moment Tensor Project*, 2012. URL http://www.globalcmt.org/.

Frasier, C. and Chowdhury, D. *Effect of Scattering on PcP/P Amplitude Ratios at Lasa From 40° to 84° Distance.* J. Geophys. Res., vol. 79(35): 5469–5477, 1974.

Garnero, E. *Heterogeneity of the lowermost mantle.* Annu. Rev. Earth Planet. Sci., (28): 509–537, 2000.

Garnero, E. and Jeanloz, R. *Fuzzy Patches on the Earth's Core-Mantle Boundary?* Geophys. Res. Lett., vol. 27(17): 2777–2780, 2000.

Große, C. *Die unterirdischen Kernexplosionen im Nordkaspischen Becken (UdSSR).* Diplomarbeit, Geophysikalisches Institut Universität Karlsruhe, 1989.

Gurnis, M., Wysession, M., Knittle, E. and Buffett, B. (Eds.). *The Core-Mantle Boundary Region*, vol. 28 of *Geodynamics Series* (American Geophysical Union, 1998).

Hernlund, J., Thomas, C. and Tackley, P. *A doubling of the post-perovskite phase boundary and structure of the Earth's lowermost mantle.* Nature, vol. 434: 882–886, 2005.

Hirose, K. and Lay, T. *Discovery of Post-Perovskite and New Views on the Core-Mantle-Boundary Region.* Elements, vol. 4: 183–189, 2008.

Hutko, A., Lay, T. and Revenaugh, J. *Localized double-array stacking analysis of PcP: D¨ and ULVZ structure beneath the Cocos plate, Mexico, central Pacific, and north Pacific.* Phys. Earth Planet. Inter., (173): 60–74, 2009.

ISC International Seismological Centre. Online Bulletin, 2010. URL http://www.isc.ac.uk, Thatcham, United Kingdom.

Jacobsen, S., Reichmann, H.-J., Spetzler, H., Mackwell, S., Smyth, J., Angel, R. and McCammon, C. *Structure and elasticity of single-crystal (Mg,Fe)O and a new method of generating shear waves for gigahertz ultrasonic interferometry.* J. Geophys. Res., vol. 107(B2), 2002.

Kampfmann, W. and Müller, G. *PcP Amplitude Calculations for a Core-Mantle Boundary with Topography.* Geophys. Res. Lett., vol. 16(7): 653–656, 1989.

Kanamori, H. *Spectrum of P and PcP in Relation to the Mantle-Core Boundary and Attenuation in the Mantle.* J. Geophys. Res., vol. 72(2): 559–571, 1967.

Kennett, B., Engdahl, E. and Buland, R. *Constraints on seismic velocities in the earth from travel times.* Geophys. J. Int., (122): 108–124, 1995.

Kennett, B.L.N. *The seismic wavefield. Volume I: Introduction and Theoretical Development* (Cambridge University Press, 2001).

Khalturin, V., Rautian, T., Richards, P. and Leith, W. *A Review of Nuclear Testing by the Soviet Union at Novaya Zemlya, 1955-1990.* Science and Global Security, (13): 1–42, 2005.

Kito, T. and Krüger, F. *Heterogeneities in D¨ beneath the southwestern Pacific inferred from scattered and reflected P-waves.* Geophys. Res. Lett., vol. 28(13): 2545–2548, 2001.

Kito, T. and Krüger, F. *Seismic heterogeneous structure in the lowermost mantle beneath the southwestern Pacific.* J. Geophys. Res., vol. 109(B09304): 1–21, 2004.

Kito, T., Rost, S., Thomas, C. and Garnero, E. *New insights into the P- and S-wave velocity structure of the D¨ discontinuity beneath the Cocos plate.* Geophys. J. Int., (169): 631–645, 2007.

Knittle, E. and Jeanloz, R. *Simulating the core-mantle boundary: an experimental study of high-pressure reactions between silicates and liquid iron.* Geophys. Res. Lett., vol. 16(7): 609–612, 1989.

Knittle, E. and Jeanloz, R. *Earth's Core-Mantle Boundary: Results of Experiments at High Pressures and Temperatures.* Science, vol. 251: 1438–1443, 1991.

Krüger, F. and Weber, M. *The effect of low-velocity sediments on the mislocation vectors of the GRF array.* Geophys. J. Int., (108): 387–393, 1992.

Krüger, F., Weber, M. and Scherbaum, F. *Double Beam of Anomalies in the Core-Mantle Boundary Region.* Geophys. Res. Lett., vol. 20(14): 1475–1478, 1993.

Krüger, F., Weber, M., Scherbaum, F. and Schlittenhardt, J. *Evidence of normal and inhomogeneous lowermost mantle and core-mantle boundary structure under the Arctic and northern Canada.* Geophys. J. Int., (122): 637–657, 1995.

Labrosse, S., Hernlund, J. and Coltice, N. *A crystallizing dense magma ocean at the base of the Earth's mantle.* Nature, vol. 450: 866–869, 2007.

Lay, T. and Helmberger, D. *A lower mantle S-wave triplication and the shear velocity structure of D¨.* Geophys. J. R. Astron. Soc., (75): 799–838, 1983.

Lay, T., Williams, Q. and Garnero, E. *The core-mantle boundary layer and deep Earth dynamics.* Nature, vol. 392: 461–468, 1998.

Mao, W., Mao, H., Sturhahn, W., Zhao, J., Prakapenka, V., Meng, Y., Shu, J., Fei, Y. and Hemley, R. *Iron-Rich Post-Perovskite and the Origin of Ultralow-Velocity Zones.* Science, vol. 312: 564–565, 2006.

Mao, Z., Lin, J., Scott, H., H, W., Prakapenka, V., Xiao, Y., Chow, P. and McCammon, C. *Iron-rich perovskite in the Earth's lower mantle.* Earth Planet. Sci. Lett., (309): 179–184, 2011.

McNamara, A., Garnero, E. and Rost, S. *Tracking deep mantle reservoirs with ultra-low velocity zones.* Earth Planet. Sci. Lett., (299): 1–9, 2010.

Menke, W. *Few 2-50 km corrugations on the core-mantle boundary.* Geophys. Res. Lett., vol. 13(13): 1501–1504, 1986.

Monfret, T., Deschamps, A. and Romanowicz, B. *The Romanian Earthquake of August 30, 1986: A Study Based on GEOSCOPE Very Long-Period and Broadband Data.* Pageoph, vol. 133(2): 367–379, 1990.

Mori, J. and Helmberger, D. *Localized boundary layer below the mid-Pacific velocity anomaly identified from a PcP precursor.* J. Geophys. Res., vol. 100(B10): 20,359–20,365, 1995.

Müller, G. *Earth-Flattening Approximation for Body Waves Derived from Geometric Ray Theory - Improvements, Corrections and Range of Applicability.* J. Geophys., (44): 429–436, 1977.

Müller, G. *The reflectivity method: a tutorial.* J. Geophys., (58): 153–174, 1985.

Müller, G. *Theory of Elastic Waves.* Tech. Rep., Deutsches GeoForschungsZentrum Potsdam, 2003.

Murakami, M., Hirose, K., Kawamura, K., Sata, N. and Ohishi, Y. *Post-Perovskite Phase Transition in $MgSiO_3$.* Science, vol. 304: 855–858, 2004.

Mykkeltveit, S. *(Ed.) NORSAR Basic Seismological Research*, 1990. Scientific Report No. 7.

Neuberg, J. and Wahr, J. *Detailed investigation of a spot on the core-mantle boundary using digital PcP data.* Phys. Earth Planet. Inter., (68): 132–143, 1991.

Nomura, R., Ozawa, H., Tateno, S., Hirose, K., Hernlund, J., Muto, S., Ishii, H. and Hiraoka, N. *Spin crossover and iron-rich silicate melt in the Earth's deep mantle.* Nature, vol. 473: 199–203, 2011.

Oganov, A. and Ono, S. *Theoretical and experimental evidence for a post-perovskite phase of $MgSiO_3$ in Earth's D¨ layer.* Nature, vol. 430: 445–448, 2004.

Persh, S. and Vidale, J. *Reflection properties of the core-mantle boundary from global stacks of PcP and ScP.* J. Geophys. Res., vol. 109(B04309): 1–11, 2004.

Persh, S., Vidale, J. and Earle, P. *Absence of short-period ULVZ precursors to PcP and ScP from two regions of the CMB.* Geophys. Res. Lett., vol. 28(2), 2001.

Pirli, M. *NORSAR System Responses Manual*, 2nd ed., 2010.

Revenaugh, F. and Meyer, R. *Seismic evidence of partial melt within a possibly ubiquitous low-velocity layer at the base of the mantle.* Science, vol. 277: 670–673, 1997.

Ross, A., Thybo, H. and Solidilov, L. *Reflection seismic profiles of the core-mantle boundary.* J. Geophys. Res., vol. 109(B08303), 2004.

Rost, S., Garnero, E., Thorne, M. and Hutko, A. *On the absence of an ultralow-velocity zone in the North Pacific.* J. Geophys. Res., vol. 115(B04312), 2010.

Rost, S., Garnero, E. and Williams, Q. *Fine-scale ultralow-velocity zone structure from high-frequency seismic array data.* J. Geophys. Res., vol. 111(B09310), 2006.

Rost, S., Garnero, E., Williams, Q. and Manga, M. *Seismological constraints on a possible plume root at the core-mantle boundary.* Nature, vol. 435: 666–669, 2005.

Rost, S. and Revenaugh, J. *Seismic Detection of Rigid Zones at the Top of the Core.* Science, vol. 294: 1911–1914, 2001.

Rost, S. and Revenaugh, J. *Small-scale changes of core-mantle boundary reflectivity studied using core reflected PcP.* Phys. Earth Planet. Inter., (145): 19–36, 2004.

Rost, S. and Thomas, C. *Array Seismology: Methods and Applications.* Reviews of Geophysics, (40,3), 2002.

Rost, S. and Thomas, S. *High resolution CMB imaging from migration of short-period core reflected phases.* Phys. Earth Planet. Inter., (183): 143–150, 2010.

Scherbaum, F., Krüger, F. and Weber, M. *Double beam imaging: Mapping lower mantle heterogeneities using combinations of source and receiver arrays.* J. Geophys. Res., vol. 102(B1): 507–522, 1997.

Schlittenhardt, J. *Array-Untersuchungen von reflektierten und diffraktierten Kernphasen.* Ph.D. thesis, Johann Wolfgang Goethe-Universität zu Frankfurt am Main, 1984.

Schweitzer, J. *Slowness Corrections - One Way to Improve IDC Products.* Pure appl. geophys., (158): 375–396, 2001.

Schweitzer, J. *Simultaneous inversion of steep-angle observations of PcP and ScP in Europe - what can we learn about the core-mantle boundary?* Geophys. J. Int., (151): 209–220, 2002.

Seismological Central Observatory, 2012. URL http://www.szgrf.bgr.de/, Germany.

Sidorin, I., Gurnis, M. and Helmberger, D. *Evidence for a Ubiquitous Seismic Discontinuity at the Base of the Mantle.* Science, vol. 286: 1326–1331, 1999.

Stein, S. and Wysession, M. *An Introduction to Seismology, Earthquakes, and Earth Structure* (Blackwell Publishing, 2003).

Sultanov, D., Murphy, J. and Rubinstein, K. *A Seismic Source Summary for Soviet Peaceful Nuclear Explosions.* Bull. Seis. Soc. Am., vol. 89(3): 640–647, 1999.

Thomas, C. *Untersuchung der P- und S-Geschwindigkeitsstruktur des unteren Erdmantels mittels Daten des Deutschen Seismologischen Regionalnetzes und des Gräfenberg-Arrays.* Diplomarbeit, Friedrich-Alexander-Universität Erlangen-Nürnberg, 1994.

Thomas, C., Wookey, J., Brodholt, J. and Fieseler, T. *Anisotropy as cause for polarity reversals of D¨ reflections.* Earth Planet. Sci. Lett., (in press), 2011.

Thorne, M. and Garnero, E. *Inferences on ultralow-velocity zone structure from a global analysis of SPdKS.* J. Geophys. Res., vol. 109(B08301), 2004.

Thybo, H., Ross, A. and Egorkin, A. *Explosion seismic reflections from the Earth's core.* Phys. Earth Planet. Inter., (216): 693–702, 2003.

United States Geological Survey. *National Earthquake Information Center: NEIC global earthquake bulletin*, 2010. URL http://earthquake.usgs.gov/earthquakes/eqarchives/epic/, Colorado, United States.

Vidale, J. and Benz, H. *A sharp and flat section of the core-mantle boundary.* Nature, vol. 359: 627–629, 1992.

Weber, M. *Interaktives seismisches Modellieren in 1-D und 2-D Medien mit der Gauss-Beam Methode*, . Vorlesungsskript.

Weber, M. *Computation of body-wave seismograms in absorbing 2-D media using the Gaussian beam method: comparison with exact methods.* Geophysical Journal, (92): 9–24, 1988.

Weber, M. *P- and S-wave reflections from anomalies in the lowermost mantle.* Geophys. J. Int., (115): 183–210, 1993.

Weber, M. *Lamellae in D¨? An alternative model for lower mantle anomalies.* Geophys. Res. Lett., vol. 21(23): 2531–2534, 1994a.

Weber, M. *Traveltime and amplitude anomalies at the seismic broad-band array GRF.* Geophys. J. Int., (118): 57–74, 1994b.

Weber, M. and Davis, J. *Evidence of a laterally variable lower mantle structure from P and S waves.* Geophys. J. Int., (102): 231–255, 1990.

Wen, L. and Helmberger, D. *Ultra-Low Velocity Zones Near the Core-Mantle Boundary from Broadband PKP Precursors.* Science, 1998.

Wicks, J., Jackson, J. and Sturhahn, W. *Very low sound velocities in iron-rich (Mg,Fe)O: Implications for the core-mantle boundary region.* Geophys. Res. Lett., vol. 37(L15304), 2010.

Williams, Q. and Garnero, E. *Seismic Evidence for Partial Melt at the Base of Earth's Mantle.* Science, vol. 273: 1528–1530, 1996.

Williams, Q., Revenaugh, J. and Garnero, E. *A Correlation Between Ultra-Low Basal Velocities in the Mantle and Hot Spots.* Science, 1998.

Wright, C. and Lyons, J. *Further evidence for radial velocity anomalies in the lower mantle.* Pageoph, vol. 119, 1980/81.

Yang, X., North, R., Romney, C. and Richards, P. *Worldwide Nuclear Explosions*, year unknown.

Yilmaz, O. *Seismic Data Processing*, vol. 2 (Society of Exploration Geophysicists, 1987).

Acknowledgement

Prof. Michael Weber for providing the theme of this thesis and his friendly supervision. He always conveys confidence which bears me out to continue.

Prof. Frank Krüger for his inspiring ideas and support.

Prof. Tine Thomas for providing me the *Xgbm* program.

Stefanie Hempel for her efforts in calculation of 2.5D ultra-low velocity zones with my parameters.

A special thank to Sergio Speziale for his differentiated view on published mineralogical experiments and the resultant influence on seismological interpretations.
Also I am thankful for his engagement and willingness to advise me of the relevant mineralogical aspects among the numberless studies.

Johannes Schweitzer for providing NORSAR data.

Klaus Stammler for providing Gräfenberg data and *Seismic Handler*.